2019

Study of GaN:Eu & delta-InN Based Active Regions For High Efficiency Long Wavelength Emitters

Ioannis Fragkos
Lehigh University

Study of GaN:Eu & delta-InN Based Active Regions For High Efficiency Long Wavelength Emitters

by

Ioannis Emmanouil Fragkos

Presented to the Graduate and Research Committee

of Lehigh University

in Candidacy for the Degree of

Doctor of Philosophy

in

Electrical Engineering

Lehigh University

May 2019

Approved and recommended for acceptance as a dissertation in partial fulfillment of the requirements for the degree of Doctor of Philosophy.

_____
Date

_____
Nelson Tansu, Dissertation Advisor

_____
Accepted Date

Committee Members:

_____
Nelson Tansu, Committee Chair

_____
Jonathan J. Wierer, Jr.

_____
Volkmar Dierolf

_____
Chao Zhou

Acknowledgments

For the completion of this work I have enjoyed the assistance and support of many people, to all of whom I am very grateful. I would like to thank my Ph.D advisor Prof. Nelson Tansu for giving me the opportunity to study and work in his group, and providing me the means to extend my scientific knowledge and my technical skills in the field of photonics. I would also like to thank Prof. Tansu for his advice on my professional development. I would also like to thank Prof. Jonathan Wierer, as well as, my office and lab mates, Damir Borovac, Wei Sun, Syed Ahmed Al Muyeed and Onos Ogidi-Ekoko for the collaboration and the numerous scientific and non-scientific discussions we had through my Ph.D years. Many thanks to the scientific staff member Dr. Renbo Song for his help with the OMVPE reactor and the valuable and critical assistance he provided to me during my experimental work. Many thanks to my Greek friends at Lehigh University Dr. Vasileios Christou, Dr. Georgios Tsampras, Dr. Thomas Charisoulis, Georgios Pilitsis and Ilias-Petros Larsinos for the good times we had, as well as, for their support they provided to me. I am very grateful to my family back in Greece for their immense support all these years that I have been away. Finally, many thanks to my K.W for her love and support that she showed - and keeps showing - to me all these years.

Τίς δὲ βίος, τί δὲ τερπνὸν ἄτερ χρυσῆς Ἀφροδίτης ;

Contents

List of Tables

List of Figures

Abstract

III-nitride alloys and nanostructures have been proved reliable materials for electronic and photonic applications. In particular, indium-gallium-nitride (InGaN) based quantum wells (QW) have been greatly improved over the years exhibiting very high efficiencies (>80%) in the blue spectral regime and have been successfully implemented as active region in light emitting diodes (LEDs). However, there are still challenges to achieve longer wavelength emission with high quantum efficiencies from the InGaN based alloy. Novel III-nitride active region designs and III-nitride materials doped with rare-earth elements have been proposed over the years for high efficiency visible light emission. Part of this dissertation is focused on the study of the europium doped GaN red light emitter (GaN:Eu). A model has been developed to elucidate the limiting factors for the efficiency droop issue observed in this type of emitter and also explain the discrepancy observed between optically-pumped and electrically driven GaN:Eu based devices. The model also provides experimental approaches to enhance the internal quantum efficiency of the GaN:Eu when it is implemented as an active region in a light emitting diode. In addition, a novel type of active region based on the integration of a thin InN layer (δ-layer) in an InGaN QW is studied for high efficiency visible light emission. This novel active region design is experimentally investigated via the organometallic vapor phase epitaxy technique (OMVPE). Strategies for efficient δ-InN integration into the InGaN QW are developed and proof-of-concepts experiments are carried out. These studies are important

for providing an intuitive approach in the development of high efficiency electrically-driven GaN:Eu and δ-InN/InGaN QW based devices in the visible spectral regime, which will enable their use for lighting applications.

Chapter 1

Introduction

1.1 Current status and future prospects of III-Nitride based light emitting devices

In recent years, III-Nitride based alloys (i.e $Al_xGa_{1-x}N$, $In_xGa_{1-x}N$) have been placed at the frontiers of semiconductor technologies. The use of III-Nitrides has found places in a wide span of technological applications including bio-applications, thermoelectrics, solar cells, power electronics, optoelectronics and photonics [1-10]. As of 2018, the high demand of III-nitride based alloys and their applications is reflected to the increased revenues of the related semiconductor companies.

Among III-Nitrides, $In_xGa_{1-x}N$ -based alloys are of great interest. As shown in figure 1.1, the versatility to tune the band-gap of InGaN -based alloys from the UV (AlN) to the infrared (InN) spectral regime have established them as the main technologies driving the light emitting diode (LED) innovations [11-13]. However, despite the rapid development of high efficiency UV and blue InGaN based light emitting diodes for general lighting applications, the commercially available primary colors (green and red) are generated via a phosphor -energy down conversion- integrated with an InGaN based blue LED.

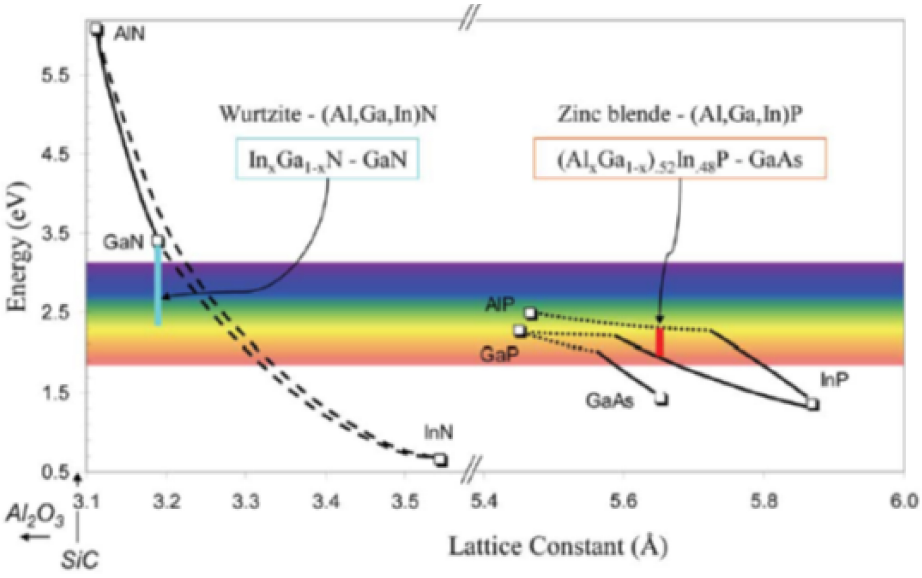

Figure 1.1: Lattice constant versus energy band-gap. The versatility of alloying the (Al,Ga,In)N material system can result in the energy coverage beyond the visible spectral regime [12].

For over a decade the pursuit of high efficiency InGaN based light emitters towards red spectral regime has proven to be challenging. The need for higher In-content in the InGaN active region for longer wavelength emission, results in phase separation and higher polarization fields with reduced wavefunction overlap, which are detrimental for efficiency of the device [15-17]. In figure 1.2(a) the evolution of the external quantum efficiencies from the III-Nitride based alloys along with other commercially used material systems for lighting applications is displayed. In addition, the highest reported external quantum efficiencies in the visible spectral regime are shown in figure 1.2(b).

Despite the demonstration of InGaN based LED in the red spectra regime, the highest reported external quantum efficiency (EQE) is 2.9% which is much lower from the blue and green InGaN-based QW LEDs [18]. Several works in recent years have suggested innovative approaches with the potential of achieving high efficiency for InGaN based quantum well (QW) LED towards red spectral regime. These works include the investigation of staggered InGaN QWs, strain compensated InGaN QWs,

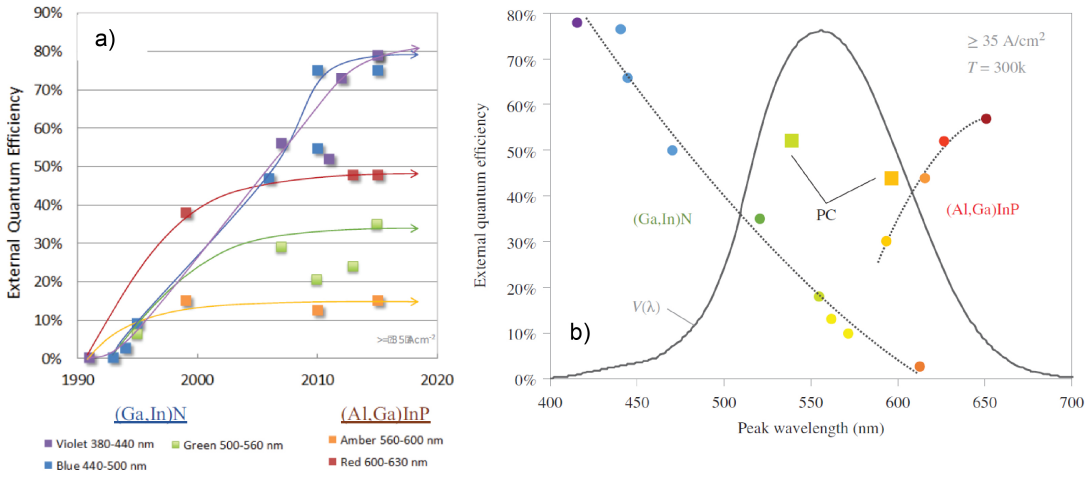

Figure 1.2: (a) Improvement of the external quantum efficiency of the (Ga,In)N based LED's and (AlGa)InP based LED's over the years [13]. (b) Best-reported LED external quantum efficiencies as a function of peak emission wavelength, at typical operating current densities of 35 Acm^{-2} or greater, and at room temperature T=300K. In addition to primary (Ga,In)N and (Al,Ga)InP LED performance, full-conversion phosphor converted (PC) LED performance for green and amber emission are indicated [14]. As of 2018 the highest reported external quantum efficiency of an InGaN based LED in the red spectral regime is 2.9% [18].

alternative substrates and buffer layers of InGaN QWs, InGaN with AlGaN and AlInN interlayers, semipolar and non-polar InGaN QW, InGaN/dilute-As GaNAs interface QW and InGaN delta- InN QW [18-28]. Furthermore, another interesting approach which targets to the emission of red and green from the GaN material, is the doping of GaN with rare-earth elements such as europium (Eu) and erbium (Er) [29-31]. The possibility of introducing europium element (Eu) into the GaN material has enabled the realization of GaN:Eu red light emitting devices including LEDs in the past decade [32-38]. However, the internal quantum efficiency (IQE) of the GaN:Eu emitter is low ($< 1\%$), despite the recent years of effort in improving the device performance.

Therefore, achieving high efficiencies towards red spectral regime either through the improvements of the InGaN- or GaN:Eu-based LEDs is a challenging task. Understanding the limiting factors and finding new methods and ways of improving the

efficiency of the GaN based LEDs at longer emission wavelengths, will open a new era for smart and ultraefficient solid stated lighting technology in the future [39].

1.2 Research work accomplished

1.2.1 Current injection efficiency study of GaN:Eu based devices

The efficiency of the GaN:Eu based red light emitters has been investigated. More specifically, a physically intuitive current injection efficiency model for the electrically-driven GaN:Eu based devices with different active region configuration (GaN:Eu based QW and GaN/GaN:Eu/GaN) has been developed to clarify the necessary means to achieve device quantum efficiency higher than the state-of-the-art for the GaN:Eu system. The identification and analysis of limiting factors for high internal quantum efficiencies (IQE) are accomplished through the current injection efficiency model. In addition, the issue of the significantly lower IQE in the electrically-driven GaN:Eu devices in comparison to the optically-pumped GaN:Eu devices is clarified in the framework of this injection efficiency model. The improved understanding of the quantum efficiency issue through current injection efficiency model provides a pathway to address the limiting factors in electrically-driven devices. Based on the injection efficiency model, several experimental approaches are suggested to address the limitations in achieving high IQE GaN:Eu QW based devices in red spectral regime.

1.2.2 Plasmonics for efficiency enhancement of GaN:Eu devices

Titanium nitride (TiN) has been theoretically investigated as a plasmonic material to enhance the internal quantum efficiency of a GaN:Eu red light emitter. Theoretical calculations are performed to evaluate the surface plasmon polariton dispersion relation and Purcell enhancement factor for a single TiN layer on top of the GaN:Eu emitter. High Purcell factors ($> 100\%$) are predicted for the case of a single TiN layer. Moreover, by tuning the dielectric properties of TiN and through the utilization of a double TiN layer, the surface plasmon frequency can be tuned to cover a wide range in the visible spectral regime with high Purcell factors. The findings of this work suggest the potential use of TiN as plasmonic material for increasing the internal quantum efficiency in GaN:Eu red light emitters as well as other GaN based light emitters.

1.2.3 Pulse-OMVPE growth studies of III-Nitrides

The pulsed-organometallic vapor phase epitaxy (OMVPE) of indium nitride (InN) has been investigated. The goal is the fabrication of high quality InN films on top of on GaN/sapphire templates and its potential use as a delta layer in the InGaN based QW. Theoretical simulations suggest that the integration of InN with the InGaN-based technology forms nano-engineered active region which is applicable for red and near-infrared light emitters.

In the pulsed-OMVPE mode, the ammonia (NH_3) was constantly flowing into the chamber, while pulsing the indium precursor ($TMIn$). A comprehensive study on the effects of the pulsing period (T_{p}), V/III ratio, and temperature (T) is carried out under a growth pressure of $200torr$. The study shows that the presence of the metallic-In, as well as the structural and electrical properties of the InN thin films

can be tuned by varying the growth conditions. By selecting the optimum conditions for the pulse-OMVPE growth of InN, a preliminary study on the integration of the InGaN-delta-InN QW is performed. In addition, the use of a low temperature AlGaN interlayer is crucial for the device performance. XRD analysis and PL studies were performed to evaluate the quality and luminescence of the emitters.

The growth and study of this preliminary structure (InGaN/delta-InN+AlGaN) exhibits a 50 nm wavelength shift compared to the InGaN/AlGaN structure. This approach opens the possibility of delta-InN active region as a promising candidate for the realization of InGaN based-QW emitters in the long wavelength regime.

References

1. Keller, S. et al. Gallium nitride based high power heterojunction field effect transistors: Process development and present status at UCSB. IEEE Transactions on Elect. Dev., 48, 3 (2001).

2. Oka, T. and Nozawa, N., AlGaN/GaN recessed MIS-gate HFET with high-threshold-voltage normally-off operation for power electronics applications. IEEE Elect. Dev. Lett., 29, 7 (2008).

3. Tong, H., et al. Thermoelectric properties of lattice-matched AlInN alloy grown by metal organic chemical vapor deposition. Appl. Phys. Lett., 97, 112105 (2010).

4. Yamaguchi, S., Izaki, R., Kaiwa, N., Sugimura, S., and Yamamoto, A., Thermoelectric devices using InN and AlxIn1-xN thin films prepared by reactive radiofrequency Sputtering. Appl. Phys. Lett., 84, 5344 (2004).

5. Dahal, R., et al. InGaN/GaN multiple quantum well solar cells with long operating wavelengths. Appl. Phys. Lett., 94, 063505 (2009).

6. Kirste, R., et al. Electronic biosensors based on III-nitride semiconductors. Annual Rev. Analytical Chem., 8, 149-169 (2015).

7. Nakamura, S., Senoh, M., Iwasa, N., and Nagahama, S., High-brightness InGaN blue, green and yellow light-emitting diodes with quantum well structures. Jap.

J. Appl. Phys., 34, Part 2, Number 7A (1995).

8. Nakamura, S., et al. InGaN-based multi-quantum-well structure laser diodes. Jap. J. Appl. Phys., 35, Part 2, Number 1B (1996).

9. Masui, H., Nakamura, S., DenBaars, S. P., Mishra, U. K., Nonpolar and semipolar III-nitride light-emitting diodes: Achievements and challenges. IEEE Transactions. on Elect. Dev., 57, 1 (2010).

10. Tansu, N., et al. III-Nitride Photonics. IEEE Photonics Journal, 2, 241-248 (2010).

11. Steigerwald, D. A., et al. Illumination with, solid state lighting technology. IEEE J. on Select. Top. in Quant. Elect., 8, 2 (2002).

12. Krames, M. R., Status and future of high power light-emitting diodes for solid-state lighting. J. of Disp. Tech., 3, 2 (2007).

13. Krames, M. R., Status and future prospects for visible-spectrum light-emitting diodes. Digest of tech. papers, 47, 39-41 (2016).

14. Krames M.R. LED Materials and Devices. Materials for Solid State Lighting and Displays, A. Kitai, ed., Wiley (2017).

15. T. Takeuchi et al. Jap. J. Appl. Phys., 36, 2, 4A (1997).

16. M. D. McCluskey et al. Appl. Phys. Lett., 72, 1730–1732 (1998).

17. B. Damilano et al. J. Phys. D: Appl. Phys., 48, 403001 (2015).

18. Hwang, J., Hashimoto, R., Saito, S., and Nunoue, S. Development of InGaN-based red LED grown on (0001) polar surface. Appl. Phys. Express, 7, 071003 (2014).

19. Zhao, H. P., et al. Approaches for high internal quantum efficiency green InGaN light-emitting diodes with large overlap quantum wells. Optics Express, 19, A991-A1007 (2011).

20. Zhao, H. P., Growths of staggered InGaN quantum wells light-emitting diodes emitting at 520-525 nm employing graded growth-temperature profile. Appl. Phys. Lett., 95, 061104 (2009).

21. Zhao, H. P., Arif, R. A., Ee, Y. K., and Tansu, N., Self-consistent analysis of strain-compensated InGaN-AlGaN quantum wells for lasers and light emitting diodes. IEEE J. Quantum Electron., 45, 66-78 (2009).

22. Zhang, J. and Tansu, N. Improvement in spontaneous emission rates for InGaN quantum wells on ternary InGaN substrate for light emitting, diodes. J. Appl. Phys., 110, 113110 (2011).

23. Daubler, J. et al. Long wavelength emitting GaInN quantum wells on metamorphic GaInN buffer layers with enlarged in-plane lattice parameter. Appl. Phys. Lett., 105, 111111 (2014).

24. Ohkawa, K., Watanabe, T., Sakamoto, M., Hirako, A. & Deura, M. 740-nm emission from InGaN based LEDs on c-plane sapphire substrates by MOVPE. J. Crys. Growth, 343, 13–16 (2012).

25. Kawaguchi, Y. et al. Semipolar (2021) single-quantum-well red light-emitting diodes with a low forward voltage. Jap. J. Appl. Phys., 52, 08JC08 (2013).

26. Zhao, H. P., Liu, G. Y., and Tansu, N. Analysis of InGaN-delta-InN quantum wells for light-emitting diodes. Appl. Phys. Lett., 97, 131114 (2010).

27. Tan, C. K., Borovac, D., Sun, W., and Tansu, N., InGaN/Dilute-As GaNAs interface quantum well for red emitters. Sci. Reports, 6, 19271 (2016).

28. Sun W., Muyeed S. A., Song R., Wierer J. J. Jr., & Tansu N. Integrating AlInN interlayers into InGaN/GaN multiple quantum wells for enhanced green emission. Appl. Phys. Lett., 112, 201106 (2018).

29. Favennec, P. N., L'Haridon, H., Salvi, M., Moutonnet, D., and Le Guillou, Y., Luminescence of erbium implanted in various semiconductors: IV, III-V and II-VI materials. Electron. Lett., 25, 718–719 (1989).

30. Kenyon, A. J., Recent developments in rare-earth doped materials for optoelectronics. Progress in Quantum Elect., 26, 225–284 (2002).

31. Hömmerich, U., et al. Photoluminescence studies of rare earth (Er, Eu, Tm) in situ doped GaN. Mat. Sc. Eng. B, 105, 91–96 (2003).

32. Heikenfeld, J., Garter, M., Lee, D. S., Birkhahn, R., and Steckl, A. J., Red light emission by photoluminescence and electroluminescence from Eu-doped GaN. Appl. Phys. Lett., 75, 1189 (1999).

33. Kim, J. H., and Holloway, P. H., Room-temperature photoluminescence and electroluminescence properties of sputter grown gallium nitride doped with europium. J. Appl. Phys., 95, 4787 (2004).

34. Park, J. H., and Steckl, A. J., Laser action in Eu-doped GaN thin-film cavity at room temperature. Appl. Phys. Lett., 85, 4588 (2004).

35. Okada, H. et al. Light emitting FET based-on spatially selective doping of Eu in AlGaN/GaN HEMT. Phys. Stat. Sol., 6, S631-S634 (2009).

36. Nishikawa, A., Kawasaki, T., Furukawa, N., Terai, Y., and Fujiwara, Y., Room-temperature red emission from a p-type/europium-doped/n-type gallium nitride light-emitting diode under current injection. Appl. Phys. Express., 2, 071004 (2009).

37. Sekiguchi, H., et al. Red light-emitting diodes with site-selective Eu-doped GaN active layer. Jap. J. Appl. Phys., 52, 08JH01 (2013).

38. Zhu, W. et al. High-power Eu-doped GaN red LED based on a multilayer structure grown at lower temperatures by organometallic vapor phase epitaxy. MRS Adv., 67, 159-164 (2017).

39. Tsao, J. Y., et al. Toward smart and ultra-efficient solid-state lighting. Adv. Optical Mater., 2, 809–836 (2014).

Chapter 2

Rare-Earth doped Gallium Nitride

2.1 Eu-doped GaN for red light emission

An alternative approach of achieving red emission without the need of high In-content of InGaN based alloys is the incorporation of rare earth elements into GaN (e.g Europium) [1-3]. The possibility of introducing Europium element (Eu) into the GaN material has enabled the realization of GaN:Eu red light emitting devices including LEDs in the past decade [4-20]. However, the internal quantum efficiency (IQE) of the GaN:Eu emitter is still low ($< 1\%$), despite the recent years of effort in improving the device performance. These efforts include improving the GaN:Eu material quality and utilizing heterostructures for higher IQE [3,15,18-21]. Improving the IQE of the GaN:Eu devices is necessary for practical technological implementation.

In addition, another major obstacle is found to be the IQE discrepancy between the electrically driven and optically excited GaN:Eu devices. Interestingly, the IQE of electrically-driven GaN:Eu devices is much lower than that of the optically-pumped GaN:Eu devices. Despite the fact that optically-pumped devices exhibited an increase in the output power and consequently in the IQE over the years, the electrically-driven devices showed a saturation in the output power, probably due to the IQE limitation

of the device [22]. This discrepancy is possibly attributed to the dependency of the IQE on the current injection efficiency of the GaN:Eu active region for the two different excitation ways. The need of electrically-driven device is however arguably stronger than optically-pumped device because in many applications including LEDs, the devices are typically driven by injected current to achieve emission. If the GaN:Eu device is to be employed for the light emitting applications, the understanding of the factors which lead to low efficiency in electrically-driven GaN:Eu device needs to be enhanced. Thus, developing a current injection efficiency model of the GaN:Eu active region will provide a qualitative picture and a better understanding of the IQE of both optically-pumped and electrically-driven GaN:Eu red light emitters. Besides, the model can further provide the opportunity to enhance the design and fabrication of high efficiency GaN:Eu based red light emitters.

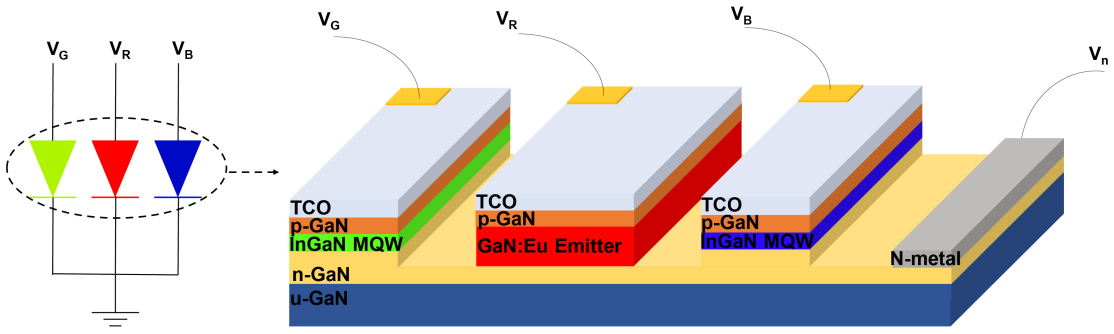

Figure 2.1: Concept of monolithically integrated white LED based on GaN material. The high efficiency blue and green InGaN QW can be monolithically integrated with the high efficiency red GaN:Eu emitter.

The development for high efficiency red light emitters based on $In_xGa_{1-x}N$ QW or GaN:Eu active region, is mandatory for the monolithic realization of GaN-based white LEDs. The solutions for challenges to achieve InGaN-based red emitters are important and still being pursued. However, the use of GaN:Eu LEDs may provide an interesting advantage over InGaN, namely: a) narrower linewidth red spectral emission, and b) less temperature-sensitivity to the emission wavelength [12-15,20,23,24]. The availability of red emitters based on GaN:Eu LEDs provides a pathway for inte-

gration with the more established InGaN-based blue and green emitters. Figure 2.1 shows the integration method that can be pursued for GaN-based display emitters with integration of InGaN-based LEDs and red-emitters based on GaN:Eu materials. Such integration can provide a solution for individually-addressed emitter in the three colors grown by selective-area epitaxy.

2.2 Excitation path of Eu^{+3} ions in the GaN host

It is known that the excitation of the Eu^{+3} ions in the GaN host is mediated by traps which are close to the vicinity of the Eu^{+3} ions [5,6,18,22,25-27]. The created or injected electron-hole pairs in the GaN host are captured from these traps where they recombine and release energy. The released energy is used for the excitation of the nearby Eu^{+3} ion. The excitation path of the Eu^{+3} ion is a complex process since different carrier processes are involved, specifically including carrier transport across the GaN:Eu region, fundamental recombination processes of carriers in the GaN host, and interactions between the host, traps and Eu^{+3} ions. This process becomes more complex in the presence of different active regions such as an AlGaN/GaN:Eu/AlGaN heterostructure and a GaN/GaN:Eu/GaN homojunction. In these type of structures, which are used for devices applications, additional mechanisms are involved. These mechanisms will be presented in detail in the following sections of Chapter 2.

Traps present in the vicinity of Eu^{+3} ions assist the excitation of the Eu^{+3} ion for red light emission. More specifically, studies have revealed several emission sites related to different configurations of trap-Eu^{+3} ion known as complexes [22,26]. In this model, this pictured is simplified by assuming a single level trap located near to the Eu^{+3} ion. In addition, it is assumed that the nature of the complex in this study is a bound-exciton in the vicinity of the Eu^{+3} ion.

In addition, it is important to clearly state that the SHR recombination, which is

present in semiconductors, is related to the non-radiative recombination rate of free carriers from defect centers in the crystal lattice. This mechanism is still present for the case of the GaN:Eu emitter. However, it is important to clarify that those defect centers should not be confused with the traps that are in the vicinity of the Eu^{+3} ions and assist to their excitation. Therefore, the SHR monomolecular recombination rate primarily describes how fast the free carriers are captured and recombine non-radiatively at the defects in the crystal lattice.

As shown in figure 2.2, the free electron-hole pairs (e-h) present in the GaN host are captured by traps, where this state of captured electron-hole pairs at the trap level is denoted as bound-exciton formation / complex foramtion - these terms are used interchangeably - in this model. The recombination of e-h pair at the trap level can result in the energy transfer and excitation to a nearby Eu^{+3} ion. In addition, different processes can take place at the trap level, including the non-radiative recombination of e-h pairs, which results in heat transfer to the lattice, as well as the bound-exciton dissociation process which leads to the release of the electron and hole back to the conduction band and valence band respectively. The deexcitation process of the Eu^{+3} ion consists of the radiative and non-radiative processes, as well as the energy back-transfer process resulting in a formation of a bound-exciton.

2.3 CIE Models - GaN:Eu QW

This chapter presents the development of physically intuitive current injection efficiency model for a GaN:Eu QW active region for understanding the discrepancy between the efficiencies of optically-pumped and electrically-driven GaN:Eu QW based devices. The discrepancies between the optically-pumped and electrically-driven RE-doped GaN LEDs devices can be explained from the differences on the carrier injection processes in the two types of devices. The following study identifies and explains the

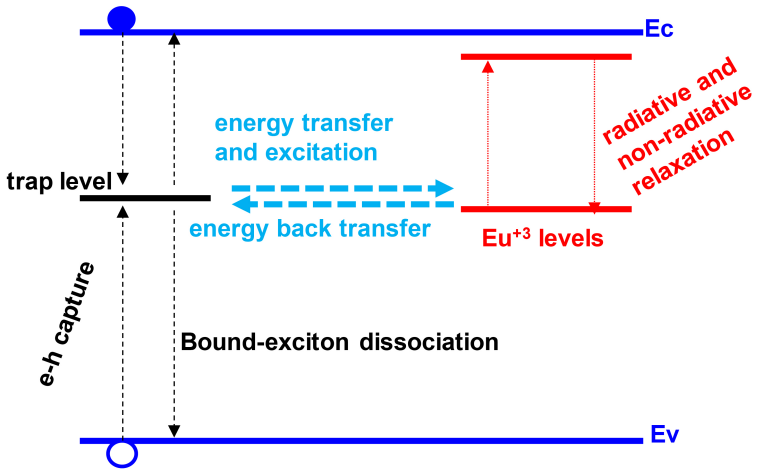

Figure 2.2: Trap assisted excitation path of Eu^{+3} ion in the GaN host. The free electron-hole pairs present in the GaN host are captured by traps close to the vicinity of Eu^{+3} ions and form bound-excitons. The recombination of bound-excitons can result to energy transfer and excitation of a nearby Eu^{+3} ion. The excited Eu^{+3} ion can de-excite non-radiatively and radiatively as well as non-radiatively by releasing the energy to a nearby trap to form a bound-exciton.

limiting factors for the low IQE of the GaN:Eu QW active region and provides the pathway to enhance the IQE of the GaN:Eu QW based devices.

2.3.1 GaN:Eu QW active region considerations

The analysis in this work is carried out based on the model of a trap assisted excitation path of Eu^{+3} ion in the GaN:Eu QW active region with $Al_xGa_{1-x}N$ barriers as shown in figure 2.3. The role of traps is presented by a single trap level but note that the extended nature of these traps close to the vicinity of Eu^{+3} ions could also result in several levels. The electron-hole pair capture from the trap with a characteristic rate $1/\tau_{\text{c\_cap}}$ is notated as complex (bound-exciton) in this model, as shown in figure 2.3(b). The subsequent recombination of carriers at the trap level (i.e. de-excitation of complex, figure 2.3(c) releases a non-radiative recombination energy that leads to the following possible reactions: (a) excitation of the nearby Eu^{+3} ion with a characteristic energy transfer rate of $1/\tau_{\text{tr}}$, (b) energy to the crystal lattice with a

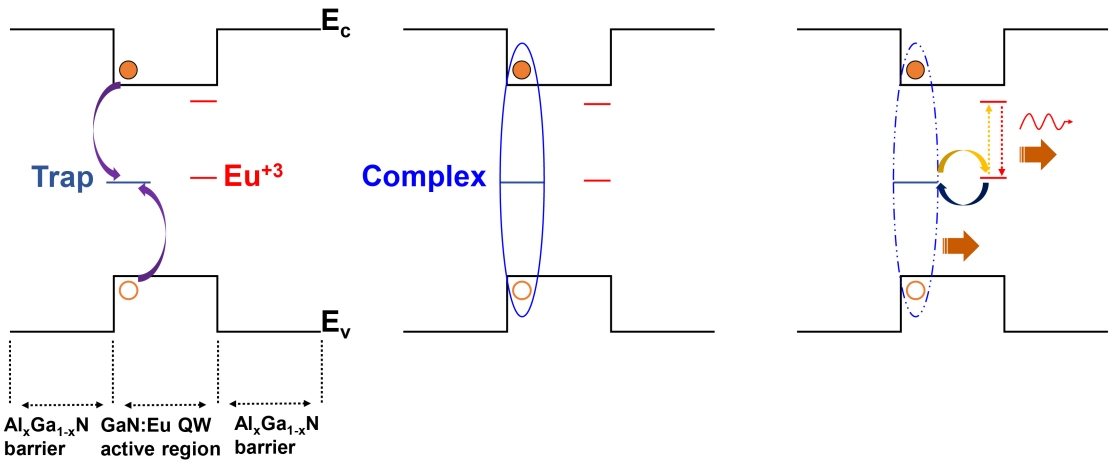

Figure 2.3: Model of the trap assisted excitation of Eu^{+3} ion in GaN:Eu QW active region. (a) The confined electron-hole in the GaN:Eu QW are captured by the traps (purple arrows) which are close to the vicinity of Eu^{+3} ion and results in (b) complex formation. (c) After the complex formation the electron-hole pair can recombine at the trap level by releasing a non-radiative energy to the crystal lattice (brown arrow) or release a non-radiative energy used for the excitation of the nearby Eu^{+3} ion (energy transfer process-gold arrow) or it can dissociate by releasing the electron-hole back to the GaN:Eu QW. Similarly, the excited Eu^{+3}can recombine non-radiatively by releasing energy to the crystal lattice (brown arrow) or release non-radiative energy for complex formation (energy back-transfer process, dark blue arrow) or recombine radiatively with photon emission (red arrow).

characteristic rate of $1/\tau_{\text{c\_heat}}$. In addition, after the formation of complex, another process can occur which results in the electron-hole population of the QW with a characteristic rate of $1/\tau_{\text{diss}}$ (complex dissociation process). Additional mechanisms to consider including the consequence of the then-de-excitation of Eu^{+3} ions: a) photon release with a characteristic rate of $1/\tau_{\text{rad}}$, b) non-radiative de-excitation with a characteristic rate of $1/\tau_{\text{Eu\_heat}}$, and c) complex formation through energy back-transfer process with a characteristic rate of $1/\tau_{\text{bt}}$. In addition, the carrier processes related to the GaN host and the $Al_xGa_{1-x}N$ barrier need to be taken into consideration, will be further discussed below.

2.3.2 Electrical model

In the electrically-driven GaN:Eu QW device, carriers are injected into the GaN:Eu QW active region from the barriers. This analysis is similar to the current injection efficiency analysis in a typical QW without the presence of RE elements [28,29]. The presence of Eu^{+3} ions modifies these rate equations to account for coupling with Eu^{+3} ions and complexes.

Previous experimental work on QW devices have shown that the carriers injected into the QW can escape to the barrier due to the high thermionic emission energy [30]. The thermionic-related carrier escape process needs to be accounted in the determination of IQE of electrically-driven QW based devices. In addition, the non-radiative and spontaneous radiative recombination process of carriers in the GaN host and $Al_xGa_{1-x}N$ barriers are also taken into consideration in the electrically-driven GaN:Eu QW.

The carrier rate equations both in the barrier (N_B) and GaN:Eu QW active region (N_{QW}) are given by:

$$\frac{dN_B}{dt} = \frac{I_{tot}}{q\,V_B} + \frac{N_{QW}}{\tau_e}\frac{V_{QW}}{V_B} - N_B\left(\frac{1}{\tau_B} + \frac{1}{\tau_{bw}}\right) \tag{2.1}$$

$$\frac{dN_{QW}}{dt} = \frac{N_B}{\tau_{bw}}\frac{V_B}{V_{QW}} + \frac{N_c}{\tau_{diss}}\frac{V_{Eu}}{V_{QW}} - N_{QW}\left(\frac{1}{\tau_{nr}} + \frac{1}{\tau_{sp}} + \frac{1}{\tau_e} + \frac{1}{\tau_{c\_cap}}\right) \tag{2.2}$$

where, the V_B, V_{QW}, V_{Eu} are the volumes of the barrier, GaN:Eu QW and Eu-doped region of the GaN:Eu QW respectively. The I_{tot} is the total injected current in the barriers which is assumed to be equal to the total injected current into the device, $1/\tau_{\mathrm{e}}$ is the carrier thermionic escape time form the GaN:Eu QW active region to the barriers, $1/\tau_{\mathrm{B}}$ is the carrier lifetime in the barrier described by the non-radiative and spontaneous radiative processes in the barrier, and $1/\tau_{\mathrm{bw}}$ is the barrier-well life-

time [28,31]. The radiative and non-radiative carrier processes in the GaN host are described by the $1/\tau_{\rm sp}$ and $1/\tau_{\rm nr}$ respectively. In general, the non-radiative and spontaneous radiative recombination rates in the GaN host and $Al_xGa_{1-x}N$ barriers are functions of the carrier concentrations in the QW and barrier, the bimolecular recombination coefficient B, Shockley-Hall-Read (SHR) constant A, and Auger coefficient C. More details regarding the non-radiative and spontaneous radiative recombination processes of carriers in the GaN host and $Al_xGa_{1-x}N$ barriers, as well as the thermionic escape from GaN:Eu QW active region to the $Al_xGa_{1-x}N$ barriers can be found in references [28,29,31-34]. The rate equations of complexes (N_c) and excited Eu^{+3} ions (N_{Eu}) in the GaN:Eu QW active region are:

$$\begin{aligned}\frac{dN_c}{dt} =& N_{QW}C_{c\_cap}\left(N_{traps}-N_c\right)\frac{V_{QW}}{V_{Eu}} + N_{Eu}C_{bt}\left(N_{traps}-N_c\right) \\ &- N_c\left(C_{tr}\ \ \left(N-N_{Eu}\right)+\frac{1}{\tau_{diss}}+\frac{1}{\tau_{c\_heat}}\right)\end{aligned} \tag{2.3}$$

$$\frac{dN_{Eu}}{dt} = N_cC_{tr}\left(N-N_{Eu}\right) - N_{Eu}\left(C_{bt}\left(N_{traps}-N_c\right)+\frac{1}{\tau_{rad}}+\frac{1}{\tau_{Eu\_heat}}\right) \tag{2.4}$$

where, the N and N_{traps} are the concentrations of Eu^{+3} ions and traps in the GaN:Eu QW active region, respectively. The parameters $C_{\rm c\_cap}$, $C_{\rm bt}$ and $C_{\rm tr}$ are defined as the capture, back-transfer and transfer coefficients in cm^3/s respectively. For the rate equations (2.3) and (2.4), a general capture, back-transfer and transfer rate can be defined as:

$$C_{c\_cap}\left(N_{traps}-N_c\right) = \frac{1}{\tau_{cap0}}\left(1-\frac{N_c}{N_{traps}}\right) = \frac{1}{\tau_{c_cap}} \tag{2.5}$$

$$C_{bt}\left(N_{traps}-N_c\right)=\frac{1}{\tau_{bt0}}\left(1-\frac{N_c}{N_{traps}}\right)=\frac{1}{\tau_{bt}} \tag{2.6}$$

$$C_{tr}\left(N-N_{Eu}\right)=\frac{1}{\tau_{tr0}}\left(1-\frac{N_{Eu}}{N}\right)=\frac{1}{\tau_{tr}} \tag{2.7}$$

Equations (2.5)-(2.7) account for saturation in the excited Eu^{+3} concentration as well as in the concentration of formed complexes, when substituted in the rate equations (2.3) and (2.4). The subscript 0 denotes the relative capture, transfer and back-transfer rate and the term in the parenthesis denotes the degree of the respective excitation of Eu^{+3} ion and the complex concentration. Thus, the terms of $1/\tau_{\mathrm{c\_cap}}$, $1/\tau_{\mathrm{tr}}$ and $1/\tau_{\mathrm{bt}}$ can be viewed respectively as the general capture transfer and back-transfer rates of the system.

The injection efficiency of GaN:Eu QW active region is the ratio of the current arising from the radiative and non-radiative de-excitation of Eu^{+3} ions to the total current injected into the GaN:Eu QW system I_{tot}, and can be expressed as:

$$\eta_{inj\_electrical}=\frac{I_{Eu}}{I_{tot}} \tag{2.8}$$

where, the I_{Eu} represents the total recombination current arising from the radiative and non-radiative de-excitation of the Eu^{+3} ion and is defined as:

$$I_{Eu}=\frac{N_{Eu}\ q\ V_{Eu}}{\tau} \tag{2.9}$$

with

$$\frac{1}{\tau}=\frac{1}{\tau_{rad}}+\frac{1}{\tau_{Eu_heat}} \tag{2.10}$$

where, the q is the electron charge.

Solving the system of equations (2.1)-(2.4) under steady state condition the cur-

rent injection efficiency of the electrical model is obtained:

$$\eta_{inj\_electrical} = \left[\left(1 + \frac{\tau_{bw}}{\left(\frac{1}{\tau_B} + \frac{1}{\tau_{bw}}\right)^{-1}} \right) \left(-\frac{\tau\ \tau_{tr}}{\tau_{Eu}\ \tau_{diss}} + \frac{\tau\ \tau_{c\_cap}}{\left(\frac{1}{\tau_{nr}} + \frac{1}{\tau_{sp}} + \frac{1}{\tau_{c_cap}}\right)^{-1}} \left(\frac{\tau_{tr}}{\tau_{Eu}\ \tau_{comp}} - \frac{1}{\tau_{bt}} \right) \right) - \frac{\tau\ \tau_{c\_cap}}{\tau_e} \left(\frac{\tau_{tr}}{\tau_{Eu}\ \tau_{comp}} - \frac{1}{\tau_{bt}} \right) \right]^{-1}. \tag{2.11}$$

where, the $1/\tau_{\mathrm{Eu}}$ and $1/\tau_{\mathrm{comp}}$ are rates related to Eu^{+3} and complex:

$$\frac{1}{\tau_{Eu}} = \frac{1}{\tau_{rad}} + \frac{1}{\tau_{Eu\_heat}} + \frac{1}{\tau_{bt}} \tag{2.12}$$

$$\frac{1}{\tau_{comp}} = \frac{1}{\tau_{tr}} + \frac{1}{\tau_{c_heat}} + \frac{1}{\tau_{diss}} \tag{2.13}$$

the internal quantum efficiency ($\eta_{\mathrm{IQE\_electrical}}$) for the electrical model is given by:

$$\eta_{IQE\_electrical} = \eta_{inj\_electrical}\ \eta_{rad} \tag{2.14}$$

where, the η_{rad} is the radiative efficiency of the Eu^{+3} ions defined as the ratio of radiative to both radiative and non-radiative de-excitation of Eu^{+3} ions:

$$\eta_{rad} = \frac{N_{Eu}/\tau_{rad}}{N_{Eu}/\tau} = \frac{\frac{1}{\tau_{rad}}}{\frac{1}{\tau_{rad}} + \frac{1}{\tau_{Eu\_heat}}} \tag{2.15}$$

2.3.3 Optical model

For the case of optically-pumped GaN:Eu QW, the thermionic emission rate from the GaN:Eu QW active region to the $Al_xGa_{1-x}N$ barrier is neglected. In optically-

pumped GaN:Eu QW, the excitation of the GaN host is resonant, and the generated carriers do not possess excess energy to escape the QW [35-38]. For the same reason, the $Al_xGa_{1-x}N$ barriers are not excited and hence the non-radiative and radiative process of carriers in the barriers can be neglected.

In the optically-pumped GaN:Eu QW, the assumption that the GaN:Eu QW active region is excited resonantly above the band-gap with a photon flux ϕ, results in a rate equation of carriers in the GaN:Eu QW active region (N_{QW}) of:

$$\frac{dN_{QW}}{dt} = \alpha\ \varphi + \frac{N_c}{\tau_{diss}}\frac{V_{Eu}}{V_{QW}} - N_{QW}\ \left(\frac{1}{\tau_{nr}} + \frac{1}{\tau_{sp}} + \frac{1}{\tau_{c\_cap}}\right) \tag{2.16}$$

where, the α is the absorption coefficient of GaN and the ϕ is the photon flux of the excitation. The first term of the left part of equation (2.16) can be viewed as the corresponding current I_{tot} arising from the creation of carriers due to absorption of the incident photon flux and is equal to:

$$a\ \varphi = \frac{I_{tot}}{q\ V_{QW}} \tag{2.17}$$

The rate equations of complexes (N_c) and excited Eu^{+3} ions (N_{Eu}) in the GaN:Eu QW active region are same as in the case of electrically-driven GaN:Eu QW and are given from equations (2.3)-(2.4). The injection efficiency for the optical model is defined as:

$$\eta_{inj\_optical} = \frac{I_{Eu}}{I_{tot}} \tag{2.18}$$

where, the I_{Eu} is defined from equation (2.9).

Solving the system of equations (2.3)-(2.4) and (2.16) under steady state condition, the injection efficiency for the optical model is obtained:

$$\eta_{inj\_optical} = \left(\frac{\tau\ \tau_{c\_cap}}{\left(\frac{1}{\tau_{nr}} + \frac{1}{\tau_{sp}} + \frac{1}{\tau_{c\_cap}}\right)^{-1}} \left(\frac{\tau_{tr}}{\tau_{Eu}\ \tau_{comp}} - \frac{1}{\tau_{bt}} \right) - \frac{\tau\ \tau_{tr}}{\tau_{Eu}\ \tau_{diss}} \right)^{-1} \tag{2.19}$$

The internal quantum efficiency for the optical model is given from equation (2.14) with the respective injection efficiency.

2.3.4 Comparison between optical and electrical model

The analysis of the current injection efficiency model indicates fundamental differences in the excitation path of Eu^{+3} ion in the GaN:Eu QW active region for the optically-pumped and electrically-driven GaN:Eu QW. In figure 2.4 a flow chart depicts the related mechanisms and phenomena along the excitation path of Eu^{+3} ion in the GaN:Eu QW for both models.

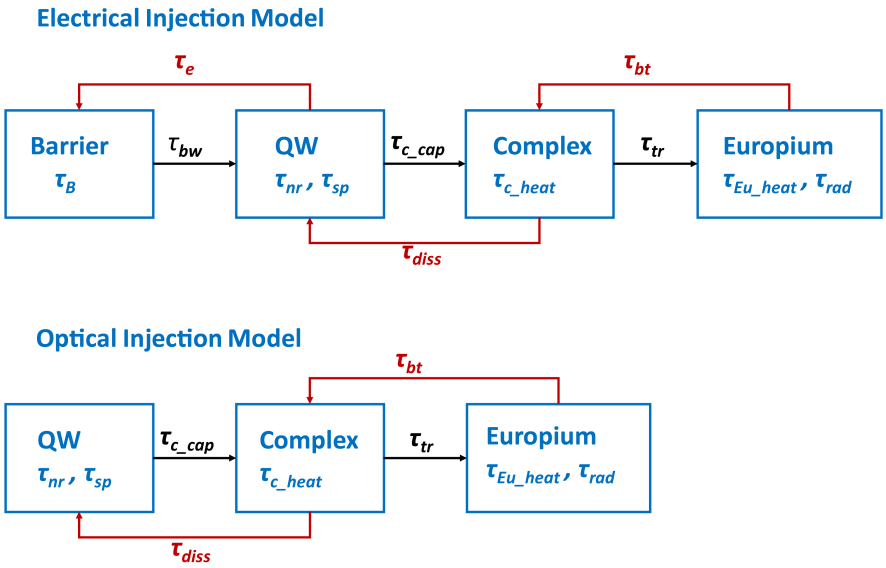

Figure 2.4: Flow charts of electrical and optical current injection efficiency models. The blue boxes indicate the different levels of barrier, GaN:Eu QW, complex and Eu^{+3} ion. Each level includes its own related processes. The levels are connected via the 'forward mechanisms' (black arrows), and via the 'recycling mechanisms' (red arrows).

More specifically, the presence of the barrier level in the electrical model results in transport phenomena of the carriers. The effect of barrier-well lifetime which depends on the mobility of the carriers and the temperature T strongly influences the injection efficiency in the active region in a similar way as in the case of a QW without the presence of RE elements [29,33]. Additionally, recombination mechanisms (monomolecular, bimolecular and Auger recombination) also exist in the barrier. Further, the barrier opens an extra path for the carriers through the recycling mechanisms (red arrows in figure 2.4), increasing the probability of carrier deviation from the Eu^{+3} excitation path. The thermionic escape from QW to the barrier, which is proportional to the concentration of carriers (N_{QW}), becomes stronger with increasing the current density [28,32,33]. The transport phenomena and thermionic process limit the injection efficiency and internal quantum efficiency in the electrically-driven GaN:Eu QW device as opposed to optically-pumped GaN:Eu QW in which these phenomena do not exist.

2.3.5 Simulation results

This section presents how the parameters such as SHR constant A, capture time τ_{cap0} , transfer time τ_{tr0}, back-transfer time τ_{bt0}, dissociation time τ_{diss}, and Eu^{+3} radiative lifetime τ_{rad}, affect the injection efficiency of electrically driven and optical-pumped Eu-doped GaN QW active region. Table 2.1 presents the parameters used in the numerical calculation of the injection efficiency for the GaN:Eu QW active region. The QW and barrier parameters used for the simulations, such as the values of effective masses and mobilities, can be found in reference [31] and correspond to experimental values for the III-nitride materials. For the numerical calculations, the bimolecular recombination coefficient B and Auger coefficient C are fixed to 10^{-11} cm^3/s and 10^{-32} cm^6/s respectively [31]. However, those experimental values can significantly vary among GaN samples fabricated under different growth conditions.

In particular, values of the SHR recombination constant A have been reported within the range [10^{-6}-10^{-8} s^{-1}] [53,54]. Note that the A, B and C coefficients, which describe the radiative and non-radiative processes in the GaN host and $Al_xGa_{1-x}N$ barriers, are assumed to be the same for the barriers and the well. The Al composition was set at $x = 10\%$ for the $Al_xGa_{1-x}N$ barriers.

Moreover, as mentioned in section 2.2, the traps that capture free electron-hole pairs to form a bound-exciton, as shown in figure 2.3, are distinct from the SHR related crystal defects. Those traps are related to the Eu^{+3} ion incorporation into the GaN host [25-27]. In addition, those traps are described by the τ_{cap0}, back transfer time τ_{ttr0} , dissociation time τ_{diss} and a non-radiative time $\tau_{\text{c\_heat}}$. Those characteristic times have been obtained from experimental works [39]. In this experimental work [39], time resolved photoluminescence measurements were performed in GaN:Eu samples. The PL decay signal was fitted according to different trap-assisted excitation models. From this PL decay fittings a relative energy transfer time between a trap state and GaN host (denoted as transfer time in this thesis), as well as, energy transfer time between the Eu^{+3} ions and the trap level (denoted as back-transfer time in this thesis) was able to be obtained. The calculated results from the experimental work in [39] - which are in the order of μs. -were used as a reference point for all the numerical calculations presented in this thesis. However, in the models presented in this thesis, there are processes related to the bound-exciton recombination which result to the crystal lattice heat, as well as, the dissociation process of the complex as defined in paragraph 2.3. Although those processes might be present, there are not available data in the literature regarding the magnitude of the corresponding lifetimes. However, in the following simulations those processes (τ_{diss} and $\tau_{\text{c\_heat}}$) are assigned to a lifetime of 1 ms to ensure negligible effect on the current injection efficiency with respect to the other lifetimes which are in the order of microseconds.

In the present analysis, the injection efficiency ($\eta_{\text{inj\_optical}}$, $\eta_{\text{inj\_electrical}}$) is plotted

with the excited Eu^{+3} concentration (N_{Eu}) versus the photon flux (ϕ) - optical model -and input current density (J) - electrical model - (figures 2.5-2.9). As shown in figures 2.5-2.9, the injection efficiency of the Eu-doped GaN QW active region exhibits the droop characteristics. Since the excited Eu^{+3} concentration cannot exceed the maximum available Eu^{+3} concentration in the active region, the excited Eu^{+3} concentration increases with the photon flux and the current density. At a point where the excited Eu^{+3} concentration saturates due to the maximum available Eu^{+3} concentration in the active region, the subsequent increase of photon flux and current density leads to the droop in the injection efficiency. The rate of this saturation and the droop in the injection efficiency depend on the values of the different parameters related to specific mechanisms in the excitation path.

Parameters	Study I	Study II	Study III	Study IV	Study V
A $(10^7\ s^{-1})$	0.1-1	1	1	1	1
τ_{cap0} $(10^{-7}\ s)$	10	0.1-10	10	10	10
τ_{tr0} $(10^{-7}\ s)$	360	360	3.6-360	360	360
τ_{diss} $(10^{-3}\ s)$	1	1	1	0.0001-1	1
τ_{bt0} $(10^{-6}\ s)$	200	200	200	0.2-2	200
$\tau_{\text{c\_heat}}$ $(10^{-3}\ s)$	1	1	1	1	1
$\tau_{\text{Eu\_heat}}$ $(10^{-3}\ s)$	1	1	1	1	1
$\tau_{\text{rad}}(10^{-6}\ s)$	400	400	400	400	30-400
N (cm^{-3})	10^{19}	10^{19}	10^{19}	10^{19}	10^{19}
N_{traps} (cm^{-3})	10^{19}	10^{19}	10^{19}	10^{19}	10^{19}
L_{QW}, L_{Eu}, L_B (nm)	2.5, 2.5, 5	2.5, 2.5, 5	2.5, 2.5, 5	2.5, 2.5, 5	2.5, 2.5, 5

Table 2.1: Parameters used for the numerical calculations of the current injection efficiency models. Study of individual parameters associated with the Eu^{+3} excitation path.

Study I: Effect of Shockley-Hall-Read constant

The SHR constant A is related to the non-radiative process of monomolecular recombination which takes place through defects in the crystal lattice. SRH mechanisms has been shown to be a critical process affecting the injection efficiency of light emitting diodes [31].

As shown in figure 2.5, at low photon fluxes and current densities, the injection

efficiency is higher as the SRH constant is smaller. Such characteristic is expected, since lower values of SRH constant indicate lower non-radiative recombination rates of carriers in the active region and barrier. As a result, the injection efficiency in the GaN:Eu QW active region increases for optical and electrical model. Interestingly, it should be noted that the increase of the SHR constant A would lead to slower saturation of the excited Eu^{+3} concentration as the photon flux and current density is increasing. This indicates that additional carriers are required through optical excitation in the optically-pumped device or electrical injection in the electrically-driven device to replace the carriers lost in the monomolecular non-radiative recombination process. Thus, higher photon fluxes and current densities are required to result in same Eu^{+3} excitation as opposed to lower values of A.

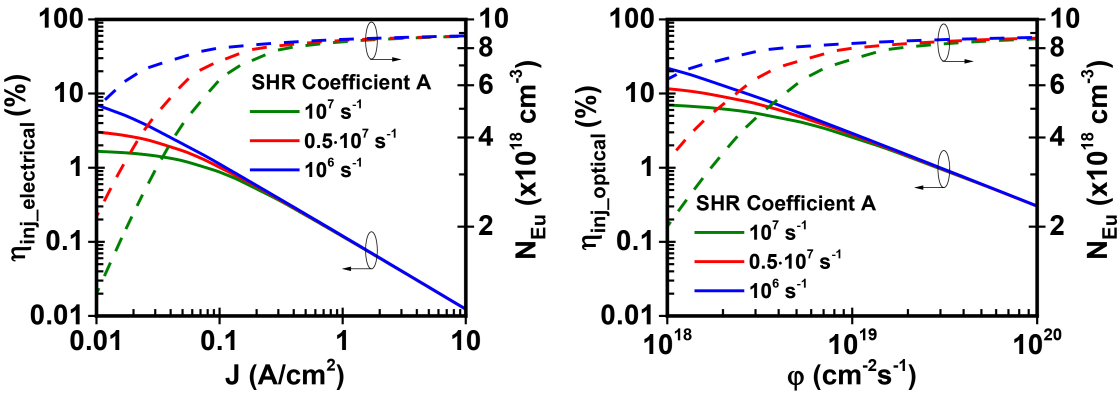

Figure 2.5: Effect of Shockley-Hall-Read constant A on injection efficiency and excited Eu^{+3} ion concentration of GaN:Eu QW active region. (a) Injection efficiency and excited Eu^{+3} ion concentration as a function of photon flux for optical model and (b) Injection efficiency and excited Eu^{+3} ion concentration as a function of current density for electrical model. The η_{IQE} is defined as $\eta_{\mathrm{IQE}} = \eta_{\mathrm{inj}}\ \eta_{\mathrm{rad}}$ and follows the same trend as the η_{inj} of the optical and electrical model.

Study II: Effect of capture time

The capture of carriers from traps with a rate $1/\tau_{\mathrm{cap0}}$ results in the creation of complexes. A general capture time $\tau_{\mathrm{c\_cap}}$ is given from equation (2.5) which is a function of the formed complexes (N_c).

Figure 2.6 shows the effect of capture time τ_{cap0} both for optical and electrical

model. Following the previous analysis, as the capture time decreases, the carriers are captured more efficiently from traps increasing the formation rate of complexes and consequently the excited Eu^{+3} concentration. This efficient capture of carriers from traps increase the injection efficiency and decrease the required amount of photon fluxes and current densities. This is observed as a shift towards lower photon fluxes and current densities of the excited Eu^{+3} concentration and injection efficiency for both models. For the optical model, the higher injection efficiency occurs for the lower capture time of $\tau_{\text{cap0}} = 10^{-7}\ s$ where the injection efficiency drops from $\eta_{\text{inj\_optical}} = 21\%$ to $\eta_{\text{inj\_optical}} = 0.2\%$. In contrast, for the electrical model it drops from $\eta_{\text{inj\_electrical}} = 9\%$ to $\eta_{\text{inj\_electrical}} = 0.01\%$.

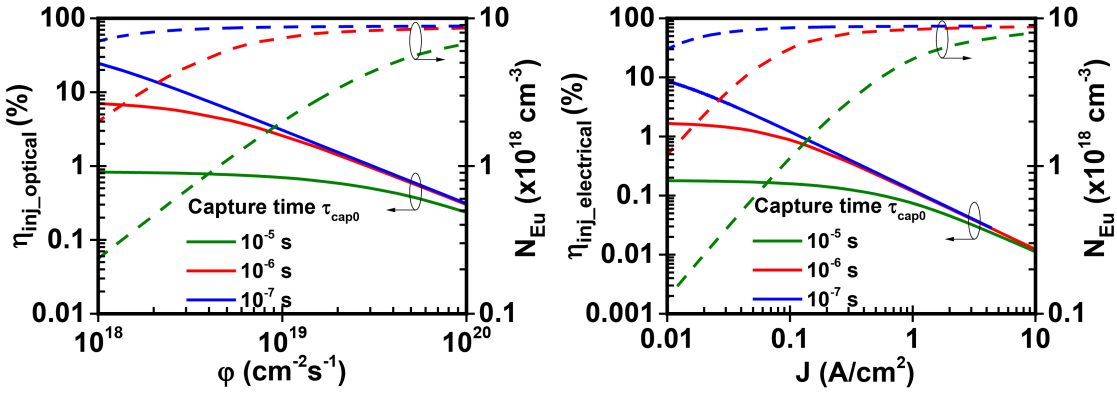

Figure 2.6: Effect of capture time τ_{cap0} on injection efficiency and excited Eu^{+3} ion concentration of GaN:Eu QW active region. (a) Injection efficiency and excited Eu^{+3} ion concentration as a function of photon flux for optical model and (b) Injection efficiency and excited Eu^{+3} ion concentration as a function of current density for electrical model. The η_{IQE} is defined as $\eta_{\text{IQE}} = \eta_{\text{inj}}\ \eta_{\text{rad}}$ and follows the same trend as the η_{inj} of the optical and electrical model.

Study III: Effect of transfer time

The transfer time defines the rate at which complexes de-excite by releasing energy to a nearby Eu^{+3} ion. As shown in figure 2.7, the injection efficiency increases as the transfer time τ_{tr0} decreases, which is a result of the faster de-excitation of the complexes. Equation (2.4) indicates that the de-excitation rate of complexes, $1/\tau_{\text{tr}}$, is essentially the excitation rate of Eu^{+3} ions. As a result, the higher excitation rates of

Eu^{+3} ions result in faster saturation of excited Eu^{+3} concentration under steady state conditions. This is observed as a shift toward lower photon fluxes (ϕ) and current densities (J) of the excited Eu^{+3} concentration. For the given range of photon flux and current density, the values of τ_{tr0} = 36 x 10^{-6} s and τ_{tr0} = 36 x 10^{-7} s result in saturation of excited Eu^{+3} concentration close to the value of Eu^{+3} ion concentration in the active region (N = 1 x 10^{19} cm^{-3}), while the value ofτ_{tr0} = 36 x 10^{-5} s results in saturation $N_{Eu} \approx$ 4 x 10^{18} cm^{-3} which is almost 40% of the total concentration of Eu^{+3} ion in the GaN:Eu QW active region.

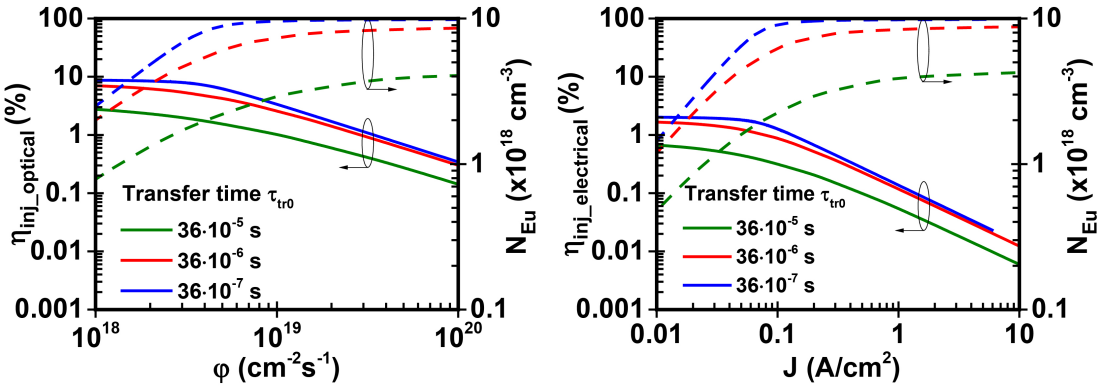

Figure 2.7: Effect of transfer time τ_{tr0} on injection efficiency and excited Eu^{+3} ion concentration of GaN:Eu QW active region. (a) Injection efficiency and excited Eu^{+3} ion concentration as a function of photon flux for optical model and (b) Injection efficiency and excited Eu^{+3} ion concentration as a function of current density for electrical model. The η_{IQE} is defined as $\eta_{IQE} = \eta_{inj}\ \eta_{rad}$ and follows the same trend as the η_{inj} of the optical and electrical model.

Study IV: Effect of complex dissociation rate and energy back-transfer rate

As stated before, the complexes can dissociate, releasing the captured electrons and holes into the QW with a rate of $1/\tau_{diss}$. Similarly, the excited Eu^{+3} ions can de-excite with a rate $1/\tau_{bt0}$ by releasing energy which results in the formation of complexes. Both dissociation time and back-transfer time are related to processes which can be considered as recycling mechanisms: in the case of dissociation process, the resulted electrons and holes can be re-captured from traps to form complexes, while in the back-transfer process the formed complexes can result to the excitation

of Eu^{+3} ions. For this study, five different values of back-transfer and dissociation rates are selected for a given current density $J = 0.87\ A/cm^2$ and photon flux of $\phi = 4$ x $10^{19}\ cm^{-2}s^{-1}$.

As it is shown in figure 2.8, by increasing the dissociation rate, the injection efficiency and excited Eu^{+3} concnetration drop significantly. More specifically, for the electrical model injection efficiency drops from $\eta_{\text{inj\_electrical}} = 0.18\%$ to almost $\eta_{\text{inj\_electrical}} = 0.001\%$, while for the optical model drops from $\eta_{\text{inj\_optical}} = 0.9\%$ to almost $\eta_{\text{inj\_optical}} = 0.01\%$. The changes in excited Eu^{+3} concnetration are identical for the two models.

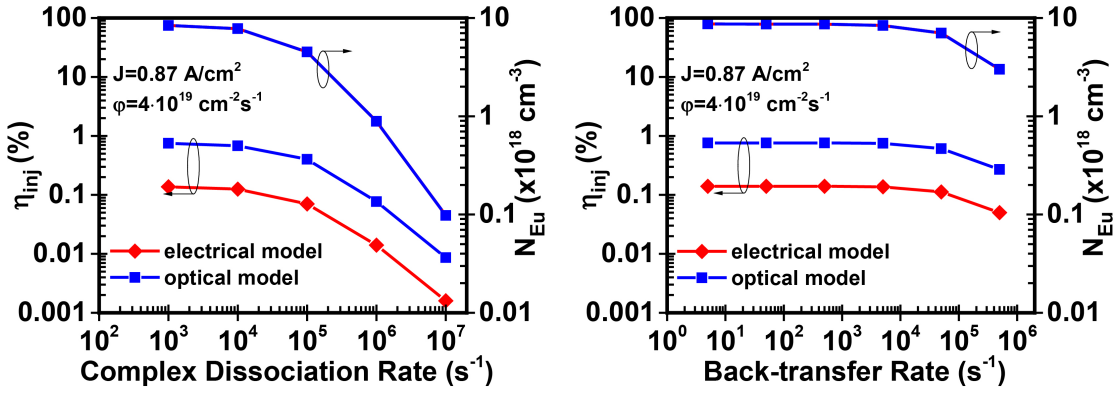

Figure 2.8: Injection efficiency and excited Eu^{+3} ion concentration of GaN:Eu QW active region as a function of (a) back-transfer rate $1/\tau_{bt0}$ and (b) dissociation rate 1/diss. The η_{IQE} is defined as $\eta_{\text{IQE}} = \eta_{\text{inj}}\ \eta_{\text{rad}}$ and follows the same trend as the η_{inj} of the optical and electrical model. The two models are compared for the same values of Eu^{+3} excited ion concentration in the GaN:Eu QW active region

A droop in the injection efficiency and excited Eu^{+3} concentration with the back-transfer rate is also observed for both models. More specifically, the droop starts when the back-transfer rate of $1/\tau_{\text{bt0}} = 5$ x $10^4\ s^{-1}$ becomes comparable with the transfer rate of complexes, $1/\tau_{\text{tr0}} = 2.77$ x $10^4\ s^{-1}$. For back-transfer rates lower than $1/\tau_{\text{bt0}} = 5$ x $10^4\ s^{-1}$, the injection efficiency and excited Eu^{+3} concentration remain unaffected.

In addition, the changes in the injection efficiency and excited Eu^{+3} concnetration with the back-transfer rate, are smaller as compared to the changes with the complex

dissociation rate. As it can be seen from figure 2.4, the level at which the dissociation process takes place is distant from the level of Eu^{+3} ion. Thus, the carriers resulted from the dissociation of complexes have higher probability to deviate from the Eu^{+3} excitation path reducing in that way the injection efficiency and the excited Eu^{+3} concentration in the GaN:Eu QW active region.

Study V: Effect of radiative lifetime of Eu^{+3} ion – Enhancement of radiative efficiency

The parameters presented in the previous sections affect the internal quantum efficiency of the system by altering only the injection efficiency in the active region. The internal quantum efficiency is calculated from equation (2.14) with a radiative efficiency fixed at $\eta_{\text{rad}} \approx 72\%$ and follows the same trend of the injection efficiency. The radiative lifetime (τ_{rad}) and the non-radiative time ($\tau_{\text{Eu\_heat}}$) of Eu^{+3} ion determine the radiative efficiency of the GaN:Eu QW system. Lower radiative lifetime results in higher radiative efficiencies, assuming that the non-radiative lifetime of Eu^{+3} ion remains unchanged.

By reducing the radiative lifetime, the injection efficiency and excited Eu^{+3} concentration are significantly altered. The lower radiative lifetime indicates faster radiative de-excitation rate of excited Eu^{+3} ions, therefore, higher injection efficiency can be achieved at a given photon flux and current density. This is clearly illustrated in figure 2.9. In addition, the resulted lower saturation values of excited Eu^{+3} ions, make the injection efficiency to be strongly altered at higher photon fluxes and current densities.

Attributed to the differences in the complex interplays among the fundamental processes in the current injection process, the optical model exhibits higher injection efficiency as compared to the electrical model for the same values of excited Eu^{+3} concentration. In particular, the reduction of radiative lifetime from $\tau_{\text{rad}} = 400$ μs to $\tau_{\text{rad}} = 30$ μs, changes the excited Eu^{+3} concentration from $N_{Eu} = 8.4$ x 10^{18} cm^{-3}

to N_{Eu} = 3.25 x 10^{18} cm^{-3} at a given ϕ = 4.7 x 10^{18} cm^{-3}. Meanwhile, injection efficiency increases from $\eta_{\text{inj\_optical}}$ = 0.62% to $\eta_{\text{inj\_optical}}$ = 2.4% which is 3.8 times higher. A similar change in the excited Eu^{+3} concentration occurs at $J = 1\ A/cm^2$ for the electrical model while the injection efficiency increases from $\eta_{\text{inj\_electrical}}$ = 0.12% to $\eta_{\text{inj\_electrical}}$ = 0.46% which is almost 3.8 times higher, same change as in the optical model. The reduction of the radiative lifetime is essential for achieving higher injection efficiencies at higher photon fluxes and current densities, while at the same time the radiative efficiency of Eu^{+3} ions is enhanced.

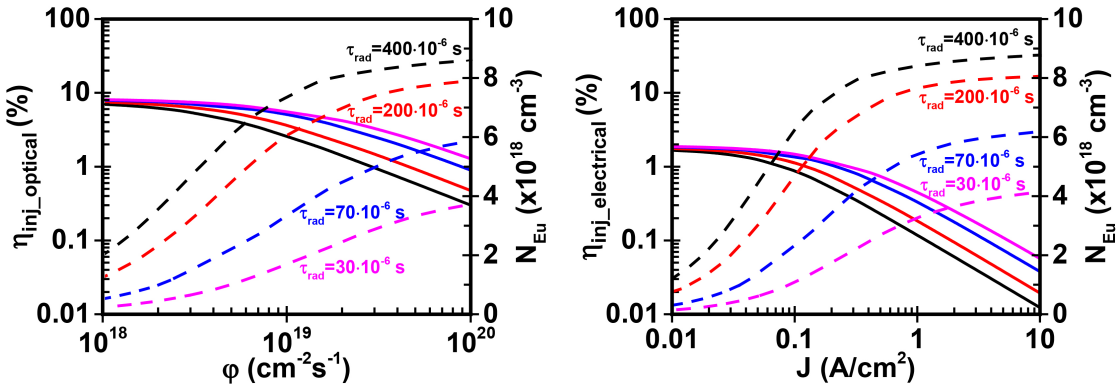

Figure 2.9: Effect of radiative lifetime trad of Eu^{+3} ion on injection efficiency and excited Eu^{+3} ion concentration of GaN:Eu QW active region. (a) Injection efficiency and excited Eu^{+3} ion concentration as a function of photon flux for optical model and (b) Injection efficiency and excited Eu^{+3} ion concentration as a function of current density for electrical model. The η_{IQE} follows the same trend as the η_{inj} for the optical and electrical model. The non-radiative lifetime of Eu^{+3} ion is set to $\tau_{\text{Eu\_heat}} = 1ms$. Different radiative lifetimes correspond to different radiative efficiencies. For τ_{rad} = 400μs the radiative efficiency is η_{rad} =71.43%. Similarly, for τ_{rad} = 200 μs / η_{rad} = 83.3%, for τ_{rad} = 7 μs / η_{rad} = 93.46%, and for τ_{rad} = 30 μs / η_{rad} = 97.09%.

2.3.6 Comparison with experimentally reported data

In order to compare the present work with experimentally reported values of GaN:Eu devices, the external quantum efficiency (η_{EQE}) for a GaN:Eu QW LED with a square device area of 1000 x 1000 μm is calculated. The external quantum efficiency is the product of the extraction efficiency (η_{extr}) and the internal quantum efficiency

of the device. An extraction efficiency of $\eta_{\text{extr}} = 44\%$ was used for thes calculations, which is a typical value for GaN:Eu based device [19]. The details of each simulation are given in Table 2.2 (Group A) and Table 2.3 (Group B). The numerical calculations for the external quantum efficiency are divided into two groups: Group A represents those which resulted in $\eta_{\text{EQE}} > 1\%$ and Group B represents those which resulted in $\eta_{\text{EQE}} < 1\%$.

Parameters	Simulation I	Simulation II	Simulation III	Simulation IV
$A\ (s^{-1})$	0.5×10^8	10^6	10^6	10^6
$\tau_{\text{cap0}}\ (s)$	10^{-7}	10^{-7}	10^{-8}	10^{-8}
$\tau_{\text{tr0}}\ (s)$	36×10^{-6}	36×10^{-6}	36×10^{-7}	36×10^{-7}
$\tau_{\text{bt0}}\ (s)$	200 x 10^{-6}	200×10^{-6}	200×10^{-6}	200×10^{-6}
$\tau_{\text{diss}}\ (s)$	10^{-3}	10^{-3}	10^{-3}	10^{-3}
$\tau_{\text{c\_heat}}$, $\tau_{\text{Eu\_heat}}\ (s)$	10^{-3}, 10^{-3}	10^{-3}, 10^{-3}	10^{-3}, 10^{-3}	10^{-3}, 10^{-3}
$\tau_{\text{rad}}\ (s)$	200×10^{-6}	200×10^{-6}	200×10^{-6}	100×10^{-6}
$N\ (cm^{-3})$	8.5×10^{19}	8.5×10^{19}	8.5×10^{19}	8.5×10^{19}
$N_{traps}\ (cm^{-3})$	8.5×10^{19}	8.5×10^{19}	8.5×10^{19}	8.5×10^{19}
L_{QW}, L_{Eu}, $L_B\ (nm)$	5, 5, 10	5, 5, 10	5, 5, 10	5, 5, 10

Table 2.2: Simulations of external quantum efficiency (EQE) for a GaN:Eu QW device-high EQE.

Parameters	Simulation I	Simulation II	Simulation III	Simulation IV
$A\ (s^{-1})$	10^6	10^6	10^6	10^6
$\tau_{\text{cap0}}\ (s)$	10^{-4}	10^{-6}	10^{-6}	10^{-6}
$\tau_{\text{tr0}}\ (s)$	36×10^{-6}	36×10^{-6}	36×10^{-4}	36×10^{-6}
$\tau_{\text{bt0}}\ (s)$	200 x 10^{-6}	200×10^{-6}	200×10^{-6}	200×10^{-8}
$\tau_{\text{diss}}\ (s)$	10^{-3}	10^{-6}	10^{-3}	10^{-3}
$\tau_{\text{c\_heat}}$, $\tau_{\text{Eu\_heat}}\ (s)$	10^{-3}, 10^{-3}	10^{-3}, 10^{-3}	10^{-3}, 10^{-3}	10^{-3}, 10^{-3}
$\tau_{\text{rad}}\ (s)$	200×10^{-6}	200×10^{-6}	200×10^{-6}	100×10^{-6}
$N\ (cm^{-3})$	8.5×10^{19}	8.5×10^{19}	8.5×10^{19}	8.5×10^{19}
$N_{traps}\ (cm^{-3})$	8.5×10^{19}	8.5×10^{19}	8.5×10^{19}	8.5×10^{19}
L_{QW}, L_{Eu}, $L_B\ (nm)$	5, 5, 10	5, 5, 10	5, 5, 10	5, 5, 10

Table 2.3: Simulations of external quantum efficiency for a GaN:Eu QW device-low EQE.

Figure 2.10(a) presents the numerical calculations form the CIE model and the experimentally reported values of two different types of GaN:Eu based LED. A. Nishikawa and co-workers fabricated two GaN:Eu based LEDs with a 300 nm GaN:Eu

active layer each, under different growth conditions [15]. They reported an external quantum efficiency of $\eta_{\mathrm{EQE}} = 0.6\%$ at an injected current of 0.5 mA which was found to reduce to $\eta_{\mathrm{EQE}} = 0.04\%$ at 20 mA. W. Zhu and co-workers fabricated a GaN:Eu based LED with an active layer of alternate GaN/GaN:Eu regions and they reported an external quantum efficiency of $\eta_{\mathrm{EQE}} = 4.6\%$ at an injected current of 1 mA which reduced to $\eta_{\mathrm{EQE}} = 0.9\%$ at 20 mA [20]. These values correspond to the highest reported external quantum efficiency up to date. The calculated EQE from the electrical current injection efficiency model, follows the same trend as the experimentally reported values. In addition, both experimental studies revealed that higher injected current into the GaN:Eu device led to saturation in the electroluminescence spectrum, which was attributed to the saturation of the excited Eu^{+3} ions. Similar findings have also been reported elsewhere [16,18]. The present study is consistent with the experimental observations that increasing the injected current will eventually result in the saturation of the excited Eu^{+3} concentration with a subsequent decrease in the injection efficiency and internal quantum efficiency the GaN:Eu QW active region.

2.4 CIE Model for a GaN/GaN:Eu homojunction

Here, a CIE model is developed for electrically-driven GaN:Eu device with a GaN/GaN:Eu/GaN active region to identify the limiting factors of the internal quantum efficiency (η_{IQE}) and explain the efficiency droop issue of this particular type of active region. This type of structure is fundamentally different from the structure investigated in the previous section on quantum well based active region. The present model provides the analysis of the current injection efficiency and IQE in the structures pursued by experimentalists [20], specifically the active region with GaN/GaN:Eu alternate layers where the active regions (GaN:Eu) are not confined by

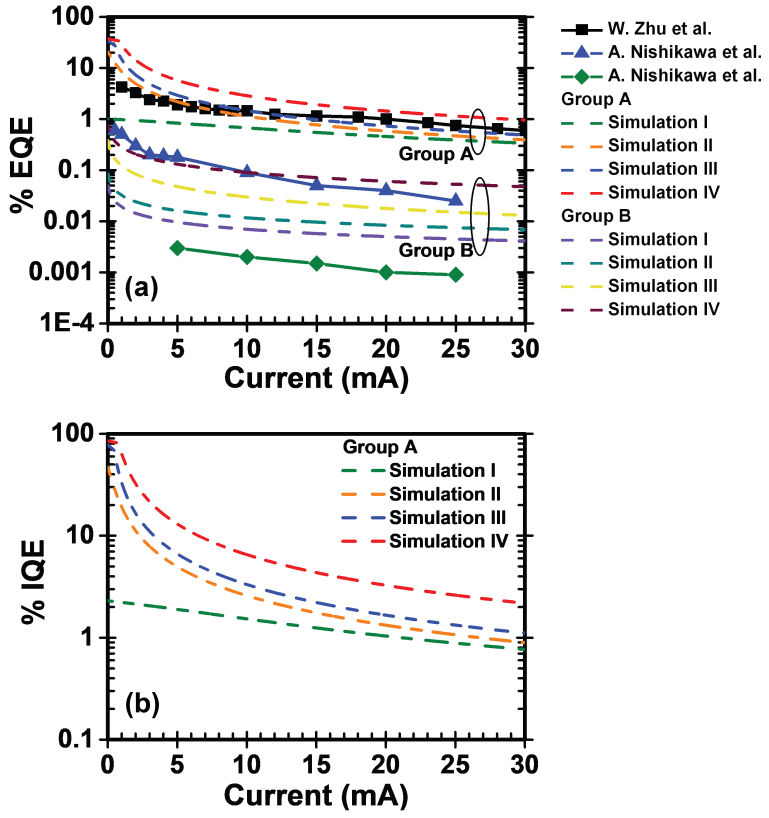

Figure 2.10: (a) EQE calculated from the electrical CIE model of GaN:Eu QW device and experimentally reported values of GaN:Eu based LED. (b) Calculated IQE for the electrically-driven GaN:Eu QW device. The simulation parameters are shown in table 2(a).

larger band-gap barrier systems. Such structure presented a very different challenge, which also required a completely different physics of carrier transport – beyond the QW model. This present model is important for enabling the direct comparison with the experimental devices.

2.4.1 Model formulation

Figure 2.11 depicts the GaN/GaN:Eu/GaN active region structure and the related carrier mechanisms along the Eu^{+3} excitation path. According to this model, radiative and non-radiative recombination processes of carriers exist both in GaN and GaN:Eu regions. These fundamental processes are described through the Auger

and the Shockley-Hall-Read (SHR) recombination processes (non-radiative) and the bimolecular recombination process (radiative) in the semiconductors. In addition, carrier transport mechanisms across the structure are present which are described through the ambipolar diffusion carrier transport across the GaN and GaN:Eu regions [289,29,31,41].

The development of the current injection efficiency model for the GaN:Eu / GaN based LED is developed here, and the framework follows the treatments presented for III-V [28,29] and GaN-based [31] lasers / LEDs. The rate equations of carriers in the GaN region (N_1) and GaN:Eu region (N_2) are given by:

$$\frac{dN_1}{dt} = \frac{I_{tot}}{q\ V_1} + \frac{N_2}{\tau_{r2}}\frac{V_2}{V_1} - N_1\left(\frac{1}{\tau_{nr1}} + \frac{1}{\tau_{sp1}} + \frac{1}{\tau_{r1}}\right) \tag{2.20}$$

$$\frac{dN_2}{dt} = \frac{N_1}{\tau_{r1}}\frac{V_1}{V_2} + \frac{N_{ex}}{\tau_{diss}} - N_2\left(\frac{1}{\tau_{nr2}} + \frac{1}{\tau_{sp2}} + \frac{1}{\tau_{r2}} + \frac{1}{\tau_{cap}}\right) \tag{2.21}$$

with the rate $1/\tau_{\mathrm{cap}}$ defined as

$$\frac{1}{\tau_{cap}} = \frac{1}{\tau_{cap0}}\left(1 - \frac{N_{ex}}{N_{traps}}\right) \tag{2.22}$$

The I_{tot} is the total current injected into the GaN region from the n- and p-cladding layers of device. The parameters, N_{ex} and N_{traps}, denote the bound-excitons and the maximum available trap concentration in the GaN:Eu region, respectively, and the τ_{cap0} is the capture time at the low regime where $N_{ex}<<N_{traps}$. In equations (2.20) and (2.21), the V_1 and V_2 are the volumes of the GaN and GaN:Eu regions respectively. The rates $1/\tau_{\mathrm{nr1}}$, $1/\tau_{\mathrm{sp1}}$, $1/\tau_{\mathrm{nr2}}$ and $1/\tau_{\mathrm{sp2}}$ are the non-radiative and spontaneous radiative recombination rates in the GaN (subscript 1) and GaN:Eu (subscript 2) regions, respectively. These rates are described by the SHR recombination constants A, the Auger coefficient C, and the bimolecular recombination constant B in the semiconductors. The rates $1/\tau_{\mathrm{r1}}$ and $1/\tau_{\mathrm{r2}}$ are described by the ambipolar

diffusion carrier transport time in the GaN and GaN:Eu regions respectively. The rate equations of bound-excitons and excited Eu^{+3} ion concentration are given by:

$$\frac{dN_{ex}}{dt} = N_2\frac{1}{\tau_{cap}} + N_{Eu}\frac{1}{\tau_{bt}} - N_{ex}\left(\frac{1}{\tau_{tr}} + \frac{1}{\tau_{diss}} + \frac{1}{\tau_{ex\_heat}}\right) \tag{2.23}$$

$$\frac{dN_{Eu}}{dt} = N_{ex}\frac{1}{\tau_{tr}} - N_{Eu}\left(\frac{1}{\tau_{bt}} + \frac{1}{\tau_{rad}} + \frac{1}{\tau_{Eu\_heat}}\right) \tag{2.24}$$

The rates $1/\tau_{\mathrm{tr}}$ and $1/\tau_{\mathrm{bt}}$ are defined in an equivalent manner as in the equation (2.22):

$$\frac{1}{\tau_{tr}} = \frac{1}{\tau_{tr0}}\left(1 - \frac{N_{Eu}}{N}\right) \tag{2.25}$$

$$\frac{1}{\tau_{bt}} = \frac{1}{\tau_{bt0}}\left(1 - \frac{N_{ex}}{N_{traps}}\right) \tag{2.26}$$

where the N_{Eu} and N are the excited and the maximum concentrations of Eu^{+3} ions in the GaN:Eu region, respectively. The current injection efficiency (η_{inj}) is defined as the ratio of the current arising from the radiative and non-radiative de-excitation of Eu^{+3} ions over the total current I_{tot}, entering the device:

$$\eta_{injection} = \frac{I_{Eu}}{I_{tot}} \tag{2.27}$$

The I_{Eu} corresponds to the total recombination current arising from the radiative and non-radiative de-excitation of the Eu^{+3} ion in the GaN:Eu region:

$$I_{Eu} = \frac{N_{Eu}\ q\ V_{Eu}}{\tau} \tag{2.28}$$

with q as the electron charge, and the lifetime has both contributions from the radiative and non-radiative processes as stated below:

$$\frac{1}{\tau} = \frac{1}{\tau_{rad}} + \frac{1}{\tau_{Eu\_heat}} \tag{2.29}$$

By solving the rate equations (2.20), (2.21), (2.23), and (2.24) under steady state conditions and using the equation (2.27), the current injection efficiency for the GaN:Eu / GaN LED can be expressed as:

$$\eta_{injection} = \left[\left(\frac{L_1}{L_2} \right) \left(b + \frac{b}{\left(\frac{1}{\tau_{r1}} + \frac{1}{\tau_{sp1}} + \frac{1}{\tau_{nr1}} \right)^{-1}} - \left(\frac{L_2}{L_1} \right) \frac{c}{\tau_{r2}} \right) \right]^{-1} \tag{2.30}$$

with

$$b = \frac{L_2}{L_1} \left(a - \frac{\left(\frac{1}{\tau_{rad}} + \frac{1}{\tau_{Eu\_heat}} \right)^{-1} \tau_{tr}}{\left(\frac{1}{\tau_{rad}} + \frac{1}{\tau_{Eu\_heat}} + \frac{1}{\tau_{bt}} \right)^{-1} \tau_{diss}} \right) \tau_{r1} \tag{2.31}$$

$$a = \left(\frac{c}{\left(\frac{1}{\tau_{r2}} + \frac{1}{\tau_{sp2}} + \frac{1}{\tau_{nr2}} + \frac{1}{\tau_{cap}} \right)^{-1}} \right) \tag{2.32}$$

$$c = \left(\left(\frac{\left(\frac{1}{\tau_{rad}} + \frac{1}{\tau_{Eu\_heat}} \right)^{-1} \tau_{tr}}{\left(\frac{1}{\tau_{rad}} + \frac{1}{\tau_{Eu\_heat}} + \frac{1}{\tau_{bt}} \right)^{-1} \left(\frac{1}{\tau_{diss}} + \frac{1}{\tau_{ex\_heat}} + \frac{1}{\tau_{tr}} \right)^{-1}} - \frac{\left(\frac{1}{\tau_{rad}} + \frac{1}{\tau_{Eu\_heat}} \right)^{-1}}{\tau_{bt}} \right) \tau_{cap} \right) \tag{2.33}$$

where, the L_1 and L_2 are the lengths of the GaN and GaN:Eu regions respectively. Then, the internal quantum efficiency (η_{IQE}) of the rare-earth doped GaN LED is given by:

$$\eta_{IQE} = \eta_{injection}\ \eta_{rad} \tag{2.34}$$

where, the η_{rad} is the radiative efficiency of the Eu^{+3} ions defined as the ratio of

radiative to both radiative and non-radiative de-excitation of Eu^{+3} ions:

$$\eta_{rad} = \frac{N_{Eu}/\tau_{rad}}{N_{Eu}/\tau} = \frac{\frac{1}{\tau_{rad}}}{\frac{1}{\tau_{rad}} + \frac{1}{\tau_{Eu\_heat}}} \tag{2.35}$$

2.4.2 Simulation results

As for the case of the GaN:Eu based QW, the study of the injection efficiency in the GaN:Eu/GaN homojunctions is similar. The material parameters used for the simulations, such as SHR recombination constant A, bimolecular recombination constant B, Auger coefficient C, electron and hole effective masses and mobilities can be found in reference [31]. For this work the values of material parameters both for the GaN and GaN:Eu region are assumed to be the same. In addition, for the magnitude of the relative times related to traps, bound-excitons and Eu^{+3} ions, the experimental results described in [39,40] were used as a point of reference. Despite the fact that the two models (the GaN:Eu based QW and the GaN/GaN:Eu/GaN) are physically and fundamentally different (the excitation path is governed by different mechanisms), the effect of the Shockley-Hall-Read constant A, capture time τ_{cap0}, transfer time τ_{tr0} and radiative lifetime of Eu^{+3} ion τ_{rad}, on the injection efficiency and excited Eu^{+3} ion population is similar as in the case of the GaN:Eu based QW. However in this section, only the effect of the length of the GaN:Eu and GaN regions on the current injection efficiency and excited Eu^{+3} ion population is presented. In addition, the effect of the carrier confinement is also presented with respect to the GaN/GaN:Eu/GaN structure.

Study: Effect of GaN and GaN:Eu region lengths

The effect of the lengths of the GaN and GaN:Eu regions is depicted in figure 2.11. As it is shown, the increase of the GaN length (L_{GaN}) reduces the current injection efficiency ($\eta_{\mathrm{injection}}$) and excited Eu^{+3} ion concentration. In contrast, an increase in

the GaN:Eu length ($L_{GaN:Eu}$) will give rise to the current injection efficiency ($\eta_{\text{injection}}$) as well as to the excited Eu^{+3} ion concentration under steady state conditions. The change in the lengths of the two regions affects the ambipolar diffusion transport time (τ_{r1}, τ_{r2}) of carries across the structure. For higher L_{GaN}, the carriers require more time to be transported across the GaN region, reducing the rate at which they arrive in the GaN:Eu region. As a result, the current injection efficiency ($\eta_{\text{injection}}$) and excited Eu^{+3} ion concentration in the active region are decreased. In contrast, for higher $L_{GaN:Eu}$, the ambipolar diffusion transport time in the GaN:Eu region (τ_{r2}) will be increased giving rise to the carrier concentration in the GaN:Eu region. The increased carrier concentration in the GaN:Eu region will result in higher probability of bound-exciton formation. Consequently, the excited Eu^{+3} ion concentration and the current injection efficiency ($\eta_{\text{injection}}$) are increased.

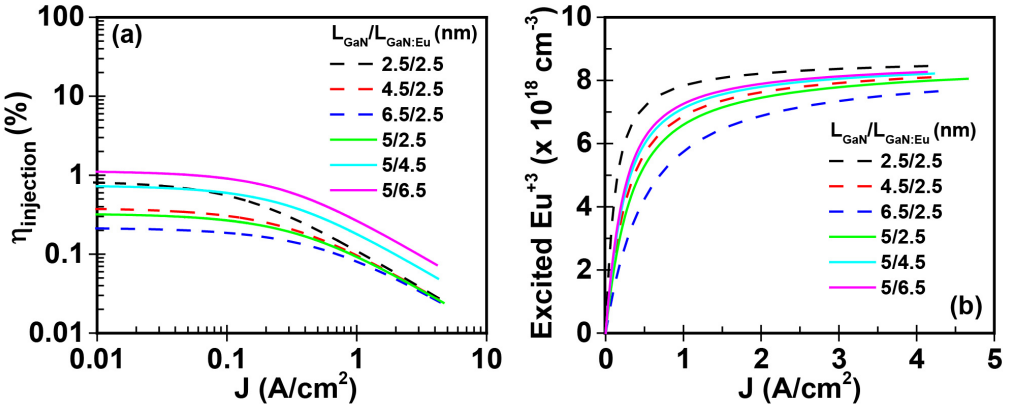

Figure 2.11: Effect of GaN and GaN:Eu region lengths ($L_{GaN}/L_{GaN:Eu}$) on (a) current injection efficiency ($\eta_{\text{injection}}$) and (b) excited Eu^{+3} ion concentration of the GaN:Eu region. The dashed lines correspond to changes in the length of the GaN region (L_{GaN}) with a fixed $L_{GaN:Eu} = 2.5\ nm$. Similarly, the solid lines corresponds to changes in the length of the GaN:Eu region ($L_{GaN:Eu}$) with a fixed $L_{GaN} = 5\ nm$

Study: Effect of carrier confinement in the GaN:Eu region

The utilization of heterostructures such as $Al_xGa_{1-x}N$/GaN:Eu/$Al_xGa_{1-x}N$ increases the carrier confinement in the GaN:Eu quantum well (QW) region, enhancing in that way the excitation probability of Eu^{+3} ions. In addition, the replace-

ment of the GaN/GaN:Eu/GaN structure with the $Al_xGa_{1-x}N$/GaN:Eu/$Al_xGa_{1-x}N$ heterostructure results in different carrier processes (figure 2.12). These additional processes include the quantum mechanical capture process of carriers from the barrier to the QW and the thermionic carrier escape process from the GaN:Eu QW to the $Al_xGa_{1-x}N$ barriers. The analysis of the $Al_xGa_{1-x}N$/GaN:Eu/$Al_xGa_{1-x}N$ heterostructure has already been provided in the previous sections. The effect of the carrier confinement on the current injection process in RE-doped GaN LED is shown in figure 2.13. The presence of the GaN:Eu quantum well (QW) confined within $Al_xGa_{1-x}N$ barriers increases the current injection efficiency ($\eta_{\text{injection}}$) and the excited Eu^{+3} ion concentration at a given current density. The carrier confinement in the QW increases the carrier density near the Eu^{+3} ions and thus, the probability of carrier capture form traps increases, giving rise to the excitation of Eu^{+3} ions. In addition, increasing the Al composition of the $Al_xGa_{1-x}N$ barrier increases the barrier height, which results in the suppression of the thermionic carrier escape process [31]. As a result, the current injection efficiency ($\eta_{\text{injection}}$) and excited Eu^{+3} ion concentration in the active region are increased. The effect of carrier confinement, has been demonstrated by T. Arai et al. [18], where they showed an increase of the PL intensity of a AlGaN/GaN:Eu/AlGaN multiple QW structure as compared to a rudimentary GaN:Eu based light emitter. Similar findings have been demonstrated for Erbium-doped GaN based heterostructures, where the effect of carrier confinement increases the luminescence of the GaN:Er emitter [42,43].

2.4.3 Comparison with experiment

The results from the CIE model are compared with the experimentally reported values. More specifically, the external quantum efficiency (η_{EQE}) of a GaN/GaN:Eu/GaN structure is calculated. The external quantum efficiency (η_{EQE}) is defined as the product of the internal quantum efficiency (η_{IQE}) and the extraction efficiency (η_{EXT}) of

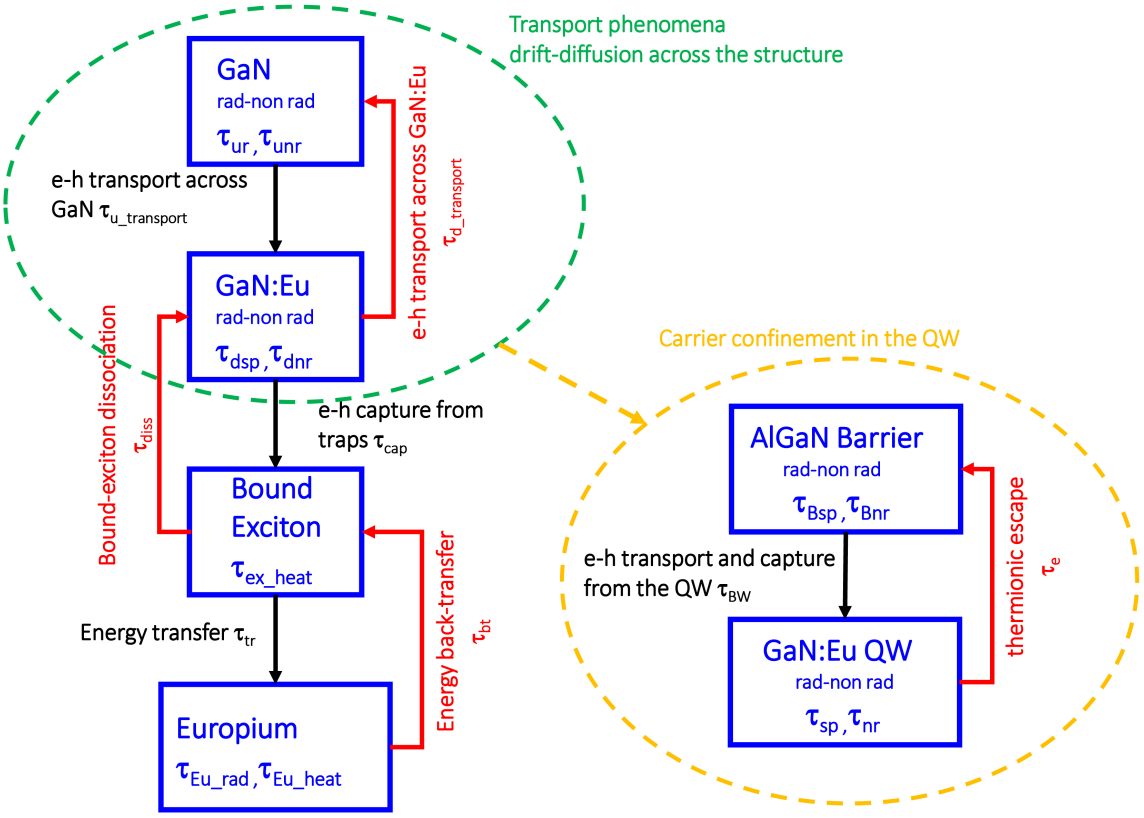

Figure 2.12: Active region structures for GaN:eu based device. The $Al_xGa_{1-x}N$ / GaN:Eu heterostructures result in the formation of GaN:Eu quantum well (QW). This QW structure results in quantum mechanical processes such as the capture of carriers form the barrier to the QW as well as to the thermionic carrier escape form the QW to the barrier. The carrier confinement give rise to the carrier concentration inside the GaN:Eu QW which in turns enhances the excitation probability of Eu^{+3} ions.

the device. For the purpose of these calculations, a device area of 0.1 x 0.1 cm^2 with an external quantum efficiency of $\eta_{\mathrm{EXT}} = 44\%$ was used, which is a typical value of the GaN:Eu based devices [19]. W. Zhu and co-workers fabricated a high power GaN:Eu based LED via low temperature OMVPE technique [20]. The active region of this device consisted of alternate GaN (6 nm) and GaN:Eu (3 nm) regions and exhibited an external quantum efficiency of $\eta_{\mathrm{EQE}} = 4.6\%$ at an injected current of 1 mA which was reduced to $\eta_{\mathrm{EQE}} = 0.9\%$ at 20 mA. These values correspond to the highest reported external quantum efficiency (η_{EQE}) for a GaN:Eu based device up

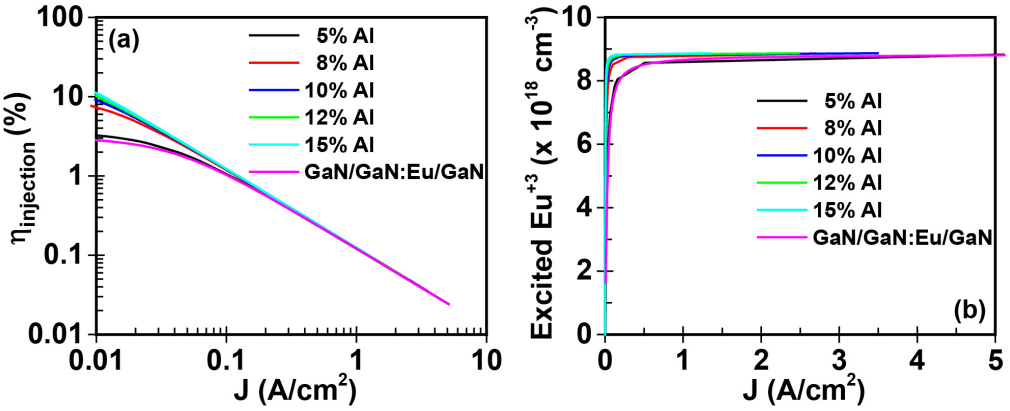

Figure 2.13: Effect of carrier confinement on (a) current injection efficiency ($\eta_{\text{injection}}$) and (b) excited Eu^{+3} ion concentration of the GaN:Eu active region. Higher Al percentage in the $Al_xGa_{1-x}N$ barrier results in the suppression of the thermionic emission of carriers form the GaN:Eu QW to the $Al_xGa_{1-x}N$ barrier.

to date.

Figure 2.14 presents the numerical fitting results to the experimentally reported values from W. Zhu et al. [20]. The simulation parameters used here are presented in Table 2.4. The simulation results provided an excellent fit with the experimental data from reference 23, as shown in figure 2.14. In order to guide the experiments, two cases (Case I and Case II) with different design parameters are investigated. In Case I (figure 219), by increasing the length of the GaN:Eu region from 3 nm to 6 nm, an increase of the external quantum efficiency (η_{EQE}) with respect to the fitting of the experimental data is possible. More specifically, an increase of 167%, 112% and 103% at an injected current of 5 mA, 15 mA and 30 mA respectively, is predicted. In Case II, by an additional decrease of the radiative lifetime of Eu^{+3} ion from τ_{rad} =100 μs to τ_{rad} = 70 μs, an increase of 173% and 183% at 15 mA and 30 mA respectively, is possible.

The experimental work by W. Zhu et al., showed that increasing the current into the GaN:Eu device, will eventually result in the saturation of the output light power of the device, as well as, in the decrease of the external quantum efficiency (η_{EQE}).

The saturation in the output power is a result of the saturation of the excited Eu^{+3} ions in the active region. The present work has showed that this saturation causes the efficiency droop issue in the GaN:Eu devices. Similar results have been experimentally verified elsewhere [15,16,18].

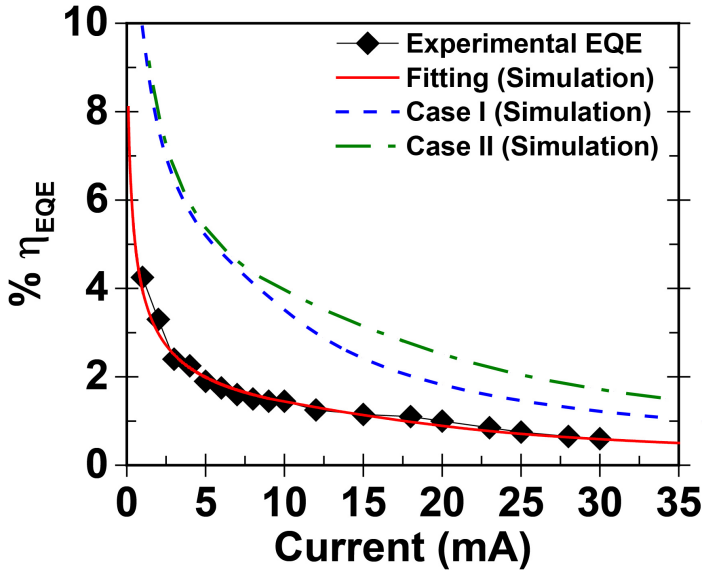

Figure 2.14: Experimentally reported values for a GaN:Eu device and the fitting with the CIE model. Two simulations for higher external quantum efficiency are performed. The increase at the particular current, is calculated with respect to the fitting of the experimental values.

Parameters	Fitting	Case I	Case II
A $(10^{8}\ s^{-1})$	0.01	0.01	0.01
τ_{cap0} $(10^{-8}\ s)$	10	10	10
τ_{tr0} $(10^{-7}\ s)$	0.36	0.36	0.36
τ_{diss} $(10^{-6}\ s)$	1000	1000	1000
τ_{bt0} $(10^{-6}\ s)$	200	200	200
$\tau_{\text{ex\_heat}}$ $(10^{-3}\ s)$	1	1	1
$\tau_{\text{Eu\_heat}}$ $(10^{-3}\ s)$	1	1	1
τ_{rad} $(10^{-6}\ s)$	100	100	70
N $(10^{19}\ cm^{-3})$	8.7	8.7	8.7
N_{traps} $(10^{-19}\ cm^{-3})$	8.7	8.7	8.7
L_{GaN}, $L_{GaN:Eu}$ (nm)	6, 3	6, 6	6, 3

Table 2.4: Parameters used for the fitting of the experimental values of the GaN:Eu device and the simulations for higher external quantum efficiency (η_{EQE})

2.5 Key findings of the CIE models - Remarks

Following the analysis of the CIE models it was identified that the saturation of the excited Eu^{+3} ions is the main reason for the efficiency droop issue. However, the saturation rate (how fast or how slow) of the excited Eu^{+3} ions will define the values of the current injection efficiency and consequently the internal and external quantum efficiencies of the emitter. Following the analysis presented in this thesis, it can be stated that the bottleneck for the low efficiency of the GaN:Eu emitter can be divided into two parts: the efficiency bottleneck a) at the low current regime and b) at the high current regime. Figure 2.15 summarizes the key findings.

Regarding the low current regime it was shown that the SHR recombination process of carriers at crystal defects, the capture process of free carries from traps in order to form the bound-exciton, as well as, the energy transfer process from the bound-excitons to the Eu^{+3} ions, are the main contributing factors for the low efficiency. For the high current regime, the radiative life time of the Eu^{+3} ion plays the major role. The lower the radiative lifetime, the faster the radiative de-excitation of the Eu^{+3} ions, which means that higher current densities can be used to excite more Eu^{+3} ions and hence increase the current injection efficiency at that particular current density.

A more intuitive approach into these mechanisms, at the low current regime, would reveal that the capture process and the SHR process - which both take place inside the GaN:Eu region- are two competing processes. Note that both processes (capture and SHR processes) are accounted for analyzing the dynamics of the carriers within the GaN:Eu layer. In addition, the transfer process takes place between the bound-exciton and the Eu^{+3} ion. As described from the rate equations of the carriers in the GaN:Eu region in the previous sections it can be clearly seen that under steady state conditions the SHR recombination process competes with the capture process of carriers from the traps which are in the vicinity of the Eu^{+3} ion. In the case where the

SHR recombination rate is large (high value of A) compared to the capture process of carriers from traps (to form a bound-exciton), the carrier loss rate into this mechanism will be very high compared to the capture rate of carrier from traps. This means that many carriers are lost into the non-radiative process of the SHR, while some of them will contribute to the formation of the bound-exciton. In an ideal case where the non-radiative recombination process SHR would be negligible or non-existent (very high GaN crystal quality), a large fraction of the carriers in the GaN:Eu region would result to the bound-exciton formation, which in turn would significantly increase the current injection efficiency. However, no matter how "efficient" the bound-excitons are formed not all of them will result to the excitation of the Eu^{+3} ions via the transfer process. As it has been mentioned previously, there other competing processes in the bound-exciton level (such as the dissociation and the non-radiative recombination process of the bound-exciton) that would take place.

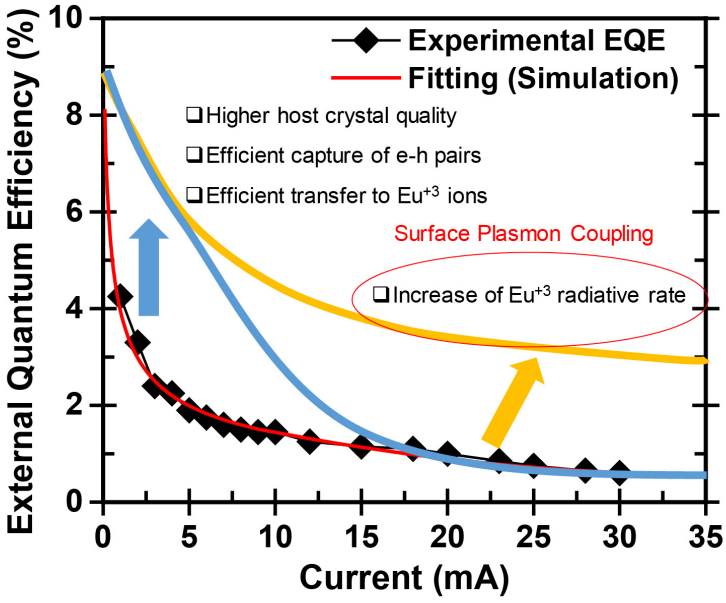

Figure 2.15: Simulated experimental EQE values [20] and the desirable improvement on the EQE (orange line). The orange line represents the EQE for an optimized device that would be suitable for technological applications. Arrows indicate the key points for EQE improvement at low and high current regimes.

2.6 IQE droop suppression remedies

Based on the previous analysis, several experimental pathways on how to increase the internal quantum efficiency (η_{IQE}) of the GaN:Eu based devices, including strategies for suppressing droop are presented. In figure 2.16, the internal quantum efficiency (η_{IQE}) is decomposed into two components, namely the current injection ($\eta_{\mathrm{injection}}$) and radiative ($\eta_{\mathrm{rad}}$) efficiencies. The individual efficiencies depend on specific phenomena along the excitation path of Eu^{+3} ions. The experimental pathway on how to alter these phenomena, in favor of the respective efficiency, are also shown in figure 2.16.

The utilization of advanced growth techniques such as metalorganic chemical vapor deposition technique (OMVPE) can result in high crystal quality [44-47]. By carefully adjusting the growth parameters, the defect concentration in the GaN host can be minimized resulting in lower SHR recombination constant A. In addition, the lower defect concentration will give rise to the carrier mobility along the structure due to reduction of the scattering centers. The carrier mobility affects the transport time, which plays an essential role in the electrically-driven internal quantum efficiency (η_{IQE}) of the system. The direct effect of carrier mobility was not presented here, but it is evident through the ambipolar diffusion transport time [29,29,31,41]. For higher carrier mobility in the GaN region, the current injection efficiency ($\eta_{\mathrm{injection}}$) will be enhanced in the RE-doped LEDs. In contrast, the higher carrier mobility in the GaN:Eu region will result in lower current injection efficiency ($\eta_{\mathrm{injection}}$) and lower excited Eu^{+3} ion concentration in the active region. Both the carrier mobility and length of the device active regions affect the transport time. Furthermore, the utilization of heterostructure will be beneficial for the internal quantum efficiency (η_{IQE}), attributed to the stronger carrier localization which in turn increases the trap capture probabilities [18,42,43]. In order to obtain a more efficient excitation of Eu^{+3} ion, co-doping and strain engineering in the GaN host are possible pathways. These meth-

ods have been proved to result in more efficient capture process and energy transfer process to the Eu^{+3} ion [15,20,21,22,26,27,48].

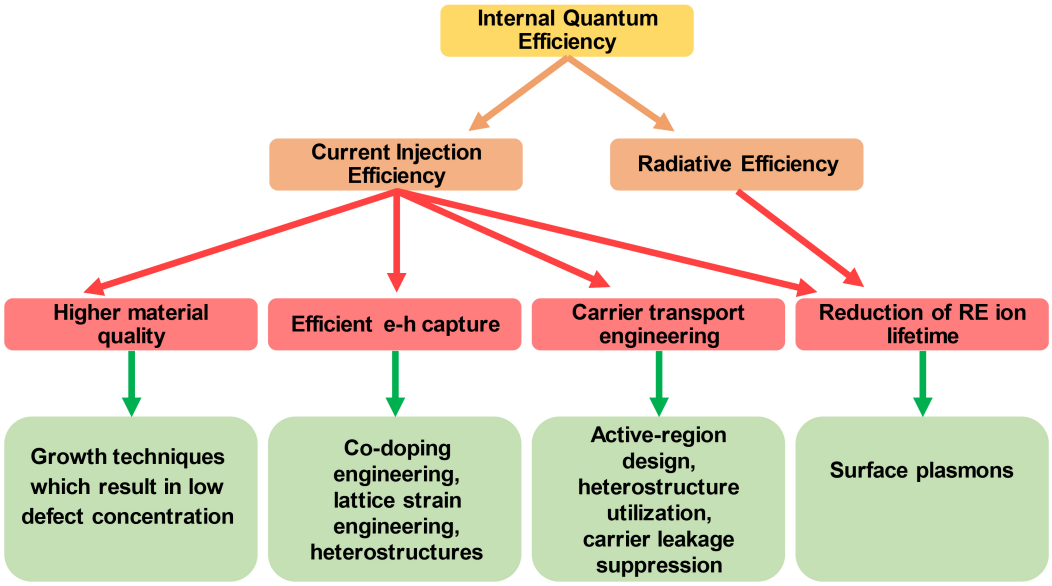

Figure 2.16: Internal quantum efficiency in the GaN:Eu based devices and its dependency on the parameters along the excitation path of Eu^{+3} ion.

The effect of radiative lifetime of Eu^{+3} ions is crucial for the internal quantum efficiency (η_{IQE}) of the device. From the present analysis, the current injection efficiency ($\eta_{\mathrm{injection}}$) and consequently the internal quantum efficiency (η_{IQE}) are limited by the saturation of the excited Eu^{+3} ion concentration at higher input current densities. In order to achieve higher efficiencies at higher input current densities, the change of this saturation rate is essential. It has been experimentally demonstrated that by utilizing surface-plasmon (SP) in GaN based QW can significantly increase the radiative efficiency of the system (49-52). For the case of GaN:Eu based emitters, through the engineering of the deposited materials used as SPs, the SP frequency can be adjusted to be very closed to the frequency of the emitted photons from the Eu^{+3} ions. This approach will increase both the current injection efficiency ($\eta_{\mathrm{injection}}$) and also the radiative efficiency (η_{rad}) of the system. The effect of the SPs on the IQE of the GaN:Eu emitters is presented in the next chapter.

2.7 A note to the relative magnitude of the lifetimes across the Eu^{+3} excitation path

It is necessary to clarify that, as described in section 2.3.5, the values of the different lifetimes associated with the trap/bound-exciton and Eu^{+3} ions were mainly based on the studies presented in the recent experimental works available in the literature [references 39 and 40]. However, it is important to mention that the range of the values of these lifetimes can significantly vary between GaN:Eu samples fabricated under different synthesis methods and conditions. In addition, as the GaN:Eu material quality is improved over the years and a better understanding of the excitation of the Eu^{+3} ions in the GaN host is established, the magnitude of the relative lifetimes associated with the trap-assisted excitation path of the Eu^{+3} ions might be proven to be lower than the values that have been used in this thesis. Nevertheless, the key idea and message obtained from the models presented in this thesis would not be altered.

2.8 Summary of Chapter 2

In summary, a current injection efficiency model (CIE) for optically-pumped and electrically -driven GaN:Eu based device with different active region configurations was developed. Through this model, the limiting factors of an optically-pumped GaN:Eu based QW device as well as and electrically-driven GaN:Eu based QW and GaN/GaN:Eu/GaN device is identified. In addition, the discrepancy between the efficiencies of optically-pumped and electrically-driven GaN:Eu QW is explained in the framework of the current injection efficiency models.

The analysis of the internal quantum efficiency (η_{IQE}) is accomplished in the basis of a multilevel system, which includes the carrier behavior and mechanisms in the

different regions of the active region and the interactions of the traps, carriers and Eu^{+3} ions with the GaN host. It was found that the droop in the efficiency of the GaN:Eu devices is associated with the droop in the current injection efficiency ($\eta_{\text{injection}}$) of the active region which arises from the saturation of the excited Eu^{+3} ion concentration. Through the manipulation of the characteristic rates and processes associated with the excitation path of Eu^{+3} ions, efficiencies higher than the current state of the art can be achieved.

These findings are applied both to optically-pumped and electrically-driven GaN:Eu based devices. Figure 2.16 provides the key points required for higher efficiency in the GaN:Eu based devices. Note that potential improvements in the extraction efficiency of the devices could further improve the EQE, but since they are not within the scope of this work, they are not taken into consideration here. In addition, according to the CIE model, several experimental pathways on how to increase the internal quantum efficiency (η_{IQE}) of the GaN:Eu based devices, including strategies for suppressing droop were presented.

This work demonstrates the pathway for enhancing the efficiency of the GaN:Eu based red light emitting devices. In addition, the CIE model can be extended to other RE-doped wide band-gap semiconductors, in which the excitation of RE ion is trap assisted.

References

1. Favennec, P. N., L'Haridon, H., Salvi, M., Moutonnet, D., and Le Guillou, Y., Luminescence of erbium implanted in various semiconductors: IV, III-V and II-VI materials. Electron. Lett., 25, 718–719 (1989).

2. Kenyon, A. J., Recent developments in rare-earth doped materials for optoelectronics. Progress in Quantum Elect., 26, 225–284 (2002).

3. Hömmerich, U., et al. Photoluminescence studies of rare earth (Er, Eu, Tm) in situ doped GaN. Mat. Sc. Eng. B, 105, 91–96 (2003).

4. Lozykowski, H. J., Jadwisienczak, W. M., Han, J., and Brown, I. G., Luminescence properties of GaN and Al0.14Ga0.86N/GaN superlattice doped with europium. Appl. Phys. Lett., 77, 767 (2000).

5. Sawahata, J., Bang, H., Seo, J., and Akimoto, K., Optical processes of red emission from Eu doped GaN. Sc. Tech. Adv. Mat., 6, 644–648 (2005).

6. Wakamatsu, R., et al. Luminescence Properties of Eu-Doped GaN Grown on GaN Substrate. Jap. J. Appl. Phys., 52, 08JM03 (2013).

7. M. de Boer, W. D. A., et al. Optical excitation and external photoluminescence quantum efficiency of Eu3+ in GaN. Sci. Rep., 4, 5235 (2014).

8. Wakamatsu, R., Timmerman, D., Lee, D., Koizumi, A., and Fujiwara, Y., Afterglow of Eu related emission in Eu-doped gallium nitride grown by organometallic vapor phase epitaxy. J. Appl. Phys., 116, 043515 (2014).

9. Heikenfeld, J., Garter, M., Lee, D. S., Birkhahn, R., and Steckl, A. J., Red light emission by photoluminescence and electroluminescence from Eu-doped GaN. Appl. Phys. Lett., 75, 1189 (1999).

10. Kim, J. H., and Holloway, P. H., Room-temperature photoluminescence and electroluminescence properties of sputter grown gallium nitride doped with europium. J. Appl. Phys., 95, 4787 (2004).

11. Park, J. H., and Steckl, A. J., Laser action in Eu-doped GaN thin-film cavity at room temperature. Appl. Phys. Lett., 85, 4588 (2004).

12. Nishikawa, A., Kawasaki, T., Furukawa, N., Terai, Y., and Fujiwara, Y., Room-temperature red emission from a p-type/europium-doped/n-type gallium nitride light-emitting diode under current injection. Appl. Phys. Express., 2, 071004 (2009).

13. Nishikawa, A., Kawasaki, T., Furukawa, N., Terai, Y., and Fujiwara, Y., Electroluminescence properties of Eu-doped GaN-based red light-emitting diode by OMVPE. Phys. Stat. Sol. A, 207, 1397–1399 (2010).

14. Nishikawa, A., Furukawa, N., Kawasaki, T., Terai, Y., and Fujiwara, Y., Improved luminescence properties of Eu-doped GaN light-emitting diodes grown by atmospheric-pressure organometallic vapor phase epitaxy. Appl. Phys. Lett., 97, 051113 (2010).

15. Nishikawa, A., Furukawa, N., Kawasaki, T., Terai, Y., and Fujiwara, Y., Room-temperature red emission from light-emitting diodes with Eu-doped GaN grown by organometallic vapor phase epitaxy. Optical Mat., 33, 1071–1074 (2011).

16. Sekiguchi, H., et al. Red light-emitting diodes with site-selective Eu-doped GaN active layer. Jap. J. Appl. Phys., 52, 08JH01 (2013).

17. Ishii, M., Koizumi, A., and Fujiwara, Y., Nanoscale determinant to brighten up GaN:Eu red light-emitting diode: Local potential of Eu-defect complexes. J. App. Phys., 117, 155307 (2015).

18. Arai, T. et al. Enhanced excitation efficiency of Eu ions in Eu-doped GaN/AlGaN multiple quantum well structures grown by organometallic vapor phase epitaxy. J. Luminescence, 158, 70–74 (2015).

19. Inaba, T. et al. Substantial enhancement of red emission intensity by embedding Eu-doped GaN into a microcavity. AIP Adv., 6, 045105 (2016).

20. Zhu, W. et al. High-power Eu-doped GaN red LED based on a multilayer structure grown at lower temperatures by organometallic vapor phase epitaxy. MRS Adv., 67, 159-164 (2017).

21. Inaba, T., Mitchell, B., Koizumi, A. & Fujiwara, Y. Emission enhancement and its mechanism of Eu-doped GaN by strain engineering. Optical Mat. Express, 7, 1381-1387 (2017).

22. Fujiwara, Y., and Dierolf, V., Present understanding of Eu luminescent centers in Eu-doped GaN grown by organometallic vapor phase epitaxy. Jap. J. Appl. Phys., 53, 05FA13 (2014).

23. Ohkawa, K., Watanabe, T., Sakamoto, M., Hirako, A. & Deura, M. 740-nm emission from InGaN-based LEDs on c-plane sapphire substrates by MOVPE. J. Cryst. Growth, 343, 13 (2012).

24. Hwang, J., Hashimoto, R., Saito, S. & Nunoue, S. Development of InGaN-based red LED grown on (0001) polar surface. Appl. Phys. Express, 7, 071003 (2014).

25. Woodward, N., et al. Excitation of Eu3+ in gallium nitride epitaxial layers: Majority versus trap defect center. Appl. Phys. Lett., 98, 011102 (2011).

26. Mitchell, B. et al. The role of donor-acceptor pairs in the excitation of Eu-ions in GaN:Eu epitaxial layers. J. Appl. Phys., 115, 204501 (2014).

27. Masago, A., Fukushima, T., Sato, K. & Katayama-Yoshida, H. Efficient luminescent center by codoping (Eu,Mg,O) into GaN. Appl. Phys. Express., 7, 071005 (2014).

28. Tansu, N., and Mawst, L. J., Current injection efficiency of 1300-nm InGaAsN quantum-well lasers. J. Appl. Phys., 97, 054502 (2005).

29. Nagarajan, R., Ishikawa, M., Fukushima, T., Geels, R. S., and Bowers, J. E., High speed quantum-well lasers and carrier transport effects. IEEE J. Quantum. Electron., 28, 1990-2008 (1992).

30. Xu, L. F., et al., Experimental evidence of the impact of nitrogen on carrier capture and escape times in InGaAsN / GaAs single quantum well. IEEE Photonics J., 4, 2262-2271 (2012).

31. Zhao, H. P., Liu, G. Y., Zhang, J., Arif, R. A., and Tansu, N., Analysis of internal quantum efficiency and current injection efficiency in nitride light-emitting diodes. J. Disp. Technol., 9, 212-225 (2013).

32. Schneider, H., and v. Klitzing, K., Thermionic emission and gaussian transport of holes in a $GaAs/Al_xGa_{1-x}As$ multiple-quantum-well structure. Phys. Rev. B, 38, 6160 (1988).

33. Taylor, G. W., and Jin, S., Revisions to Transport solution for SCH QW laser diodes. IEEE J. Quantum. Electron., 34, 1886-1889 (1998).

34. Tansu, N., and Mawst, L. J., The Role of Hole-Leakage in 1300-nm InGaAsN Quantum Well Lasers. Appl. Phys. Lett., 82, 1500-1502, (2003).

35. Gardner, N. F., et al. Blue-emitting InGaN–GaN double-heterostructure light-emitting diodes reaching maximum quantum efficiency above 200A/cm2. Appl. Phys. Lett., 91, 243506 (2007).

36. Shen, Y. C., et al. Auger recombination in InGaN measured by photoluminescence. Appl. Phys. Lett., 91, 141101 (2007).

37. Kim, M., et al. Origin of efficiency droop in GaN-based light-emitting diodes. Appl. Phys. Lett., 91, 183507 (2007).

38. Xie, J., et al. On the efficiency droop in InGaN multiple quantum well blue light emitting diodes and its reduction with p doped quantum well barriers. Appl. Phys. Lett., 93, 121107 (2008).

39. Lee, C. W., Everitt, H. O., Lee, D. S., Steckl, A. J., and Zavada, J. M., Temperature dependence of energy transfer mechanisms in Eu-doped GaN. J. Appl. Phys., 95, 7717 (2004).

40. Wang, J., Koizumi, A., Fujiwara, Y., and Jadwisienczak, W. M., Study of defects in GaN in situ doped with Eu3+ ion grown by OMVPE. J. Elect. Mat., 45, 2001-2007 (2016).

41. Yeh, J. Y., Mawst, L. J. & Tansu, N. The Role of Carrier Transport on the Current Injection Efficiency of InGaAsN Quantum-Well Lasers. IEEE Photon. Technol. Lett., 17, 1779-1881 (2005).

42. Al Tahtamouni, T. M., Stachowicz, M., Li, J., Lin, J. Y. & Jiang, H. Dramatic enhancement of 1.54 μm emission in Er doped GaN quantum well structures. Appl. Phys. Lett., 106, 121106 (2015).

43. Al Tahtamouni, T. M., Li, J., Lin, Y. J. & Jiang, H. J. Current injection 1.54 μm light-emitting devices based on Er-doped GaN/AlGaN multiple quantum wells. Opt. Mat. Exp., 6, 3476-3481 (2016).

44. Amano, H., Sawaki, N., Akasaki, I. & Toyoda, Y., Metalorganic vapor phase epitaxial growth of a high quality GaN film using an AlN buffer layer. Appl. Phys. Lett., 48, 353 (1986).

45. Hashimoto, T., Wu, F., Speck, J. S. & Nakamura, S. A GaN bulk crystal with improved structural quality grown by the ammonothermal method. Nature Mater., 6, 568 (2007).

46. Nakamura, S. In Situ Monitoring of GaN growth using interference effects. Jap. J. Appl. Phys., 30, 10A (1991).

47. Ee, Y. K. et al. Metalorganic vapor phase epitaxy of III-nitride light-emitting diodes on nano-patterned AGOG sapphire substrate by abbreviated growth mode. IEEE J. Sel. Top. Quantum Electron., 15, 1066-1072 (2009).

48. Zavada, J. M. Impurity co-doping of gallium nitride materials for enhanced light emission. ECS Trans., 61, 65-70 (2014).

49. Okamoto, K. et al. Surface plasmon-enhanced light emitters based on InGaN quantum wells. Nature Mater., 3, 601-605 (2004).

50. Okamoto, K. et al., Surface plasmon enhanced spontaneous emission rate of InGaN/GaN quantum wells probed by time-resolved photoluminescence spectroscopy. Appl. Phys. Lett., 87, 071102 (2005).

51. Neogi, A. et al. Enhancement of spontaneous emission in a quantum well by resonant surface plasmon coupling. Phys. Rev. B, 66, 153305 (2002).

52. Zhao, H. P., Zhang, J., Liu, G. Y. & Tansu, N. Surface plasmon dispersion engineering via double-metallic Au / Ag layers for III-nitride based light-emitting diodes. Appl. Phys. Lett., 98, 151115 (2011).

53. Schubert, M. F. et al. Effect of dislocation density on efficiency droop in GaInN/GaN lightemitting diodes. Appl. Phys. Lett., vol. 91, p. 231114, 2007.

54. Shen, Y. C. et al. Auger recombination in InGaN measured by photoluminescence. Appl. Phys. Lett., vol. 91, p. 141101, Oct. 2007.

Chapter 3

Surface plasmon polaritons for IQE enhancement

3.1 Theory of surface plasmon polaritons

Plasmons are the quanta of the collective oscillations of the "free" electrons in a material at the presence of an electromagnetic field. The term "free" usually denotes the electrons present in the conduction band of the (semi-) conductive material. Surface plasmons are a special case, where collective plasma oscillations take place at the interface of negative dielectric constant -(semi-) conductive material- and a positive dielectric constant material. Surface plasmons oscillate at frequency (ω_{sp}), which is lower than the oscillation frequency of the bulk plasmons (ω_p). When coupling of an electromagnetic wave and a surface plasmon occurs, a quasi-particle named surface-plasmon-polariton is formed, which propagates along the (semi-)conductor/dielectric interface (figure 3.1). A detailed theory regarding the formation of surface plasmon polaritons in metal-dielectric interfaces can be found in references [1-5]. In the following section a brief description of the surface plasmon polariton in an infinite metal-dielectric interface and in a multiple dielectric/metal/dielectric system will be

given.

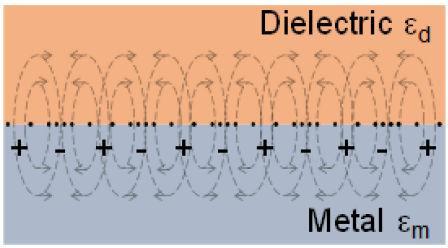

Figure 3.1: Surface plasmon polaritons at the metal / dielectric interface.

3.1.1 Case of semi-infinite layers

To describe the surface plasmon polaritons mathematically, we need to solve the Maxwell's equations by imposing appropriate boundary conditions in the metal / dielectric system. Assuming the structure depicted in figure 3.2, a dielectric material ε_d , occupies half space ($z > 0$) while a conductive material with a relative dielectric function ε_m occupies the other half space ($z < 0$).

Figure 3.2: Schematic diagram of a semi-infinite metal/dielectric structure. The dielectric has a positive relative dielectric function ε_d >0 and the metal has a complex relative dielectric function with $Re(\varepsilon_m)$<0.

Considering an electromagnetic wave propagating in the $\hat{x}$ direction as $\vec{E}(x, y, z) = \vec{E}(x)e^{-i\gamma x}$ the wave equation take form of

$$\frac{\partial^2 \vec{E}(x,y,z)}{\partial z^2} + \left({k_0}^2 - \gamma^2\right)\vec{E}\,(x,y,z) = 0 \tag{3.1}$$

where, the k_0 is the propagation constant in the free space ($k_0 = \omega/c$) and γ is the propagation wavevector along the $\hat{x}$ direction. Assuming harmonic time dependence

and homogeneity along the $\hat{y}$ direction the following set of equations for TM solutions (which are confined at the interface) are derived:

$$\begin{aligned} H_y(z) &= A_d e^{-i\gamma x} e^{-k_d z} \ , z > 0 \\ H_y(z) &= A_m e^{-i\gamma x} e^{k_m z} \ , z < 0 \end{aligned} \tag{3.2}$$

where the k_d and k_m are the wavevectors perpendicular to the interface of the two materials. The continuity of the electromagnetic field at the interface requires that $A_m = A_d$ and

$$\frac{k_d}{k_m} = -\frac{\varepsilon_d}{\varepsilon_m} \tag{3.3}$$

In order to have confinement of the wave at the interface the above equation requires that $Re(\varepsilon_m)<0$ and $\varepsilon_d>0$, i.e the metal and the dielectric need to have opposite sings of the real part of their relative dielectric functions (for the case of complex values of the dielectric). According to the definition of equation (3.1) the following relations are obtained:

$$k_d^2 = \gamma^2 - k_0^2 \varepsilon_d \tag{3.4}$$

$$k_m^2 = \gamma^2 - k_0^2 \varepsilon_m \tag{3.5}$$

and combining the equations (3.3)-(3.5) yields to the dispersion relation of SPPs propagating at the interface between two semi-infinite spaces:

$$\gamma = k_0 \sqrt{\frac{\varepsilon_d \varepsilon_m}{\varepsilon_d + \varepsilon_m}} \tag{3.6}$$

For the case of TE modes, the continuity at of the electromagnetic wave at the interface requires $A_m(k_m+k_d) = 0$ and since confinement in the interface requires

positive real values of the complex k_d and k_m , the above condition is fulfilled only for the case where A_m=0 and therefore $A_m = 0 = A_m$. Thus, no surface modes exist for TE polarization for this structure.

Note: The definition of a complex relative dielectric function is $\varepsilon_r = \varepsilon_r'$ - $i\varepsilon_r''$ where ε_r' <0 and ε_r'' <0. In addition, in the set of equations (3.2) the propagation constant equals to $\gamma = \alpha$ - $i\beta$, where α >0 and β >0 (In the section 3.2 of this chapter, the γ is presented as k_{spp}). In this definition, α is the real propagation constant and the β is the attenuation constant. The last one defines the effective propagation distance ($1/e$ decay length) of the surface plasmon polariton $L_{spp} = \beta^{-1}$ (or $(2\beta)^{-1}$ if it refers to Power).

Figure 3.3 shows the dispersion relation of a semi-infinite strucure of Au/air. For these calculations the dielectric function of the air is $\varepsilon_{rair} = 1$ and that of gold is described by the Drude model as:

$$\varepsilon_{rAu} = \varepsilon_\infty - \frac{{\omega_p}^2}{\omega^2 - i\omega\Gamma_p} \tag{3.7}$$

where the $\varepsilon_\infty = 6.21$ is the background constant permittivity at high frequency, the ω_p =1.33×10^{16} rad/s is the plasma frequency of the gold and the $\Gamma_p = 1.32 \times 10^{14}$ rad/s is the damping factor.

The dashed line is the light line in the air while the the blue and orange represents the dispersion without and with a damping factor Γ_p respectively. In general, it is important to mention that the SPP resonance frequency is the frequency at which the condition $Real\{\varepsilon_{rAu}\} = Real\{\varepsilon_{rair}\}$ is satisfied, and defines an asymptotic limit for the SPP dispersion. The dispersion relation for both cases exhibits two branches, a high-energy and a low-energy branch. The high-energy branch, called the Brewster mode, does not describe true surface waves, since according to the equations (3.5) and (3.2) the z-component of the wavevector in the metal is imaginary and hence the fields propagate inside the metal. The low-energy branch corresponds to the real in-

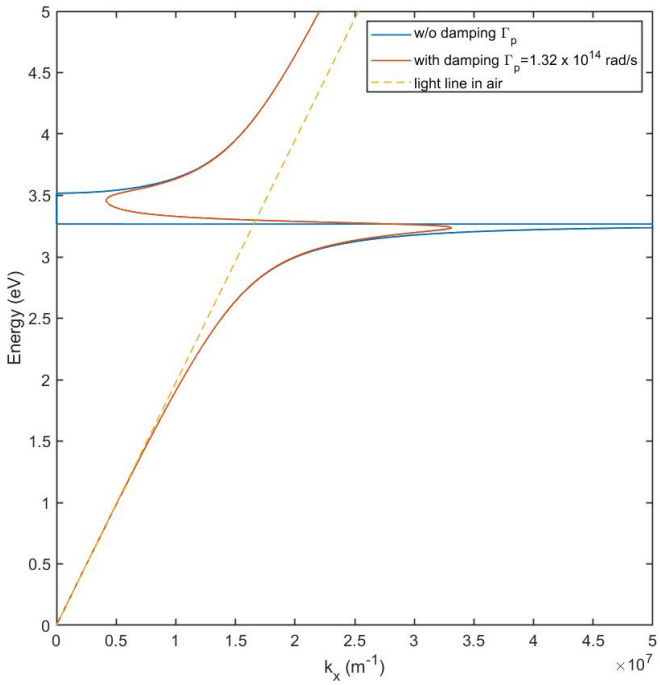

Figure 3.3: Dispersion relation of a semi-infinite strucure of Au/air.

terface wave, i.e the surface plasmon polariton, and it approaches the asymptotic limit corresponding to the ω_{sp}. For the case with a damping factor there is a continuous transition from the lower-energy branch (SPP dispersion) to the upper higher-energy branch. This is because, as the SPP dispersion line approaches the asymptotic limit ω_{sp}, the losses inside the metal increase significantly. As a result, for energies higher than ω_{sp} the dispersion curve bends back and connects to the upper higher-energy branch. In the connecting region the energy of the mode is strongly localized inside the metal, and hence the high losses are present. In contrast, for the ideal case without damping, the two branches are not connected (the connection is due to the numerical simulation in Matlab) which means that the fields do not propagate inside the metal and no losses take place. For this study, the upper high-energy branch is not considered.

An important feature of surface plasmons is that for a given energy the wavevector

k_x is always larger than the wavevector of light in free space (dashed line). It is seen that for small wavevectors k_x the SPP dispersion curve asymptotically approaches the light line in air (or any other dielectric in case of Au/dielectric interface). The physical reason for the increased k_x (and hence momentum) of the SPP is the strong coupling between the light and the surface charges. The light field has to "attract" the electrons along the metal surface. This means that in order for the SPP to be excited, phase matching condition must exist (photon must have similar wavevector to k_x). The same also is true for the decoupling of the SPP into radiation modes in the air (or dielectric). This will be described in the later section.

3.1.2 Case of a planar multilayer structure

For the case of a multilayer structure the transfer matrix method is utilized to solve for the surface plasmon dispersion relation. The schematics of such structure are shown in figure 3.4.

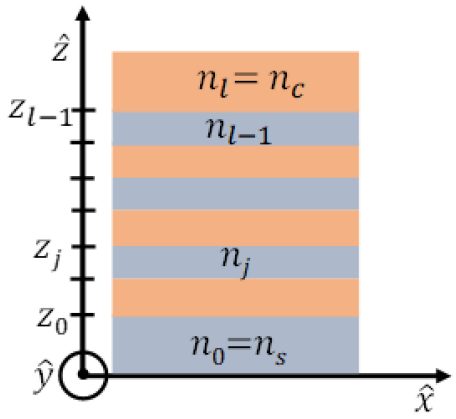

Figure 3.4: Schematic diagram of a multilayer structure.

The equation of TM modes propagating along the $\hat{x}$ direction is given by

$$\vec{H}_j = H_j(z)e^{i(\omega t - \gamma x)}\ \hat{y} \tag{3.8}$$

$$\vec{E}_j = \left(\frac{\gamma}{\omega \varepsilon_0 \varepsilon_{r_j}} H_j(z) \;\; \hat{z} - \frac{j}{\omega \varepsilon_0 \varepsilon_{r_j}} \frac{\partial H_j(z)}{\partial z} \hat{x} \right) e^{i(\omega t - \gamma x)} \tag{3.9}$$

where the propagation constant γ is defined in an equivalent manner to the section 3.1.1. and the index j refers to the particular j^{th} layer. The magnetic field amplitude $H_{j(z)}$ in the j^{th} layer is defined as

$$H_j(z) = A_j e^{-i \; k_j (z_j - z_{j-1})} + B_j e^{-i \; k_j (z_j - z_{j-1})} \tag{3.10}$$

where the A_j and B_j are the coefficients corresponding to the $\hat{z}$ and $-\hat{z}$ propagation directions respectively. In addition, z_j defines the boundary between the j^{th} and $(j+1)^{th}$ layer and k_j is the wavevector normal to the interface, defined as

$$k_j = \sqrt{\gamma^2 - \frac{\omega^2}{c^2} \varepsilon_{r_j}} \tag{3.11}$$

where the c is the speed of the light in vacuum and ε_{r_j} is the complex relative dielectric function of the j^{th} layer. (Note that the ε_r of a material is given is related to the complex refractive index via $\varepsilon_r = n^2$).

By applying boundary conditions requiring the continuity of the fields at the interface of the j^{th} and $(j+1)^{th}$ layer (i.e at $z = z_j$) and requiring their equality at z_j-z_{j-1} the following matrix regarding the amplitudes of the j^{th} and $(j+1)^{th}$ layer is derived:

$$\begin{bmatrix} A_{j+1} \\ B_{j+1} \end{bmatrix} = Q_j \begin{bmatrix} A_j \\ B_j \end{bmatrix} \tag{3.12}$$

where Q_j is the transfer matrix is defined as

$$Q_j = \frac{1}{2} \begin{bmatrix} \left(1 + \left(\frac{n_{j+1}^2}{n_j^2}\right) \frac{k_j}{k_{j+1}}\right) e^{-k_j d_j} & \left(1 - \left(\frac{n_{j+1}^2}{n_j^2}\right) \frac{k_j}{k_{j+1}}\right) e^{k_j d_j} \\ \left(1 - \left(\frac{n_{j+1}^2}{n_j^2}\right) \frac{k_j}{k_{j+1}}\right) e^{-k_j d_j} & \left(1 + \left(\frac{n_{j+1}^2}{n_i^2}\right) \frac{k_j}{k_{j+1}}\right) e^{k_j d_j} \end{bmatrix} \tag{3.13}$$

where $d_j = z_{j+1}$-z_j is the thickness of the j^{th} layer.

For a multilayer structure having l layers the transfer matrix for the whole structure equals to the product of

$$Q_{tot} = \prod_{j=l-1}^{0} Q_j = \begin{bmatrix} q_{11} & q_{12} \\ q_{21} & q_{22} \end{bmatrix} \tag{3.14}$$

and corelates the complex coefficients of the cover and substrate layer

$$\begin{bmatrix} A_c \\ B_c \end{bmatrix} = Q_{tot} \begin{bmatrix} A_s \\ B_s \end{bmatrix} \tag{3.15}$$

For confined modes whose fields must vanish in the infinity ($-\infty$, $+\infty$) the coefficients A_s and B_c must equal to 0. Therefore, by substituting in the above equation we get:

$$q_{22}(\gamma, \omega) = 0 \tag{3.16}$$

The values of the complex propagation wavevector γ that satisfy the above equation give both the guided and leaky modes of the structure and determine the dispersion relation of the surface plasmon polariton $\hbar\omega$ vs $Re(\gamma)$, where the $\hbar$ is the Plank's constant. The equation (3.15) is solved numerically in Matlab while the electromagnetic field profile is evaluated though equations (3.11)-(3.14). Note that the complex coefficients A_j and B_j are unnormalized. The normalization condition requires that the field carries 1 watt of power flow along the $\hat{x}$ axis per unit width in the $\hat{y}$ direction:

$$\int_{-\infty}^{\infty} \frac{|H_j(z)|^2}{{\varepsilon_{r_j}}^*} dz = \frac{2\omega\varepsilon_0}{\gamma^*} \tag{3.17}$$

3.2 Purcell factor F_p due to SPP coupling

The spontaneous emission rate of an emitter in a dielectric medium of refractive index of n is given by the well know formula of (derived from the Fermi's golden rule)

$$\Gamma_0 = n\frac{{\omega_p}^3\mu^2}{3\pi^2\hbar\varepsilon_0 c^3} \tag{3.18}$$

where n is the refractive index of the dielectric where the emitter is embedded, ω is the transition frequency of the emitter and μ is the dipole matrix element of the transition.

If the system of the emitter is in the vicinity of a conductive layer such as metal, the spontaneous emission rate will be modified due to the coupling to the SPP modes (assuming that the frequency of the emitter is very close to the SPP frequency ω_{sp}). The total recombination rate of the emitter will be the sum of $\Gamma_0 + \Gamma_p + \Gamma_{nr}$, with Γ_{nr} the non radiative recombination of the emitter and Γ_p the recombination rate into the plasmon modes.

This total new recombination rate with respect tot he recombination rate of the emitter without the presence of the metal, is an analog of the Purcell factor F_p and can be expressed as :

$$F_p = \frac{\Gamma_p(\omega) + \Gamma_0(\omega) + \Gamma_{nr}(\omega)}{\Gamma_0(\omega) + \Gamma_{nr}(\omega)} \approx 1 + \frac{\Gamma_p(\omega)}{\Gamma_0(\omega)} \tag{3.19}$$

assuming minimal non-radiative recombination rate of the emitter compared to its radiative recombination rate.

The local electric filed of the plasmon mode $E(a)$, where a is the distance of the emitter relative to the conductive layer, can be used to estimate the corresponding recombination rate (Γ_p) of the emitter into the plasmon continuum. This recombination rate of the emitter is given by the Fermi's golden rule:

$$\Gamma_p = \frac{2\pi}{\hbar}\left\langle \vec{\mu}\vec{E}(a)\right\rangle^2 \rho(\hbar\omega) \tag{3.20}$$

where $\rho(\hbar\omega)$ is the mode density of plasmons and is equal to

$$\rho(\hbar\omega) = \frac{L^2}{4\pi}\frac{d(k^2)}{d(\hbar\omega)} \tag{3.21}$$

It can be seen that the surface plasmon density of states can be calculated from the dispersion relation ω vs k.

The electric field $E(a)$ can be normalized to a half quantum for zero-point fluctuation by the following relation:

$$E^2(a) = \frac{\hbar\omega/2}{\frac{L^2}{4\pi}\int_{-\infty}^{\infty} d(\omega\varepsilon)/d(\omega)E_0^2(z)dz}E_0^2(a) \tag{3.22}$$

where $E_0(z)$ is the unnormalized plasmon electric field and L^2 is the in-plane quantization area and ε the dielectric fucntion of materials that conist the system emitter/dielectric and conductive layer (ε_r is the relative dielectric function). Combining the above equations the Purcell factor of the emitter/dielectric in the presence of the conductive layer is given by:

$$F_p(\omega) = 1 + \frac{3\pi c^3 E_0^2(a)}{4n\omega^2\int_{-\infty}^{\infty} d(\omega\varepsilon_r)/d(\omega)E_0^2(z)dz}\frac{d(k^2)}{d(\omega)} \tag{3.23}$$

3.3 Coupling of SP on GaN based emitters for visible emission

The field related to surface plasmon polariton and their properties is named plasmonics. Due to their novel optical properties, SPPs have been used in a variety of applications, such as sensing spectroscopy and subwavelength optics [6-9]. In ad-

dition, their usage in enhancing the efficiency of light emitting devices has already been established. The first researchers that theoretically proposed the use of plasmonics for the emission enhancement of materials were Yablonovitch et al [10,11]. Okamoto et all were the first to demonstrate the light emission enhancement for an InGaN/GaN quantum well (QW) material coated with Ag thin film [12]. The reason for the efficiency enhancement is due to the coupling of the emitted electromagnetic (EM) mode to a surface plasmon (SP) of a conductive layer, spaced at a distance from the emitter, and the generation of a surface plasmon polariton (SPP). Through this coupling, the radiative efficiency of the system is enhanced (the effective radiative lifetime is reduced) due to increase of photon density states near the surface plasmon energy E_{sp} - a phenomenon known as the Purcell effect [13]. Since the first work of Okamoto et al., the concept of SP coupling to the active materials in III-Nitride semiconductors has been widely used. More specifically, metallic thin layers such as silver (Ag) and gold (Au) have been deposited on top of InGaN multiple quantum wells for increasing the efficiency of the emitter in the ultraviolet (UV) and visible spectral regimes [10-12,14-17].

However, despite the popularity of these noble metals as the metallic plasmonic material choices for applications in the UV and visible spectral regime, such materials are unsuitable for plasmonic applications in the red and near infrared spectral regime attributed to high Ohmic losses [18, 19]. In contrast, the transition-metal nitrides, such as titanium nitride (TiN), hafnium nitride and zirconium nitride (ZrN), are promising candidates as low-loss plasmonic materials in the visible and near-IR spectral regimes attributed to the ability for achieving negative real permittivity values at relatively lower carrier concentrations [20-25]. In addition, these materials offer a wide tunability of their dielectric properties, usually through the variation of the deposition parameters [20-25]. The concept of the efficiency enhancement via the surface plasmon polaritons can be applied for the case of the GaN:Eu emitters.

Through the CIE models and the analysis presented in the previous chapter, it was identified that the saturation of the excited Eu^{+3} ions in the GaN host - resulted either by optical excitation or electrical injection in the GaN host - as one of the key factors limiting the peak internal quantum efficiency and droop issue at high injection current level. These limiting factors resulted in the low current injection efficiency in electrically-driven GaN:Eu LED, which in turn led to a significant reduction in both its internal and external quantum efficiencies.

In addition, it was proposed that the reduction in the radiative life time of Eu^{+3} ions (τ_{rad}) reduces the saturation issue of the Eu^{+3} ions up to higher current density; such approach enables the ability to achieve high current injection level and minimize the drooping issue at higher current density (for electrically-driven GaN:Eu devices) and at higher photon flux (for optically-excited devices). The reduction in the τ_{rad} also increases the radiative efficiency ($\eta_{\text{radiative}}$) of the Eu^{+3} ions, which in turn results in a further enhancement of the internal quantum efficiency ($\eta_{\text{IQE}} = \eta_{\text{injection}}\ \eta_{\text{radiative}}$) of the device.

In this chapter, the use of metal nitrides - TiN, HfN and ZrN - as plasmonic materials in the red spectral regime is investigated. More specifically, the effect of the coupling of the surface plasmons of the metal-nitride to the GaN:Eu based red light emitter and its impact on the internal quantum efficiency - of this particular type of red light emitter - is studied. A comparison among the metal nitrides is made, and it was found that TiN is the most suitable selection for applications in the characteristic photon energy of the GaN:Eu emitter at $\approx 2\ eV$. Consequently, the study is proceeded to investigate the effect of the TiN layer thickness (d_{TiN}) and GaN spacer thickness (d_{spr}) on the SPP dispersion relation and Purcell factor. The impact on the electrically-driven device characteristics for TiN-based surface plasmon coupled on GaN:Eu LEDs is also presented.

3.3.1 Effect of single layer of metal-nitride on the GaN:Eu emitter

For the purpose of the theoretical study, the structure depicted in figure 3.4 (a) is considered. The metal-nitride layer is placed on top of a GaN/GaN:Eu/GaN emitter, where the last layer of GaN serves as the spacer between the GaN:Eu and metal-nitride regions. The SPP dispersion relation is computed by solving the Maxwell's equations in the GaN/GaN:Eu/GaN active layer, metal-nitride plasmonic layer, and air region with the appropriate boundary conditions. After solving the SPP dispersion relation, the electric field profile is evaluated to calculate the Purcell enhancement factor; this method is similar to work presented in reference 10. The simulations are performed assuming the dielectric functions of GaN:Eu and GaN regions as identical and equal to is the refractive index of GaN. For the dielectric function of the metal-nitride the Drude-Lorentz model is used according to the following formula:

$$\varepsilon_{rTiN} = \varepsilon_{\infty} - \frac{{\omega_p}^2}{\omega^2 - i\omega\Gamma_p} + \sum_{j=1}^{m} \frac{f_j {\omega_j}^2}{{\omega_j}^2 - \omega^2 + i\omega\Gamma_j} \tag{3.24}$$

where the ε_{∞} is the background constant permittivity at high frequency, the ω_p is the plasma frequency of the metal-nitride, the Γ_p is the damping factor, and the ω_j is the frequency of the Lorentz oscillators with strength f_j and damping factor Γ_j. The parameters of the dielectric function of the individual metal-nitride materials investigated in this study are shown in Table 3.1.

Parameters	HfN	TiN	ZrN
ε_{∞}	2.5	4.855	3.465
ω_p (eV)	5.71	7.9308	8.018
Γ_j (eV)	0.6878	0.1795	0.5192
ω_1 (eV)	4.60	4.2196	5.48
f_1	1.20	3.2907	2.450
Γ_1 (eV)	2.65	2.0341	1.736

Table 3.1: Parameters of the Drude-Lorentz model for the different metal-nitrides investigated in this study.

Prior to the theoretical investigation it is important to mention that the structure studied here (figure 3.5 (a)) is basically the active region of a GaN:Eu based device. In addition, in this study any possible cavity effects on the Purcell enhancement factor have been excluded. The structure depicted in figure 3.5(a) does not contain any highly reflective layers (i.e reflective metals, distributed Bragg reflectors), as well as, does not meet the criteria for the lowest resonant cavity frequency: the required cavity width for the lowest resonant wavelength (or frequency) is $\lambda/2$ (where the λ is the characteristic emitted wavelength of the light source), while the total width of the structure depicted in figure 3.5(a) is much less than the above required condition.

Figure 3.5(b) depicts the effect of different metal-nitride materials on the SPP dispersion relation. The thickness of the metal-nitride layer was fixed at 20 nm while the thickness of the GaN spacer was fixed at 15 nm. It can be seen that the SPP dispersion relation approaches an asymptotic limit which corresponds to the characteristic surface plasmon polariton energy (E_{sp}). Among the metal-nitrides the energy of the SPP of the TiN is very close to the characteristic photon energy of the GaN:Eu emitter ($\approx 2\ eV$) in the red spectral regime. In contrast the ZrN and HfN present a characteristic E_{sp} which is in the green ($\approx 2.2\ eV$) and deep red ($\approx 1.70\ eV$) spectral regime respectively. In addition, as it is shown in figure 3.5(c), TiN presents high Purcell factor at the characteristic energy of E_{sp} as compared to the other metal-nitrides. It is important to mention that this comparison of metal-nitrides aims on the selection of the appropriate material for plasmonic application only in the spectral regime of the characteristic photon energy of GaN:Eu emitter at $\approx 2\ eV$. Therefore, TiN is found to be a suitable plasmonic material for the surface plasmon coupling with the GaN:Eu based red light emitter. The use of the other metal-nitrides presented in this study can be used for similar applications in the spectral regime of their characteristic asymptotic limit of E_{sp}.

Figure 3.6(a) depicts the effect of different TiN layer thickness on the SPP disper-

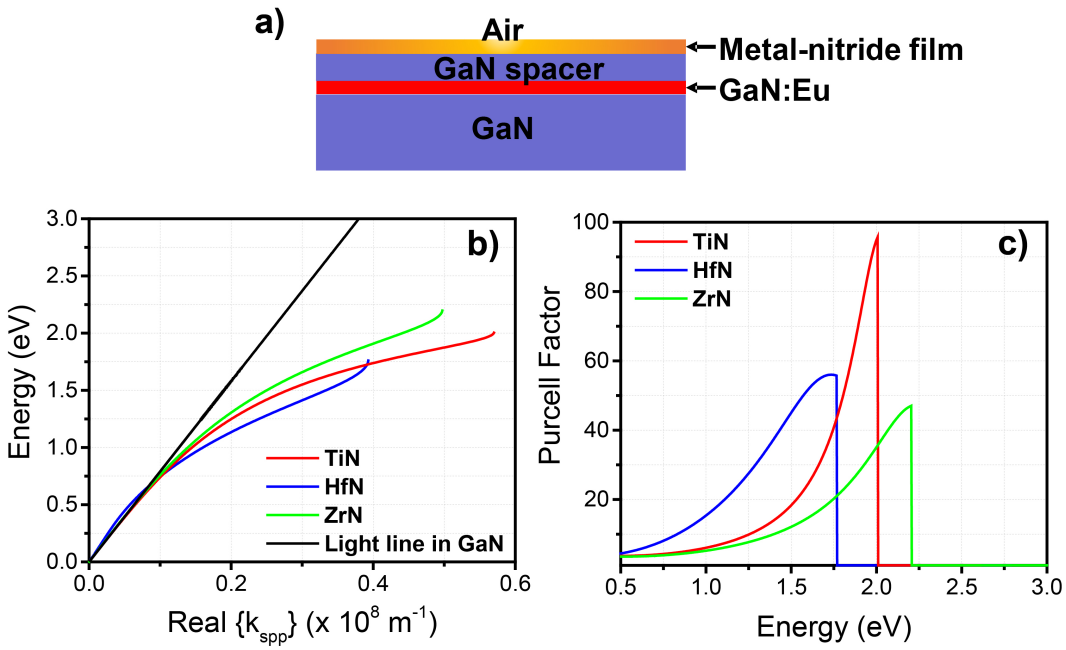

Figure 3.5: (a) Schematic of the structure used for the simulations. (b) Energy dispersion relation of the surface plasmon polariton (SPP) for different metal-nitrides. The thickness of the metal-nitride film was set at 20 nm while the GaN spacer thickness of was set at 15 nm. (c) Purcell factor for different metal-nitrides films on top of the GaN:Eu red light emitter

sion relation for the case of $d_{spr} = 15\ nm$. By decreasing the TiN thickness, the SPP curve is pushed down at lower energies while maintaining the asymptotic limit at E_{sp} $\approx 2.0\ eV$. In general, for a thin conductive layer surrounded by dielectrics, collective plasma oscillations localized at the metal/dielectric and metal/air interfaces exist. The thinner the conductive layer is, the stronger the coupling between the SPPs at the two interfaces becomes resulting in a larger energy separation of the two SPPs [15]. As the energy approaches the E_{sp} , the penetration depth of the electric field of the SPP in the conductive layer significantly reduces resulting in the non-interaction of the two SPPs at the two interfaces. Hence, the limit of E_{sp} is independent of the conductive layer thickness.

Figure 3.6(b) depicts the Purcell factor for various TiN thicknesses for the case of $d_{spr} = 15\ nm$. As the energy of the SPP increases towards E_{sp}, the Purcell factor

increases due to the increased surface plasmon density of states (SPDS). The maximum value of the Purcell factor is obtained at the limit of E_{sp}, where the SPDS has its maximum value. Note that the SPDS is proportional to $(\frac{\partial E}{\partial k})^{-1}$ of the dispersion curve shown in figure 3.6(a). At energies above E_{sp}, the GaN / TiN interface cannot support a guided SPP mode, hence the Purcell factor drops to unity. In addition, by decreasing the TiN thickness, the Purcell factor can be obtained for values higher than 100. In contrast, by reducing the TiN thickness beyond 10 nm, the Purcell factor drops at energy $\approx E_{sp}$, while it becomes broader at lower energies. This behavior is attributed to the lower energies of the SPP for the case of $d_{TiN} = 5\ nm$ as compared to those with $d_{TiN} > 5\ nm$, as shown in figure 3.6(a).

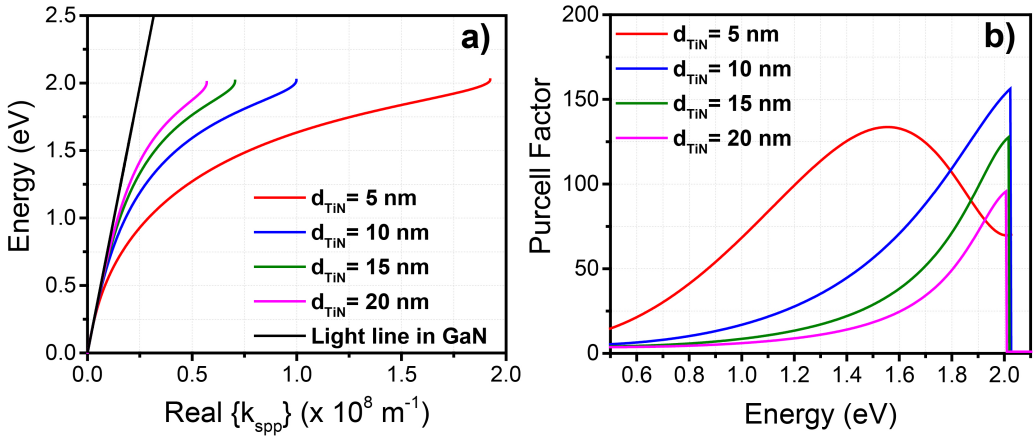

Figure 3.6: (a) Energy dispersion relation of the surface plasmon polariton (SPP) for different TiN thickness (d_{TiN}) with GaN spacer thickness of $d_{spr} = 15$ nm. (b) Purcell factor for different TiN thickness (d_{TiN}) with GaN spacer thickness of $d_{spr} = 15\ nm$.

As shown in figure 3.6(a) and 3.6(b), the use of thinner TiN layer results in larger SPP wavevector (k_{spp}) with high Purcell factor; however, such condition comes at the expense of the SPP propagation length $\lambda_{spp} = 2\pi/Re\{k_{spp}\}$ and the $1/e$ decay length of the electric field (L_{spp}). A length L_{spp} of ≈ 4.05 nm is obtained for the case of $d_{TiN} = 5\ nm$. As the d_{TiN} is increased to 15 nm (or 20 nm), the L_{spp} increases to $\approx 11.7\ nm$ ($\approx 15\ nm$). Despite the relatively low $1/e$ decay propagation length,

the out-coupling of the SPP into the air can be achieved through scattering via the roughness of the TiN / GaN interface [12, 26].

In figure 3.7(a), a similar dependency of the Purcell factor on the TiN thickness is observed for a different spacer thickness of $d_{spr} = 25\ nm$. Figure 3.7(b) depicts the Purcell factors at the asymptotic limit of E_{sp} versus different spacer thickness, plotted for different TiN thicknesses. A reduction of the Purcell factor with the spacer thickness is observed for all cases. In general, a thicker spacer corresponds to a larger separation of the TiN and GaN:Eu layers, which in turn results in a weaker coupling of the GaN:Eu region to the SP layer. The interplay role of the conductive and the spacer layer thicknesses has also been demonstrated for the case of GaN/Ag/air interfaces [11].

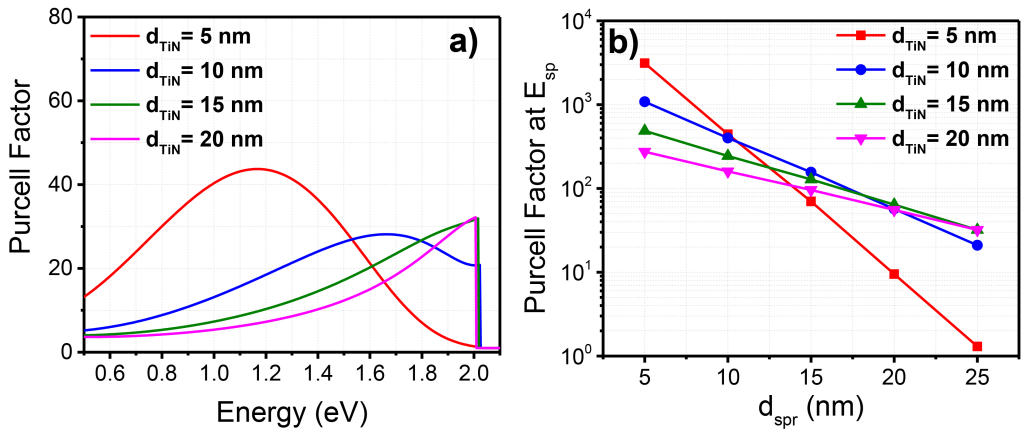

Figure 3.7: (a) Purcell factor for different TiN thickness (d_{TiN}) with GaN spacer thickness of $d_{spr} = 25\ nm$. (b) Purcell factors at the asymptotic limit of E_{sp} versus different GaN spacer thickness (d_{spr}) plotted for different thickness of TiN (d_{TiN}).

3.3.2 Effect of double metallic layer on GaN:Eu emitter

The dielectric properties of TiN strongly depend on the deposition conditions [27-33]. By tuning the deposition conditions of TiN on top of GaN, the desirable dielectric properties of TiN can be achieved. In this way the surface plasmon frequency can be

designed to cover a wide range of the visible spectral regime. In contrast to the single TiN layer presented in this work, two different layers of TiN with different dielectric functions can be used to tune the asymptotic limit E_{sp}. The concept of a double layer (DL) has been demonstrated for the case of the InGaN QWs where the thickness of the individual layers of the DL varied to tune the surface plasmon energy E_{sp} [15,16]. A similar concept can be applied for the case of a double TiN layer on top of GaN based light emitters, including GaN:Eu and InGaN QWs, which could potentially increase the Purcell factor over a wide range in the visible spectral regime.

3.4 Impact of Purcell Factor on Internal quantum efficiency

The analysis of the Purcell factor in the internal quantum efficiency of the electrically-driven GaN:Eu LEDs is presented in figure 3.8, in order to quantify the improvement presented from the use of surface plasmon structure. The device used for this calculation is identical to the device structure studies in section 2.4 of Chapter 2. The introduction of surface plasmon coupled active region in GaN:Eu results in an order of magnitude increase in the internal quantum efficiency of the electrically-driven devices, and provides a reduction of efficiency-droop up to relatively high current density (J).

A large surface plasmon coupled structure (Purcell factor ≈ 1000) results in peak internal quantum efficiency $\approx 20\%$ for $J = 0.1\ A/cm^2$. The droop suppression from the Purcell effect is found to be more significant at higher current densities. Specifically, a Purcell factor of 1000 results in an increase of the internal quantum efficiency by ≈ 16 times at a current density of $J = 10\ A/cm^2$, while the same Purcell factor results in only ≈ 1.7 times higher improvement for $J = 0.1\ A/cm^2$. For the structure without any surface plasmon coupling (reference case, with Purcell factor = 1), a

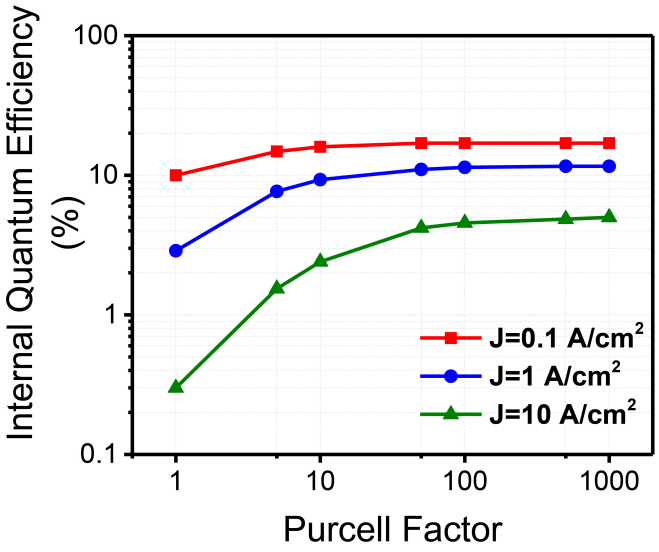

Figure 3.8: Internal quantum efficiencies of electrically-driven GaN:Eu LED as a function on Purcell enhancement factor, plotted for three different current densities (J).

significant reduction ($\approx$ 30 times) in the internal quantum efficiency is observed as the current density increases from $J = 0.1\ A/cm^2$ to $J = 10\ A/cm^2$. In contrast, the reduction of only ≈ 3.5 times in the internal quantum efficiency was observed in the structure having a large Purcell factor (≈ 1000) for the same current density range ($J = 0.1\ A/cm^2$ to $J = 10\ A/cm^2$). As mentioned earlier, the changes in the Purcell factor correspond in changes of the radiative lifetime of the GaN:Eu region (i.e Eu^{+3} ions) which affect the radiative efficiency of the system. In addition, a change in the current injection efficiency will also occur resulting in an overall change of the internal quantum efficiency of the GaN:Eu device.

3.5 Summary of Chapter 3

The metal-nitrides of hafnium-nitride (HfN), zirconium nitride (ZrN) and titanium nitride (TiN) have been investigated as plasmonic materials to enhance the internal quantum efficiency of the GaN:Eu red light emitter. It was found that among those

metal-nitrides, the TiN is the most promising material candidate for surface plasmon coupling to the GaN:Eu red light emitter. Through the tuning of the TiN and GaN spacer thickness, Purcell factors as high as 1000 can be achieved at a photon energy $\approx E_{sp}$. The coupling of the active region of a GaN:Eu LED to the surface plasmon of the TiN layer is expected to result in significant increase in the internal quantum efficiency of the electrically-driven devices. This approach will provide a pathway for achieving 20% internal quantum efficiency in electrically-driven devices. A significant reduction in drooping at high current density is expected in the surface-plasmon coupled GaN:Eu electrically-driven LED. The droop suppression in the electrically-driven surface plasmon coupled device is expected to improve by ≈ 16 times over that of the reference devices without employing surface plasmon coupling.

References

1. Orfanidis, J. S., Notes in: Electromagnetic Waves and Antennas. Rutgers University. Web page: www.ece.rutgers.edu/≈orfanidi/ewa

2. Maier, A. S., Plasmonics: Fundamentals and Applications. 2007 Edition. Springer Science Business Media LLC, 233 Spring Street, New York, NY 10013, USA.

3. Pitarke, J. M., Silkin, V., M., Chulkov, E., V., & Echenique, P., M. Theory of surface plasmons and surface-plasmon Polaritons. Inst. of Phys. Pub. Rep.on Prog. in Phys., 70, 1–87 (2007)

4. Raether, H. Surface Plasmons on Smooth and Rough Surfaces and on Gratings. Springer-Verlag Berlin Heidelberg, New York London Paris Toky

5. R. F. Wallis, R., F., & Stegeman G., I. Electromagnetic Surface Excitations Proceedings of an International Summer School at the Ettore Majorana Centre, Italy (1985). Editors Springer-Verlag Berlin Heidelberg, New York Tokyo.

6. Zhang, J., Zhang, L., & Xu, W. Surface plasmon polaritons: physics and Applications J. Phys. D: Appl. Phys. 45, 113001 (2012).

7. Okamoto, K, et al. Plasmonics toward high-efficiency LEDs from the visible to the deep-UV region. Proc. SPIE 10124, Light-Emitting Diodes: Materials, Devices, and Applications for Solid State Lighting XXI, 101240R (2017).

8. Okamoto, K. et al. High-efficiency light emission by means of exciton–surface-plasmon coupling. Journal of Photochemistry and Photobiology C: Photochemistry Reviews 32, 58–77 (2017).

9. Okamoto, K. Tunable plasmonic resonance in wide wavelength range for smart photonic and optoelectronic applications. Proc. SPIE 10536, Smart Photonic and Optoelectronic Integrated Circuits XX, 105360R (2018).

10. Gontijo, M. et al. Coupling of InGaN quantum-well photoluminescence to silver surface plasmons. Phys. Rev. B 60, 11564 (1999).

11. Neogi, A. et al. Enhancement of spontaneous emission in a quantum well by resonant surface plasmon coupling. Phys. Rev. B 66, 153305 (2002).

12. Okamoto, K. et al. Surface plasmon-enhanced light emitters based on InGaN quantum wells. Nature Mater. 3, 601–605 (2004).

13. Purcell E. M. Spontaneous emission probabilities at radio frequencies. Phys. Rev. 69, 681 (1946).

14. Okamoto, K. et al. Surface plasmon enhanced spontaneous emission rate of InGaN/GaN quantum wells probed by time-resolved photoluminescence spectroscopy. Appl. Phys. Lett. 87, 071102 (2005).

15. Paiella, R. Tunable surface plasmons in coupled metallo-dielectric multiple layers for lightemission efficiency enhancement. Appl. Phys. Lett. 87, 111104 (2005).

16. Zhao, H. P., Zhang, J., Liu, G. Y. & Tansu, N. Surface plasmon dispersion engineering via double metallic Au/Ag layers for III-nitride based light-emitting diodes. Appl. Phys. Lett. 98, 151115 (2011).

17. Lin, J., Mohammadizia, A., Neogi, A., et al. Surface plasmon enhanced UV emission in AlGaN/GaN quantum well. Appl. Phys. Lett. 97, 221104 (2010).

18. Johnson, P. B and Christy, R. W. Optical constants of the noble metals. Phys. Rev. B 6, 4370 (1972).

19. West, P. R. et al. Searching for better plasmonic materials. Laser Photonics Rev. 4, 795 (2010).

20. Steinmüller-Nethl, D., Kovacs, R., Gornik, E. & Rödhammer, P. Excitation of surface plasmons on titanium nitride films: determination of the dielectric function. Thin Solid Films 237, 277-281 (1994).

21. Hibbins, A.P., Sambles, J. R. & Lawrence, C. R. Surface plasmon-polariton study of the optical dielectric function of titanium nitride. J. Mod. Opt. 45, 2051-2062 (1994).

22. Chen, N. C. et al. Excitation of surface plasma wave at TiN/air interface in the Kretschmann geometry. J. Appl. Phys. 109, 043104 (2011).

23. Naik, V. et al. Titanium nitride as a plasmonic material for visible and near-infrared wavelengths. Opt. Mat. Exp. 4, 478-489 (2012).

24. Naik,V. G., Shalev, V. M. & Botlasseva A. Alternative plasmonic materials: beyong gold and silver. Adv. Mater. 25, 3264-3294 (2013).

25. Gu, Z. et al. Optical reflectivity and hardness improvement of hafnium nitride films via tantalum alloying. Appl. Phys. Lett. 109, 232102 (2016).

26. Barnes, W. L. Light-emitting devices: Turning the tables on surface plasmons. Nature Mat. 3, 588-589 (2004).

27. Wiemer, C., Lévy, F. & Bussy, F. Determination of chemical composition and its relationship with optical properties of Ti-N and Ti-V-N sputtered thin films. Surf. Coat. Technol. 68, 181–187 (1994).

28. Humlicek, J. et al. Ellipsometry and transport studies of thin-film metal nitrides. Thin Solid Films 332, 25–29 (1998).

29. Patsalas, P. & Logothetidis, S. Optical, electronic, and transport properties of nanocrystalline titanium nitride thin films. J. Appl. Phys. 90, 4725–4734 (2001).

30. Postava, K., Aoyama, M. & Yamaguchi, T. Optical characterization of TiN / SiO2(1000 nm) / Si system by spectroscopic ellipsometry and reflectometry. Appl. Surf. Sci. 175, 270–275 (2001).

31. Huber, P., Manova, D., Mändl, S. & Rauschenbach B. Optical characterization of TiN produced by metal-plasma immersion ion implantation. Surf. Coat. Technol. 142, 418–423 (2001).

32. Naik, G. V., Kim, J., Boltasseva, J. Oxides and nitrides as alternatives plasmonic materials in the optical range. Opt. Mat. Exp. 1, 1090 (2011).

33. Patsalas, P., Kalfagiannis, N. & Kassavetis, S. Optical properties and plasmonic performance of titanium nitride. Materials 8, 3128-3154 (2015).

Chapter 4

Organometalic Vapor Phase Epitaxy of III-Nitrides

4.1 OMVPE epitaxial system

Organometalic vapor phase epitaxy (OMVPE) is a compound semiconductor epitaxial growth technique that is widely used both in the industry and in research facilities. The growth of the of the III-nitrides takes place in a high vacuum chamber with typical growth pressures ranging from 20 to 500 $mtorr$. The growth of the semiconductor compounds is a result of complex chemical reactions of gases at the surface of a substrate under certain temperature and pressure. Figure 4.1 depicts the main proceces during the epitaxy of the film. The purpose of this chapter is to give an introduction to the OMVPE system that was used in the framework of this thesis and also introduce in the derivation of the V/III molar ratio, which is one of the main parameters to achieve high quality epitaxial films. The growth of the III-nitride coimpunds and epitaxial structures for visible light emission, is presented in Chapter 5 and Chapter 6 respectively.

In this work, the growth of the Ill-nitride compounds was performed in vertical-

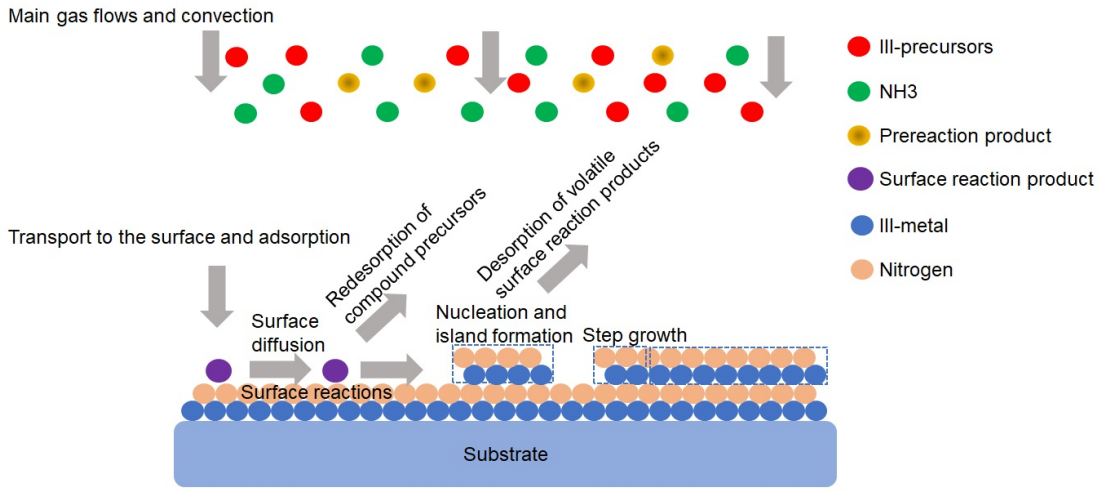

Figure 4.1: Processes during OMVPE epitaxy of III-nitride compounds.

type turbo-disk rotating showerhead OMVPE reactor (VEECO P-75). The schematic of the reactor is shown in figure 4.2. The main components of this particular type of reactor are grouped into three parts: 1) gas and metalorganic (MO) sources delivery system, 2) growth chamber, and 3) pressure maintenance system. The gas delivery system mainly consists of stainless-steel tubes, pressure regulators and electronically-controlled pneumatic valves, capable of delivering high-purity gases, i.e. parts-per-billion (ppb) level impurity, into the growth chamber.

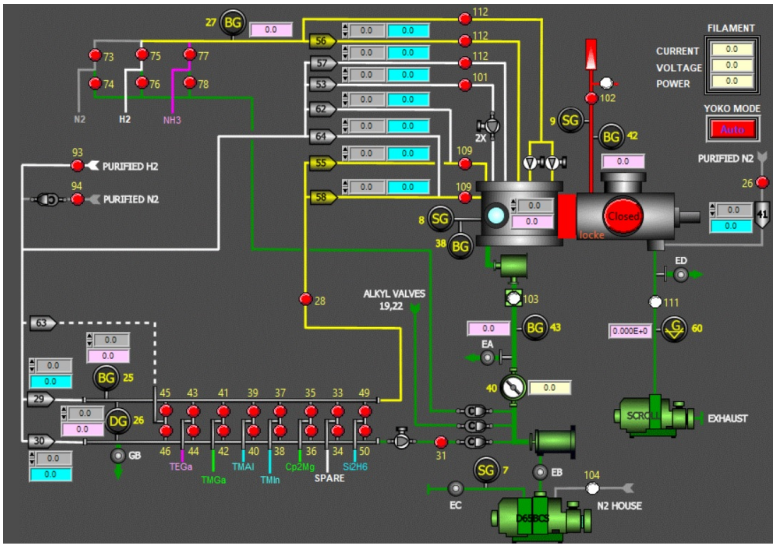

Figure 4.2: Schematics of the OMVPE growth chamber as it is seen from the user's interface program.

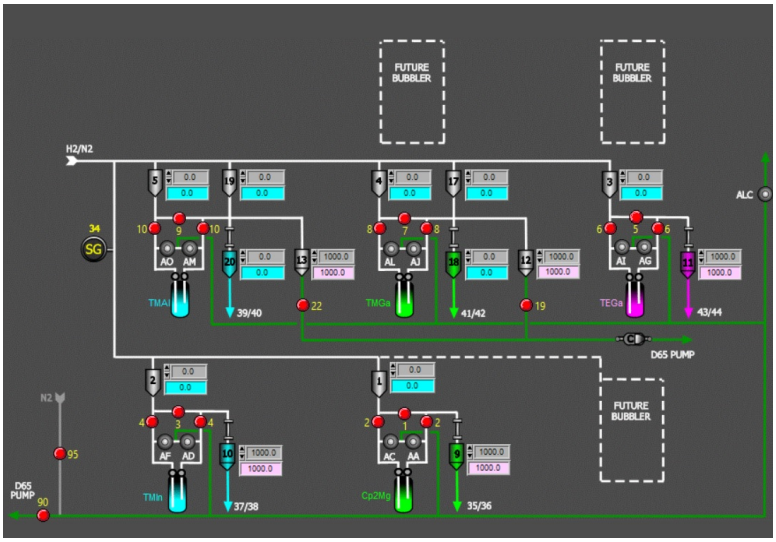

Figure 4.3: Schematics of the MO sources and bubblers as it they are seen from the user's interface program.

Gas and metalorganic (MO) sources delivery system

For the growth of all the Ill-nitride compounds, the following MO sources are used: trimethylgallium ($TMGa$), triethylgallium ($TEGa$), trimethylindium ($TMln$) and trimethylaluminum ($TMAl$). The MO source of bis cyclopentadienyl magnesium ($Cp2Mg$) is also employed as p-dopant. Nitrogen (N_2) (or hydrogen (H_2)) is used as the carrier gas for the III-precursor. While the MO sources provide the desirable III-precursor, ammonia (NH_3) is used to provide the atomic nitrogen (V-precursor). Another V precursor which is used to provide n-type doping in III-nitrides is silane (SiH_4). In addition, hydrogen (H_2) and nitrogen (N_2) are employed as ambient gases during growth.

Highly purity H_2 is generated in-house by electrolysis process by Teledyne HM-100 H_2 generator and further purified by an SAES Getter H_2 purifier. House N_2 and NH_3 gases are also purified by an Aeronex gas purifiers. The gas flow is individually regulated by mass flow controllers (MFC) calibrated to the respective input gas pressure. The MO source manifolds are connected to the gas delivery system. Figure 4.2 depicts the schematic of the metalorganic sources used in this work. The

MO sources are contained inside cylindrical stainless steel called 'bubblers', which in turn are immersed into a temperature-controlled baths. The temperature of the MO source is crucial because it determines the vapor pressure and consecutively the partial pressure in the growth chamber. In this work, nitrogen is used as the carrier gas of the MO source. The carrier gas is passed through a mass flow controller to regulate its flow prior to its entrance to the inlet of the MO bubbler. The carrier gas picks up the MO vapor and carries it into the growth chamber. The vapor and bubbler pressure can be directly correlated to the actual flow of the MO source.

Growth chamber

The carrier gas (with the MO source), as well as, ammonia (NH_3) and other gases (H_2, N_2) are introduced into the growth chamber from the top, where they pass through a metallic screen with a 'showerhead' configuration. This configuration allows flexibility in specifying the amount of flows and the relative position of different vapor sources impinging on the substrate. The substrate utilized for growth, is usually sapphire (for u-GaN growth) or u-GaN/sapphire (for III-nitride alloy / semiconductor structure growths). The substrate is placed on top of a circularly-indented 2" graphite platter coated with silicon carbide (SiC). Bellow the platter is a resistive-heating filament, which is connected to a power supply. The platter is mounted on top of a spindle, which is connected to a motor that spins the substrate/sample during the growth. A rotational speed of 1100- 1500 *rpm* is typically employed. The rotation of the substrate/sample also assists to a viscously drug/pulling of gases straight down and redirecting them outward over the substrate carrier. During the growth, the temperature of the sample is monitored by RealTemp monitoring system, which measures the 'glow' of the sample at high temperature (T $>$ 450 ^{o}C). Additionally, the RealTemp also serve as film thickness and growth rate monitor, where the growth rate is measured in-situ from the peaks and valleys of the reflectivity plot. The

growth chamber is double-walled and cooled by temperature-controlled recirculating water loop. The sample is transferred into and out of the growth chamber through a separate loading area called the load-lock. The load-lock is kept under vacuum (0 psi) and is isolated from the growth chamber by a gate-valve. The processes of the load-lock routine (sample loading into the load-lock) and gate-valve routine (sample loading into the growth chamber) are automatically via a control panel. In addition, the gas flows, growth pressure and temperature are controlled via a program interface (LabView) which allows the user to build a desirable recipe for a particular growth.

Pressure maintenance system

The pressure maintenance system consists of a particle filter, throttle valve, EBARA vacuum pump and exhaust line connected to the Vector scrubber. Throttle valve and EBARA pump regulate the pressure of the growth chamber. The gases in the outlet of the growth chamber pass through a particle filter trap prior to being pumped out by the Ebara AA70W pump. The outlet of the Ebara pump is connected with a wet scrubber unit of Vector Ultra 3001 that provides abatement of toxic, corrosive, and water-reactive gases from process equipment effluent. The scrubber, which utilizes water and N_2, is used to purify the gases before they get passed onto the main exhaust line for further scrubbing and released into the atmosphere. The throttle valve is located between the growth chamber and the Ebara pump and is used to control the growth chamber pressure by tuning its opening from 0% to 100%. Other supporting facilities include heat exchanger for pumps and reactor cooling, process gas manifolds for gas flow controlling, gas purifiers for N_2, H_2, NH_3, etc.

4.2 Epitaxial growth parameters

One of the most important parameters for the epitaxial growth of high quality III-nitride compound semiconductors, besides the growth pressure (P_{CG}) and temperature(T_g), is the V/III molar ratio during the epitaxy. The V/III molar ratio is directly related to the flow of the carrier gas and NH_3 and can be derived as follows:

The vapor pressure of the MO source inside the bubbler is a function of temperature and can be described from the followin empirical equation:

$$P_{vapor} = 10^{(a-b)/T} \tag{4.1}$$

with a and b the empirical parameters which are shown in Table 4.1.

MO Source	a	$b\ (K)$	$T\ (K)$	$P_{vapor}\ (Torr)$	$P_{Bubbler}\ (Torr)$
$TMGa$	8.07	1703	273.15	64.443	900
$TEGa$	8.083	2162	283.15	2.802	900
$TMIn$	10.98	3204	293.15	1.123	900
$TMAl$	8.224	2134.83	293.15	8.742	900

Table 4.1: Parameters of the Drude-Lorentz model for the different metal-nitrides investigated in this study.

For the group III-precursors that use a single dilution configuration the actual flow ($sccm$) is calculated by:

$$F_{III} = F_{III} \times \frac{P_{vapor}}{P_{Bubbler} - P_{vapor}} \tag{4.2}$$

It is important to mention that the partial pressures of the $TMGa$ and $TMAl$ are much higher than those of $TMIn$ and $TEGa$. Therefore, a double dilution configuration is employed for the $TMGa$ and $TMAl$ in order to reduce the flow and avoid any possible precipitation and contamination of the precursors in the gas line or the growth chamber. Moreover, the double dilution assists to the more precise control of

the flow. For the case of the double dilution, the actual flow of the the III-precursor is given by:

$$F_{III} = F_{III\_Main} \times \frac{P_{vapor}}{P_{Bubbler} - P_{vapor}} \times \frac{F_{III\_DD}}{F_{III\_Main} - F_{III\_Push}} \tag{4.3}$$

where F_{III_Main}, F_{III_Push}, and F_{III_DD} are flow rates of pure N_2 carrier gas going through the bubbler, pure N_2 push gas, and double dilution of N_2 carrying MO source, respectively. They are controlled by the main MFC, Push MFC, Double Dilute MFC (for the case of $TMGa$ this corresponds to main MFC = MFC - 4, Push MFC = MFC - 18 Double Dilute MFC = MFC - 17 as shown in figure x).

Therefore, the partial pressure of the III-precursors $P_{III\_partial}$ (mtorr) in the growth chamber is given by:

$$P_{III\_partial} = P_{GC} \times \frac{F_{III}}{F_{Ambient\_gas} + F_{NH_3}} \tag{4.4}$$

The partial pressure of the ammonia (NH_3) $P_{V\_partial}$ is obtained from the following equation:

$$P_{V\_partial} = P_{GC} \times \frac{F_{NH_3}}{F_{Ambient\_gas} + F_{NH_3}} \tag{4.5}$$

where the $F_{Ambient\_gas}$ represents the total flow rate of ambient gas of N_2 and H_2 flowing into the chamber during the growth. The chamber growth pressure (P_{CG}) is set by the growth recipe and is controlled by the throttle valve underneath the chamber. The V/III molar ratio of the growth is defined as:

$$V/III = \frac{P_{V\_partial}}{P_{III\_partial}} \tag{4.6}$$

Chapter 5

Pulse-OMVPE Growth Mode of InN

5.1 Motivation for bulk InN growth via the pulse-OMVPE growth technique

In virtue of its narrow band-gap of $\approx 0.7\ eV$, indium nitride (InN) is an important semiconductor material for optoelectronic applications including solar cells, THz generation, high-speed electronic devices and light emitters [1-13]. However, challenges in growing high quality epitaxial InN films via the metal-organic chemical vapor deposition (OMVPE) technique still hinder the development of InN based devices. These challenges are attributed to the low dissociation temperature of InN ($\approx 600\ ^{o}C$), and the low pyrolysis efficiency of ammonia (NH_3) at low growth temperatures. These challenges impose a narrow set of growth conditions that need to be met in order to avoid the formation of metallic-In on the surface of the InN films. An effective method to overcome these issues is the use of the pulsed-OMVPE technique. In this growth technique, the indium precursor is supplied into the chamber in pulses while the supply of NH_3 is constantly flowing. For the case of the InN epitaxial growth,

it has been shown that the use of the pulsed-OMVPE mode results in the increased adatom mobility of the In on the surface of the substrate, the etching of the metallic-In droplets during the off state of the indium precursor due to hydrogen generation - arising from the pyrolysis of the NH_3, and the consumption of metallic-In by reactive nitrogen species [9-11]. In addition, the use of the pulsed-OMVPE allows a wider window for optimized growth conditions to achieve high quality metallic-In free InN epitaxial films [9-11, 14-17].

In this work, the pulsed-OMVPE technique was employed for the growth of the InN in a vertical-flow Veeco P-75 reactor. Unintentionally doped GaN templates (3 μm), grown on c-plane sapphire substrates at a pressure of 500 $torr$ and a temperature of $\approx$ 1050 ^{o}C, were used as the substrates for the InN growths. The structural characteristics of the films were determined by X-ray rocking curve scans of the (002) plane and the full width at half maximum (FWHM) was found to be $\approx$ 200 $arcsec$. The electron background concentration was determined via Hall measurements in the Van der Pauw configuration and it was found to be in the range of n $\approx$ 3 x 10^{16} cm^{-3} with an electron mobility of $\mu_e \approx 430\ cm^2/Vs$. For the growth of the InN, the NH_3 was constantly supplied into the reactor while the trimethylindium ($TMIn$) precursor was introduced via the nitrogen carrier gas (N_2) into pulses. Four different growth studies were carried out to investigate the effect of growth temperature, V/III molar ratio and pulse characteristics - pulse period (T_{p}) and duty cycle (T_{dc}) -, on the structural and electrical properties of the films. The duty cycle (T_{dc}), at a particular pulse period (T_{p}), determines the time duration that the $TMIn$ precursor is flowing into the chamber. For each InN growth, the total pressure was set to 200 Torr and the delivery of the $TMIn$ precursor was set to 5.5 $\mu mole/min$ for the "on" state, while the number of the periods was tuned accordingly so that the total $TMIn$ supply time was kept constant and equal to 35 minutes. The growths resulted in film thicknesses in the range of $\approx$ 100-200 nm, as it was estimated through the

reflectance oscillations at 930 nm during the growth. The structural properties were studied, using an Empyrean Panalytical Malvern X-ray diffractometer with parallel beam geometry and CuKa radiation. Atomic force microscopy (AFM) in tapping mode was used to evaluate the surface morphology of the films in a 5 μm x 5 μm surface area, while the electrical properties of the films were studied via an Ecopia HMS - 3000 Hall measurement system in a Van der Pauw configuration. The present findings indicate that metallic-In-free InN films with relatively low structural defect densities, sheet carrier concentrations (n_s) and high electron mobilities (μ_e) can be fabricated using the pulsed-OMVPE growth technique.

Despite the suggestion of the use of the pulse-OMVPE mode, as the method to eliminate any metallic-In from the epitaxial InN films, metallic-In is still present, especially at low V/III ratios. As it is shown from the XRD pattern in figure 4.1, metallic-In is still present when the V/III ratio is $\approx$ 17000 , growth temperature T= 540 ^oC. The metallic-In was able to be removed through HCL etching for 3 min at 100 ^oC. However, as it will be shown later in this chapter, the formation of metallic-In depends upon a combination of parameters and growth temperature operating regimes. Nevertheless, the use of the pulse-OMVPE allows a wider window for optimized growth conditions to achieve the desirable properties of the epitaxial InN films.

5.2 Epitaxy of InN

5.2.1 Effect of growth temperature T_{g}

The effect of the growth temperature (T_{g}) was studied under a V/III molar ratio $\approx$ 39000, pulse period $T_{\mathrm{p}} = 26\ s$ and duty cycle $T_{\mathrm{dc}} = 50\%$. In figure 5.2(a), the XRD patterns of the coupled $\omega/2\theta$ scan revealed a wurtzite InN (002) peak located at $\approx 15.65^{\mathrm{o}}$ and the GaN substrate (002) peak located at $\approx 17.30^{\mathrm{o}}$. In addition, for

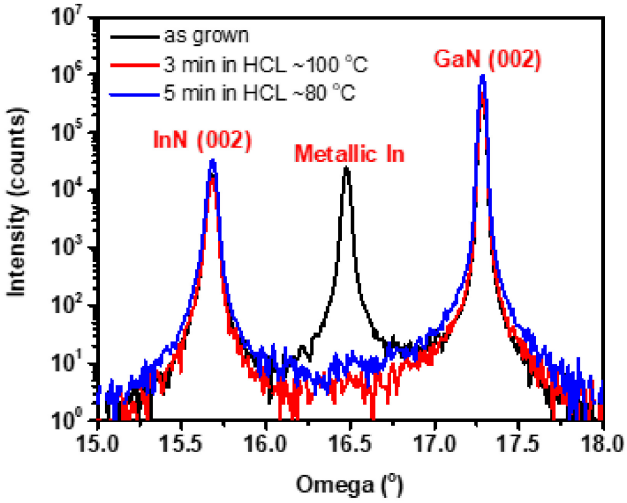

Figure 5.1: Pulse OMVPE growth of InN on GaN/sapphire with growth conditions of V/III ratio of $\approx$ 17000, growth temperature of $T = 540\ ^{o}C$ and pulsing characteristics of T_{p} =26 s and $T_{\mathrm{dc}} = 50\%$. Metallic-In is still present at these growth conditions.

the sample grown under the lowest temperature of 460 ^{o}C an extra peak located at $\approx$ 16.40^{o} was observed, which corresponds to the cubic metallic-In (101) crystal plane. The presence of metallic-In is probably attributed to the low NH_3 dissociation at this low growth temperature. To evaluate the crystal structure quality of the InN layers, a rocking curve scan for the (002) plane (symmetric scan) and (105) plane (asymmetric scan) was performed. It is well known that for the III-nitrides, the full width at half maximum (FWHM) of the symmetric scan corresponds to the lattice distortions due to screw type of threading dislocations, while that of the asymmetric scan is related to any type of threading dislocations that distort the crystal structure (screw, edge and mixed screw-edge threading dislocations) [19]. In addition, it has been shown that the threading dislocations significantly affect the mosaic, tilt and twist of the InN epitaxial films [20,21]. Nevertheless, in this study the FWHM of the symmetric and asymmetric rocking curve scans are expected to give a qualitative view of the crystal structure quality of the InN films.

As the growth temperature increases from 460 ^{o}C to 535 ^{o}C (low temperature

regime), the FWHM of the rocking curve, shown in figure 5.2(b), varies slightly in the range of 343-408 *arcsec* and then rapidly increases towards 1647 *arcsec* for higher growth temperatures ($T_g > 535\ ^oC$) (figure 5.2(b)). In contrast, the FWHM of the (105) plane gradually increases from 705 to 1712 *arcsec* with increasing the growth temperature. This is an indication that the crystal structure quality of the InN films degrades with increasing the growth temperature. This might be attributed to the generation of threading dislocations and the increase of the mosaicity of the InN films.

As shown in figure 5.2(c) and 1(d) the AFM images revealed a 3-dimensional morphology - due to large lattice mismatch between the GaN and InN ($\approx 10\%$) - of the surface of the films consisting of grains, whose size and density were dependent on the growth temperature. More specifically, at higher growth temperatures, the size of the grains increased, and their density became smaller resulting in higher surface roughness and an overall increasing trend of the RMS roughness of the films. Moreover, the larger grains are expected to be more tilted and twisted with respect to each other contributing more to the broadening of the rocking curve linewidths [20]. This controversial trend of the crystal structure quality with increasing the growth temperature has also been reported elsewhere [22].

The electrical properties of the films for the growth temperature study are shown in figure 5.2(e). The InN films exhibited n-type conductivity. In general, the InN films exhibit an intrinsic n-type conductivity which is associated with several sources, including intrinsic defects such as nitrogen vacancies, extrinsic defects such as oxygen and hydrogen impurities, as well as, a surface electron accumulation layer [23-28]. The extend at which each of the above sources contributes to the electrical characteristics, is reflected on their dependency on the growth parameters. In this study, the electrical properties of the films are improved with increasing the growth temperature. The sheet carrier concentration decreases (n_s) which is an indication that elevated growth temperatures eliminate possible defects that would act as donors. In this particular

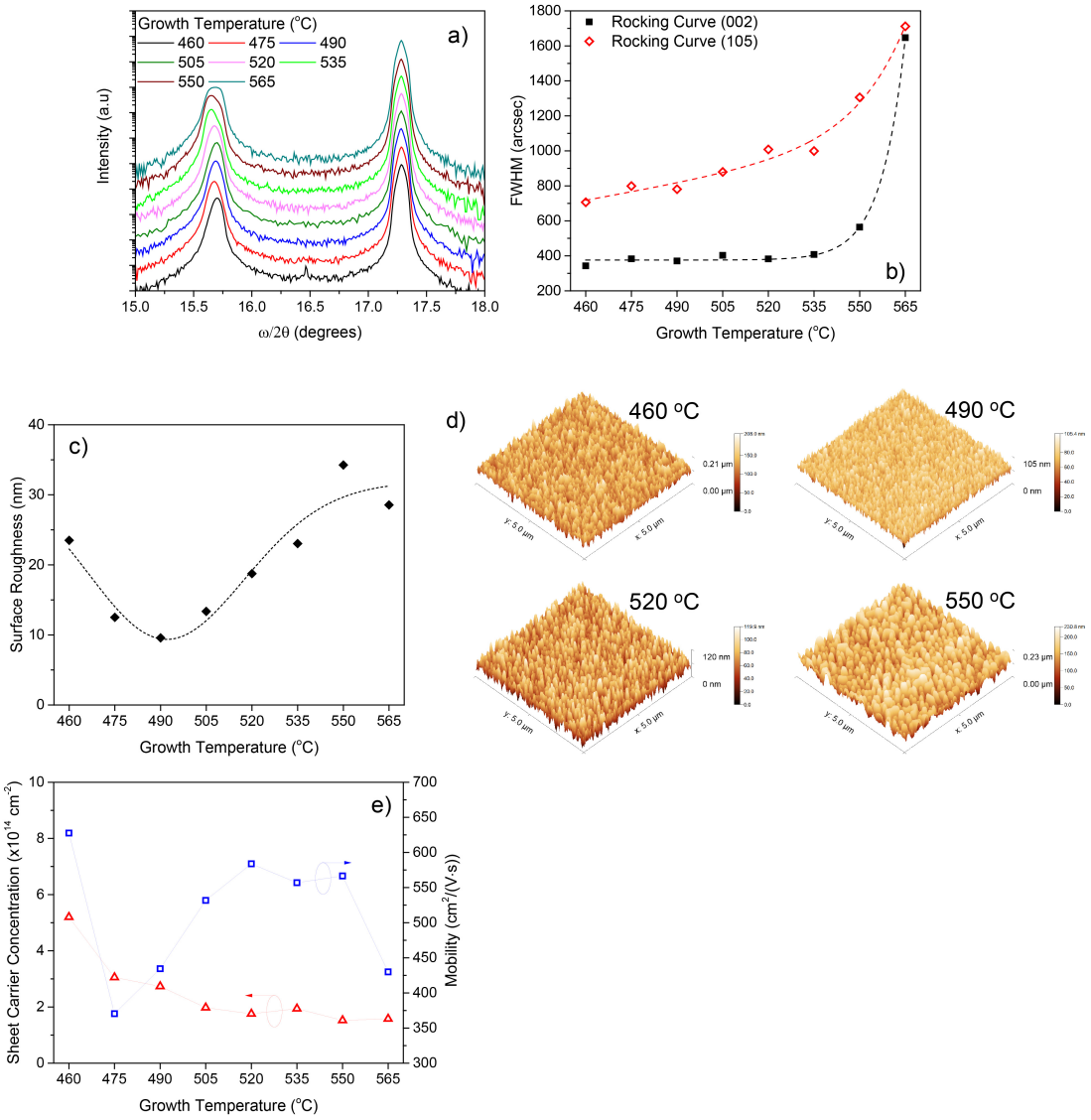

Figure 5.2: $\omega/2\theta$ XRD scans, b) full width at half maximum of symmetric (002) and asymmetric (105) rocking curve scans, c) RMS surface roughness and d) surface characteristics of InN grown at different growth temperatures. e) Hall electrical characteristics of the films measure via the Van der Pauw method.

case, considering the low growth temperature regime of InN, we believe that the density of nitrogen vacancies (V_{N}) is reduced due to higher efficiency of NH_3 pyrolysis and atomic nitrogen production at elevated temperatures. Furthermore, despite the statistical variation, the carrier mobility (μ_e) exhibits an increase with the growth temperature, which is attributed to the reduction of scattering centers such as grain boundaries. An average mobility of $\mu_e \approx 570\ cm^2/Vs$ with an average sheet carrier concentration of $n_s \approx 1.6$ x $10^{14}\ cm^{-2}$ was observed for growth temperatures in the range of 505-550 ^{o}C. In addition, the sample grown under the lowest temperature, exhibited the highest sheet carrier concentration ($n_s \approx 5$ x $10^{14}\ cm^{-2}$) and mobility ($\mu_e \approx 627\ cm^2/Vs$), due to the presence of the metallic-In.

5.2.2 Effect of V/III molar ratio

For the study of the effect of V/III molar ratio, the growth temperature was set at $T_{\mathrm{g}} = 505\ ^{o}C$, and the pulsing period and duty cycle were set at $T_{\mathrm{p}} = 26\ s$ and $T_{\mathrm{dc}} = 50\%$, respectively. For each growth, the NH_3 flow varied in order to achieve V/III molar ratios of 24500, 29000, 32000, 34000 and 39000. In figure 5.3(a) the XRD pattern of an $\omega/2\theta$ coupled scan is shown. The peaks corresponding to wurtzite InN (002) and wurtzite GaN (002) planes are clearly observed at $\approx 15.65^{o}$ and $\approx 17.30^{o}$, respectively. For the growth under the lowest V/III molar ratios of 24500 and 29000, a peak corresponding to the cubic-In (101) crystal plane appeared. The lower V/III molar ratio corresponds to lower NH_3 flow into the chamber, which limits the production of atomic nitrogen and hydrogen to effectively etch / consume the metallic-In during the "off" state of the pulse, respectively. The FWHM of the rocking curve of the (105) plane indicates an increase in the crystal defect density and mosaicity as the V/III molar ratio increased (figure 5.3(b)).

The surface roughness, as well as the surface morphology for films does not significantly changes under different V/III molar ratios except for the film grown under

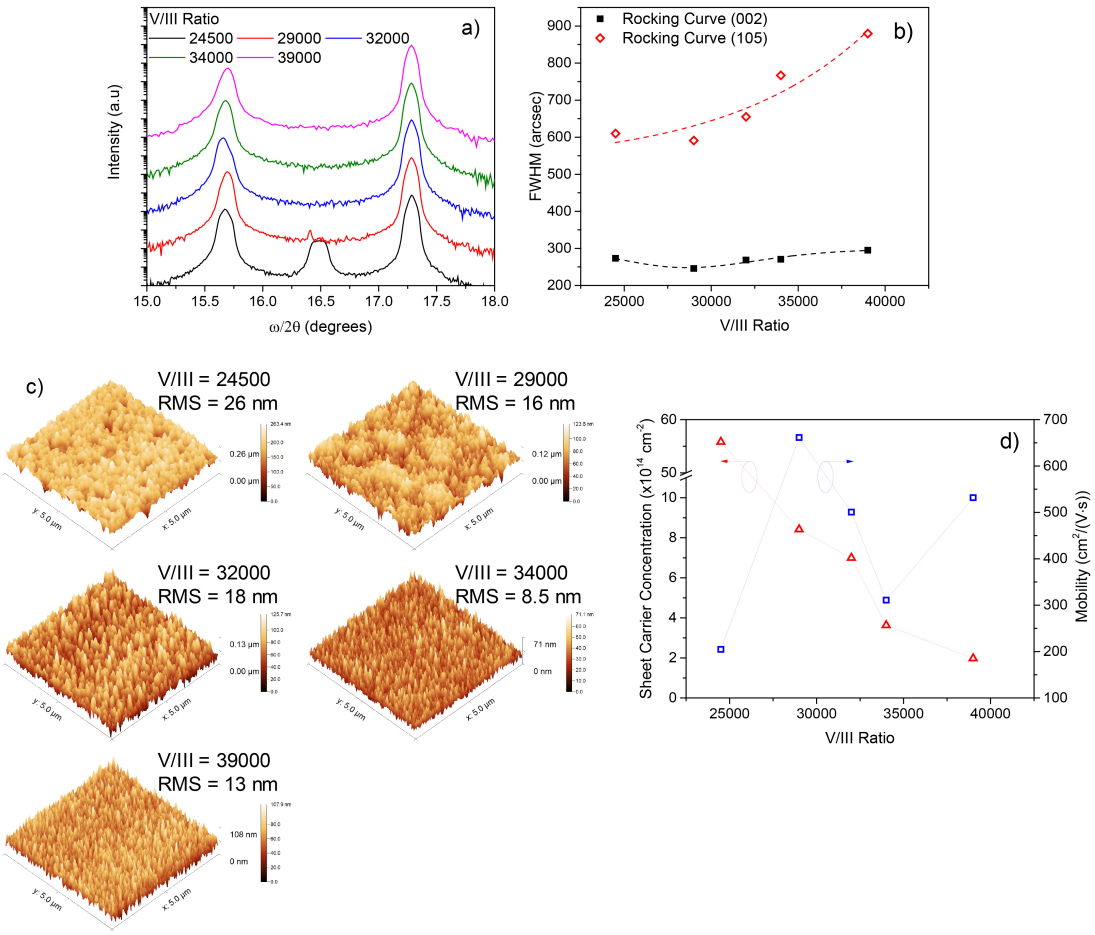

Figure 5.3: $\omega/2\theta$ XRD scans, b) full width at half maximum of symmetric (002) and asymmetric (105) rocking curve scans, c) surface morphology and d) Hall electrical characteristics of the films measured via the Van der Pauw method at different V/III ratios.

the lowest V/III ratio of 24500 (figure 5.3(c)). It is known that during the growth of III-nitrides (i.e GaN), higher V/III ratios enhance the nuclei and grain density and assist to the lateral (2-dimensional) growth of the grains. However, for the case of InN the large lattice mismatch between the InN and the GaN template cannot accommodate a 2-dimmensional growth. Similar observations regarding the trends of surface roughness of the pulsed-OMVPE-grown InN films have been reported by Jamil et al. [10].

The electrical characteristics obtained from the Hall measurements are shown in figure 5.3 (d). The sample grown under the lowest V/III ratio of 24500 exhibits a very high sheet carrier concentration (ns) which arises from the presence of the metallic-In in the film. In addition, its low mobility of $\mu_e \approx 205\ cm^2/Vs$ can be attributed to scattering from grain boundaries, as well as to carrier-carrier scattering mechanisms. Overall, the electron background concentration was reduced at higher V/III molar ratios. We expect that higher V/III molar ratios result in higher production of atomic nitrogen and suppress defect formation, especially nitrogen vacancies (V_N), which may act as intrinsic donors. On the contrary, the measured mobilities of the films exhibit a large variation, which can be attributed to changes of the surface morphologies of the InN films. The lowest sheet carrier concentration was measured ns $\approx$ 1.97 x 10^{14} cm^{-2} with a corresponding carrier mobility of $\mu_e \approx 531\ cm^2/Vs$ under a V/III molar ratio of 39000.

5.2.3 Effect of pulse characteristics – pulse period & duty cycle

The effects of the pulse period (T_{p}) and the duty cycle (T_{dc}) were studied under a growth temperature of $T_{\mathrm{g}} = 505\ ^{\circ}C$ and a V/III molar ratio of 34000. A duty cycle of $T_{\mathrm{dc}} = 50\%$ was selected for the pulse period study, while a period of $T_{\mathrm{p}} = 26\ s$ was selected for the duty cycle study. An $\omega/2\theta$ coupled scan revealed the

characteristic wurtzite (002) InN peak and no metallic-In presence was detected in both studies (Figure 5.4(a), 5.4(a)). Table 5.1 and Table 5.2 present the FWHM of the symmetric and asymmetric rocking curves for the pulse period and duty cycle studies respectively. As the pulse period increases from $T_{\mathrm{p}} = 16\ s$ to $T_{\mathrm{p}} = 26\ s$, the FWHM of the (002) and (105) planes varies slightly in the range of 332-368 *arcsec* and 610-731 *arcsec* respectively. Similar behavior is observed for the case of the duty cycle. Under these growth conditions, the dependency of the linewidth variations of the rocking curves on the pulse characteristics is minimal compared to the cases of the growth temperature and V/III molar ratio studies. In addition, as shown in Figure 5.4(b) and 5.4(d) the surface morphology of the InN films with longer pulsing periods and longer duty cycles resulted in larger and less dense islands, which effectively increased the surface roughness of the InN films. In Figure 5.5(a) and 5.5(b)) the electrical characteristics of the films are shown. The lower pulsing periods and duty cycles resulted in a lower background electron concentration. More specifically, the sheet carrier concentration (n_s) decreased from 8.4 x 10^{14} cm^{-2} to 4.3 x 10^{14} cm^{-2} when the pulse period reduced from $T_{\mathrm{p}} = 46\ s$ to $T_{\mathrm{p}} = 16\ s$, respectively. Similarly, the sheet carrier concentration decreases by more than half, reducing from 7.54 x 10^{14} cm^{-2} down to 3.49 x 10^{14} cm^{-2} with reducing the duty cycle. Moreover, for both studies the electron mobility (μ_e) is found to vary within the range of $\mu_e \approx$ 310-610 cm^2/Vs and is probably associated with the variations in the crystal structure quality of the films.

The changes of the duty cycle alter the effective V/III molar ratio as

$$\left(\frac{V}{III}\right)_{eff} = \left(\frac{V}{III}\right)_{nom} \left(1 + \frac{1 - T_{dc}}{T_{dc}}\right) \tag{5.1}$$

where, T_{dc} is the duty cycle of the pulsed-OMVPE mode and $(\frac{V}{III})_{nom}$ the nominal V/III molar ratio during the growth. It is obvious from the above relation that for a given nominal V/III molar ratio, the effective V/III molar ratio increases for lower

duty cycles - of a given T_{p} - and remains unchanged with variations in the pulse period T_{p} - of a given pulse duty cycle T_{dc} -. As mentioned earlier, the role for the pulsed-OMVPE growth mode is to allow sufficiency time for the formation of metallic-In free InN films. From the observed experimental trends we intuitively believe that the reduction of the pulse period - under a pulse duty cycle of $T_{\mathrm{dc}} = 50\%$ - , as well as the reduction of the duty cycle - under a pulse period of $T_{\mathrm{p}} = 26\ s$ - , decreases the scattering of the atoms on the surface and accommodates a better adatom mobility of the In on the surface of the films. Hence, better incorporation of the In and N atoms in the crystal lattice is expected resulting in smoother surfaces as well as in less background electron concentration due to the suppression of nitrogen vacancies (V_N). From these observations it can be suggested that a pulsed-OMVPE growth mode with low pulse period with relatively low duty cycle would be advantageous for the formation of high-quality InN with smooth surfaces and low background electron concentration.

Pulse Period T_p	FWHM (002) $(acsec)$	FWHM (105) $(arcsec)$
16 s	368	731
26 s	397	766
36 s	386	743
46 s	332	610

Table 5.1: Full width at half maximum of symmetric (002) and asymmetric (105) rocking curve scans for the pulse period study with $T_{dc} = 50\%$.

Pulse Period T_{dc}	FWHM (002) $(acsec)$	FWHM (105) $(arcsec)$
30%	338	666
40%	336	719
50%	396	767
60%	332	609
70%	367	653
80%	350	675

Table 5.2: Full width at half maximum of symmetric (002) and asymmetric (105) rocking curve scans for the duty cycle study $T_p = 26\ s$.

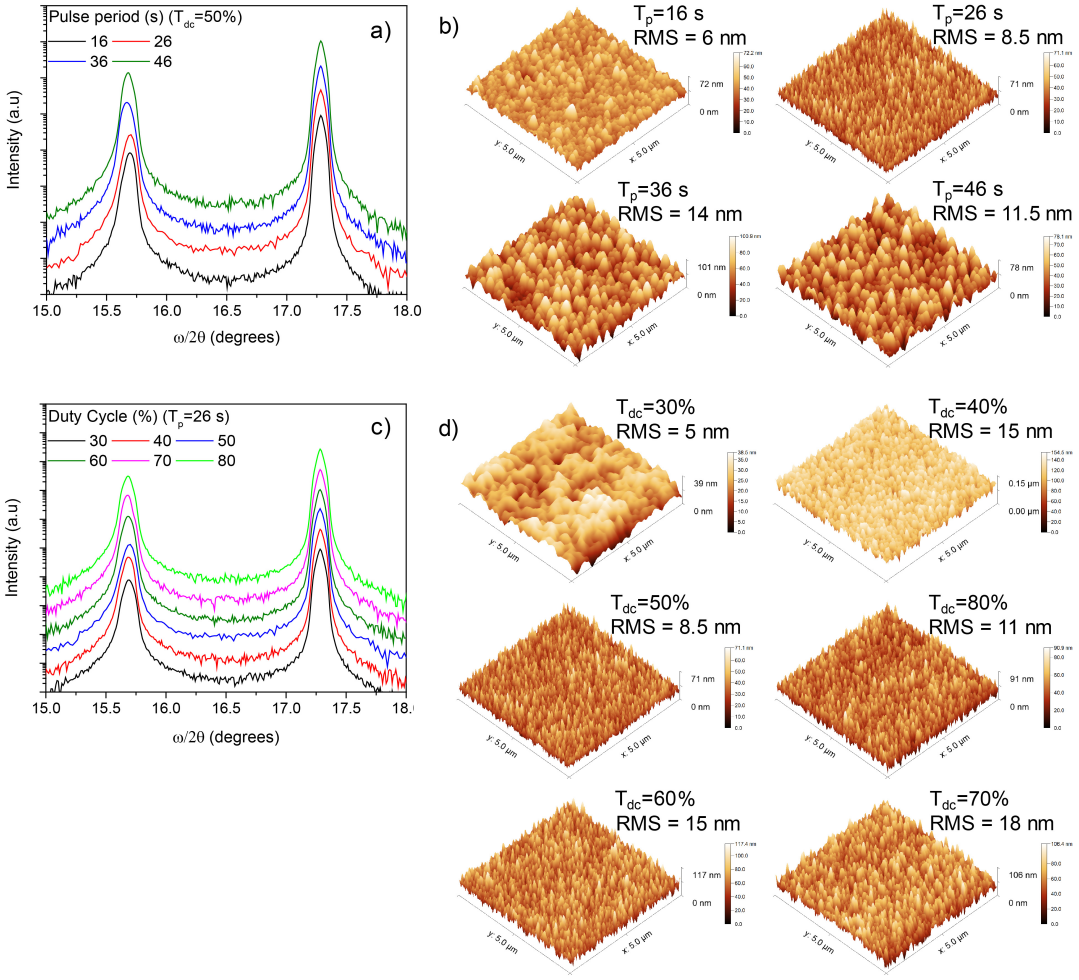

Figure 5.4: a-b) $\omega/2\theta$ XRD scans and surface morphology at different pulse periods T_{p}. c-d) $\omega/2\theta$ XRD scans and surface morphology at different pulse duty cycles T_{dc}.

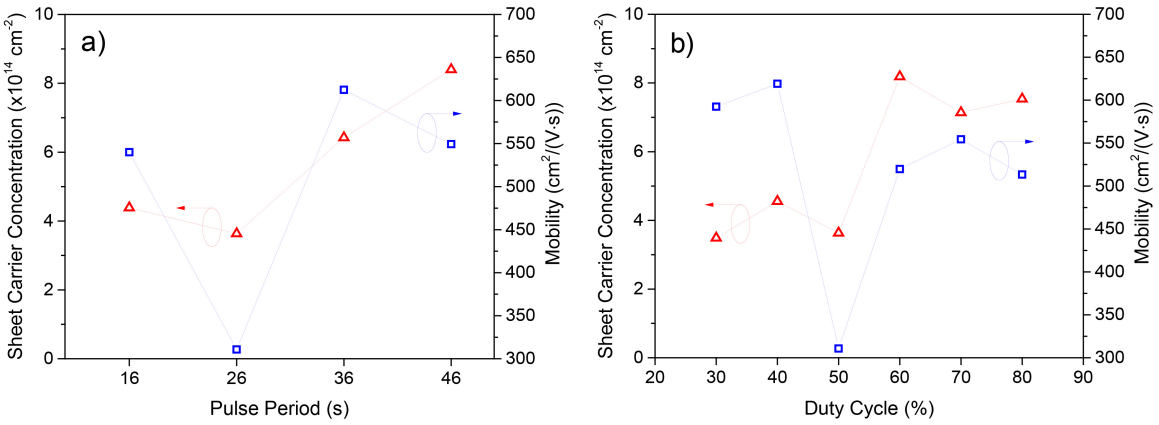

Figure 5.5: Hall electrical characteristics of the films measured via the Van der Pauw method at different a) Pulse Periods T_{p} and b) Pulse Duty Cycles T_{dc}.

5.3 Comparison with similar studies

Table 5.3 presents data reported by various groups on InN grown via the pulsed-OMVPE technique. These data correspond to InN with thicknesses between 150-300 nm grown under optimal conditions [15-18,22]. For most of the studies, the low sheet carrier concentration ($n_s \approx 1$ x 10^{14} cm^{-2}), is accompanied by a large FWHM of the rocking curve of the (002) crystal plane (> 1000 $arcsec$). In addition, this trend is followed by either high surface roughness and/or low electron mobility (μ_e). In the current study, InN films with very low dislocation densities - as indicated from the low FWHM of the rocking curves (FWHM (002) < 400 $arcsec$ and FWHM (105) $<$ 1000 $arcsec$) - and low surface roughness (< 15 nm), values, which are among the lowest reported up to date via the pulsed-OMVPE growth technique. In addition, these superior structural properties, as compared to the studies presented in Table 5.3, are accompanied with high electron mobilities ($\mu_e > 550$ cm^2/Vs) and relatively low sheet carrier concentration ($n_s < 2$ x 10^{14} cm^{-2}). Hence, a systematic study of InN films with high crystal structure quality, high electron mobilities and low background carrier concentration has bee demonstrated, which will be essential for future devices

employing this material for applications such as LEDs and LASERs.

Scientific work	Rocking curve FWHM $arcsec$	RMS nm	n_s cm^{-2}	μ_e $cm^2/(Vs)$
Jamil et al. [22]	(102)-1800 (002)-1281	31	3.3×10^{14}	681
Fareed et al. [17]	-	42	1.49×10^{14}	98
Kadys et al. [16]	(002)-820	12	1×10^{14}	644
Baijun et al. [18]	(002)-4900	13.2	1.04×10^{14}	67
Mickevicius et al. [15]	(002)-1744	28.3	–	-
Present work	(105) < 1000 (002) < 400	<15	$< 2.0 \times 10^{14}$	>550

Table 5.3: Structural and electrical data of InN films grown on GaN/sapphire via the pulsed-OMVPE. The data represent InN films fabricated under optimal growth conditions with thickness of 150-300 nm.

It has been suggested that high quality InN can be integrated with a conventional InGaN QWs to realize high efficiency long wavelength emitters. More specifically, theoretical, as well as some preliminary studies, have shown that the insertion of an ultra-thin layer of InN (delta-like) in a conventional InGaN-based QW results in a significant shift of the emitted wavelength towards the red spectral regime with a simultaneous enhancement of the spontaneous emission rate [13,29,30]. The theoretical and experimental investigation of this concept is presented and discussed in the following chapter. In addition, it is worth mentioning that the 3-D growth mode of InN can be exploited in order to form InN quantum dots (QD) with various thicknesses through the photoelectrochemical process [31,32]. It is known that this process is initiated in regions with low material quality i.e regions with high dislocation densities and grain boundaries.The the 3-D morphology of the InN thin films will assist to the formation of the InN QDs.

5.4 Summary of Chapter 5

Metallic-In free InN samples with different growth conditions were fabricated via the pulsed-OMVPE technique. It was found that the crystal structure quality of the InN films was degraded with increasing the growth temperature from 460-565 ^{o}C while the presence of point defects, which act as intrinsic donors, was suppressed resulting in low sheet carrier concentration of $n_s \approx 1.6$ x 10^{14} cm^{-2} and high electron mobilities of $\mu_e \approx 570\ cm^2/(Vs)$. Higher V/III molar ratios degraded the crystal structure quality and the surface roughness of the films, while the sheet carrier concentration (n_s) decreased due to suppression of nitrogen vacancies (V_N). The formation of metallic-In was more pronounced for growths with V/III molar ratios < 32000, which significantly affected the structural and electrical characteristics of the InN films. The study of the pulse period and duty cycle showed that no metallic-In was formed under the specific growth conditions. In addition, the lower pulse periods and lower duty cycles assist to the improvement of the surface roughness of the films and to the reduction of sheet carrier concentration (n_s). The current work systematically presents how the various growth parameters governing the InN pulsed-OMVPE growth can be effectively tuned in order to achieve high crystal structure quality (FWHM of (002) $< 400\ arcsec$ and (105) $< 1000\ arcsec$) with high electron mobilities ($\mu_e > 550\ cm^2/Vs$) and low sheet carrier concentrations ($n_s < 2$ x $10^{14}\ cm^{-2}$) which can be useful for future electronic devices employing the InN material system. The electrical properties of the films remain almost unaffected in a wide range of environmental temperatures as it was observed from the Hall dependent measurements.

References

1. Foutz, B.E., O'Leary, S.K., Shur, M.S., Eastman, L.F. Transient electron transport in wurtzite GaN, InN, and AlN. J. Appl. Phys. 85, 7727 (1999).

2. Wu, J., et al. Superior radiation resistance of InGaN alloys: Full solar spectrum photovoltaic material system. J. Appl. Phys., 94, 6477 (2003).

3. Teraguchi, N. & Suzuki, A. Nitride-type III-V HEMT having an InN 2DEG channel layer.US Patent 6,177,685, (2001).

4. Xu, G. eta al. THz Generation from InN Films due to Destructive Interference between Optical Rectification and Photocurrent Surge. Sem. Sci. and Tech., 25 (1), 015004, (2010).

5. Tekcan, B. et al. A Near-Infrared range photodetector based on indium nitride nanocrystals obtained through laser ablation. IEEE Electron. Dev. Lett., 35, 936 (2014).

6. Wu, G.-G. et al. Near infrared electroluminescence from n-InN/p-GaN light-emitting diodes. Appl. Phys. Lett. 100, 103504 (2012).

7. Zhao, Y. et al. Near infrared light-emitting diodes based on n-InN/p-NiO/p-Si heterojunction. J. Lumin. 173, 1 (2016).

8. Andreev, B. A. et al Towards the indium nitride laser: obtaining infrared stimulated emission from planar monocrystalline InN structures. Sci. Rep. 8, 9454 (2018).

9. Johnson, M.C., Konsek, S.L., Zettl, A., & Bourret-Courchesne, E.D. Nucleation and growth of InN thin films using conventional and pulsed MOVPE. J. Cryst. Growth, 272, 400 (2004).

10. Jamil, M., Hongping, Z., John B., H., & Tansu, N. Influence of growth temperature and V/III ratio on the optical characteristics of narrow band gap (0.77 eV) InN grown on GaN/sapphire using pulsed MOVPE. J. Crys. Growth, 310, 4947-4953 (2008).

11. Jamil, M., et al. OMVPE Epitaxy of InN Films on GaN Templates Grown on Sapphire and Silicon (111) Substrates. Physica Stat. Solidi (a), 205 (7), 1619-1624 (2008).

12. Yoshikawa, A. et al. Proposal and achievement of novel structure InN / GaN multiple quantum wells consisting of 1 ML and fractional monolayer InN wells inserted in GaN matrix Appl. Phys. Lett. 90, 073101 (2007).

13. Zhao, H., Liu, G. & Tansu, N. Analysis of InGaN-delta-InN quantum wells for light-emitting diodes. Appl. Phys. Lett. 97, 131114 (2010).

14. Woods, V., Dietz, N. InN growth by high-pressures chemical vapor deposition: Real-time optical growth characterization. Mater. Sci. Eng. B, 127, 239 (2006).

15. Mickevicius, J. et al. Engineering of InN epilayers by repeated deposition of ultrathin layers in pulsed OMVPE growth. Appl. Surf. Sci. 427, 1027–1032, (2018).

16. Kadys, A. et al. Growth of InN and In-rich InGaN layers on GaN templates by pulsed metalorganic chemical vapor deposition. J. of Elec. Mat., 44, 1, (2015).

17. Qhalid Fareed, R.S., et al. High quality InN/GaN heterostructures grown by migration enhanced metalorganic chemical vapor deposition. Appl. Phys. Lett., 84, 1892 (2004).

18. Baijun, Z., Xu, H., Fan, Y., Xin D. & Yuantao, Z. Studies on Growth of N-Polar InN films by pulsed metal-organic vapor phase epitaxy. Chem. Res. Chin. Univ., 32(4), 669—673, (2016).

19. Heying, B., et al. Role of threading dislocation structure on the x-ray diffraction peak widths in epitaxial GaN films. Appl. Phys. Lett. 68, 643 (1996).

20. Yamaguchi, S. et. al. Structural properties of InN on GaN grown by metalorganic vapor-phase epitaxy. J. Appl. Phys. 85, 7682 (1999).

21. Chierchia, R. et al. Microstructure of heteroepitaxial GaN revealed by x-ray diffraction. J. of Appl. Phys. 93, 8918 (2003).

22. Jamil, M., Zhao, H., Higgins, J. B. & Tansu, N. MOVPE and photoluminescence of narrow band gap (0.77 eV) InN on GaN/sapphire by pulsed growth mode. phys. stat. sol. (a) 205, 12, 2886–2891 (2008).

23. Wu, J. et al. Unusual properties of the fundamental band gap of InN. Appl. Phys. Lett., 80, 3967 (2002).

24. Piper, L. F. J., Veal, T. D., McConville, C. F., Lu, H., & Schaff, W. Origin of the n-type conductivity of InN: The role of positively charged dislocations. J. Appl. Phys. Lett. 88, 252109 (2006).

25. Limpijumnong, S., & Van de Walle, C. G. Passivation and Doping due to Hydrogen in III-Nitrides. Phys. Status Solidi B, 303 (2001).

26. Look, D.C., Lu, H., Schaff, W. J., Jasinski, J., & Liliental–Weber, Z. Donor and acceptor concentrations in degenerate InN. Appl. Phys. Lett., 80, 258 (2002).

27. Stampfl, C., Van de Walle, C. G., Vogel, D., Kruger, P., & Pollmann, J. Native defects and impurities in InN: First-principles studies using the local-density approximation and self-interaction and relaxation-corrected pseudopotentials.

28. Janotti, A. & Van de Walle, C. G. Sources of unintentional conductivity in InN. Appl. Phys. Lett. 92, 032104 (2008).

29. Fragkos, I.E. et al. Pulsed OMVPE growth studies of InN for integration in InGaN active region. Proceeding of ACCGE-21/OMVPE-18. III/V Nitride and Other WBG Semicondutors, Santa Fe, NM, USA 2017

30. Fragkos, I.E. et al. Experimental studies of delta-InN incorporation in InGaN quantum well for long wavelength emission. Proceeding of IEEE Phot. Conf. WH3 / Phosphors and Long Wavelength GaN Materials, Reston, VA USA 2018

31. Xiao, X. et al. Quantum-size-controlled photoelectrochemical fabrication of epitaxial InGaN quantum dots. Nano Lett., 14 (10), 5616–5620, (2014).

32. Wei, X. et al. Room temperature luminescence of InGaN quantum dots formed by quantum-sized-controlled photoelectrochemical etching. Appl. Phys. Lett., 113, 121106 (2018).

Chapter 6

III-Nitride based QWs for long wavelength emission

6.1 InGaN delta-InN based QW for long wavelength emission

In recent years, the pursuit of high efficiency InGaN based quantum well (QW) light emitters towards red spectral regime has been proven to be challenging. The need for higher In-content in the InGaN active region for longer wavelength emission, results in phase separation of the InGaN alloy, defect formation due to lattice mismatch with the u-GaN substrates, and higher polarization fields which reduce the wavefunction overlap between electrons and holes inside the QW. These factors are detrimental for the internal quantum efficiency (IQE) of the emitter and have resulted to the well-known "green-gap" problem [1-5]. The challenges for high In-content in the InGaN active region, have hindered the development of relatively high efficiency visible light emitters - without the need of phosphor down conversion - that could exploit a full color gamut and enable LED devices for solid state lighting and display applications [6].

Several theoretical and experimental approaches have been proposed to overcome these issues including, staggered InGaN QWs, strain compensated InGaN QWs, semipolar and non-polar InGaN QWs, ternary substrates and buffer layers, and high bandgap thin interlayers embedded in the InGaN QWs. Recently, special research interest has been given for the later one, since the use of AlGaN and AInN interlayers has resulted in InGaN QWs with the highest efficiencies in the red and green spectral regime [7-23]. In addition to the above solutions, a different approach which eliminates the need for high In-content has been proposed. In particular, theoretical studies have shown that by varying the thickness of an inserted ultra-thin layer (delta-like) of InN ($\approx 6\ nm$) in the middle of a conventional 3.0 nm $In_{0.25}Ga_{0.75}N$ QW with GaN barriers results in a significant wavelength shift towards the red spectral regime ($\approx 740\ nm$) with enhanced wavefunction overlap ($\Gamma_{e-h} \approx 50\%$) [24].

The work presented in this thesis exploits the concept of the δ-InN layer in combination with a thin AlGaN interlayer (IL) integrated into a conventional InGaN QW with GaN barriers (δ-structure) to achieve high efficiency long wavelength emitters. This new δ-structure is depicted in figure 6.1, is different form the one presented in reference [24], since it consists of a δ-InN layer placed on top of a conventional InGaN QW – rather than in the middle – followed by the AlGaN IL. Numerical simulations were carried out based on a six-band $k.p$ formalism for wurtzite semiconductor which took into account the strain effect, valence band mixing, polarization fields, and the carrier screening effect [9]. The energy band structure, wavefunction overlap and spontaneous emission rates were calculated for the δ-structure and were compared to a reference structure. The reference structure consists of an InGaN QW, AlGaN IL and GaN barriers with the same layer thicknesses and compositions as the δ-structure.

This new design enables experimental verification via the OMVPE growth technique since the use of the AlGaN IL circumvents the issue of the δ-InN evaporation/decomposition during the high temperature GaN barrier growth. More specifi-

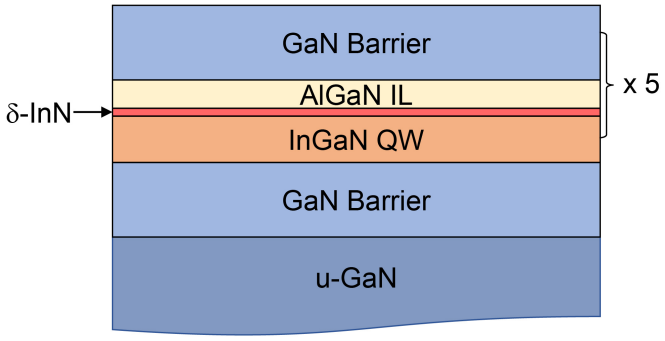

Figure 6.1: Novel active region design consisted of InGaN QW + δ-InN + AlGaN interlayer between GaN barriers.

cally, the large discrepancy on the optimized growth temperatures between the InN ($< 600\ ^{o}C$), InGaN ($\approx 700\ ^{o}C$) and GaN ($\approx 850\ ^{o}C$) materials would result in the decomposition/out-diffusion of InN during the growth of the GaN barrier growth [25,26], thus creating a challenge for the integration of this new active region design. However, this challenge can be addressed by growing an AlGaN interlayer at the same temperature as the InN ($< 600\ ^{o}C$) in order to "cap" the indium during the high temperature growth of the GaN barrier [25,26]. The concept of the AlGaN IL has been demonstrated in the case of the conventional InGaN QWs. In addition, the AlGaN IL is beneficial for high temperature GaN barrier growth with a concurrent thermal annealing of the beneath layers [19]. Moreover, despite the low growth temperature of the AlGaN IL, the material quality is expected to be moderate due to the low adatom mobility of the Al precursors. However, during the high temperature GaN barrier growth, the thermal annealing that occurs in the AlGaN IL is expected to improve its crystal quality overall [19].

Following the numerical simulations, proof-of-concept experiments were carried out via the OMVPE technique to demonstrate the properties of the δ-structure in comparison with the reference structure.

6.2 Numerical simulations

Figure 6.2 (a) and 6.2 (b) depict the band structure of the reference and the δ-structures respectively. The reference structure is consisted of a 2.6 nm $In_{0.2}Ga_{0.8}N$ QW with 1 nm $Al_{0.4}Ga_{0.6}N$ IL and 5 nm GaN barriers while the δ-structure has a 0.6 nm δ-InN layer inserted between the $In_{0.2}Ga_{0.8}N$ QW and $Al_{0.4}Ga_{0.6}N$ IL. The reference structure is characterized by a transition (emitted) wavelength of $\lambda = 437$ nm which is the blue spectral regime with an electron-hole (e-h) wavefunction overlap of $\Gamma_{e-h} = 43\%$. According to the concept of the δ-InN layer, as presented in reference [24], the introduction of a very thin layer of a much lower bad gap material should decrease the energy transition levels both in the condition band and valence band of the quantum well, shifting the emitting wavelength towards the red spectral regime. As it is shown in figure 6.2 (b), the insertion of the δ-InN layer redshifts the transition wavelength from 437 nm to 634 nm (red spectral regime) but at the expense of the e-h wavefunction overlap Γ_{e-h} , which is dramatically reduced to 3% as compared to the reference structure.

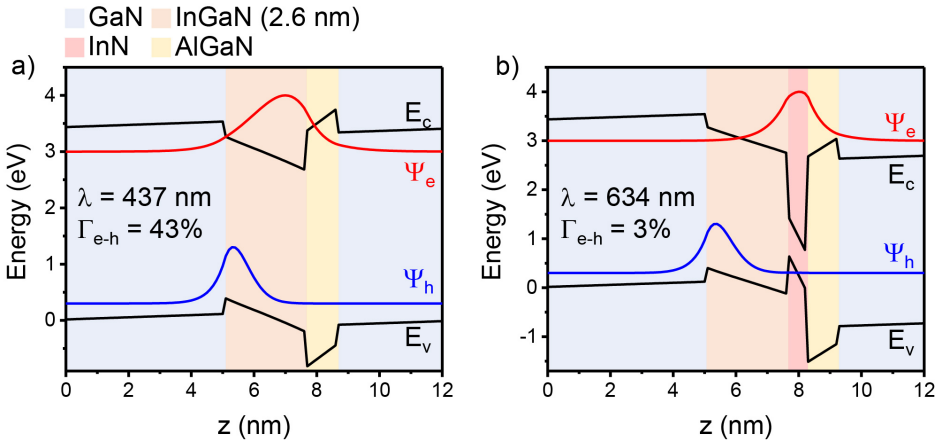

Figure 6.2: Numerical simulations of bandstructure and e/h wavefunction profile of a) reference structure consisted of 2.6 nm $In_{0.2}Ga_{0.8}N$ QW + 5 monolayers $Al_{0.4}Ga_{0.6}N$ interlayer between 5 nm GaN barriers, and b) δ-structure consisted of of 2.6 nm $In_{0.2}Ga_{0.8}N$ QW + 3 monolayers (0.6 nm) δ-InN + 5 monolayers $Al_{0.4}Ga_{0.6}N$ interlayer between 5 nm GaN barriers.

It is important to mention that the thickness of the inserted δ-InN layer is 0.6 nm which corresponds to a few monolayers (≈ 3) of InN. For such low thickness, the δ-InN can not act a quantum well i.e there are no confined states within this layer. All of the confined states are located in the InGaN QW layer. The main reason of the low e-h wavefunction overlap of the δ-structure is the location of the holes in the valence band. In particularly, as it can be seen in figure 6.2 (a), the peak of the hole wavefunction (Ψ_h) of the reference structure is located at the interface of the InGaN layer with the left GaN barrier and its position does not change with the insertion of the δ-InN layer in the δ-structure (figure 6.2 (b)) as opposed to the peak of the electron wavefunction Ψ_e. For the later one, the peak of Ψ_e moves into the δ-InN layer of the δ-structure.

In order to increase the e-h wavefunction overlap in the δ-structure, the peak of the Ψ_h has to be shifted towards the δ-InN layer. A simple way to accomplish this, is to reduce the thickness of the InGaN layer. Figure 6.3 (b) presents the case where the InGaN layer is reduced to 2.0 nm. By doing so the peak of the hole wavefunction is shifted into the δ-InN layer, dramatically increasing the e-h wavefunction overlap Γ_{e-h} to 86% with an emitted wavelength $\lambda = 615\ nm$. Figure 6.3 (a) corresponds to a reference structure with a 2 nm $In_{0.2}Ga_{0.8}N$ layer.

It is obvious that the δ-InN layer itself does not help to achieve large e-h wavefunction overlap in this particular novel active region design. The thickness of the InGaN layer is very crucial. In general for thin InGaN layers $< 2\ nm$ with few monolayers of δ-InN and an AlGaN IL, the δ-structures will result in very high wavefunction overlap with a simultaneous wavelength shift towards the red spectral regime as compared to the reference structure without the δ-InN layer.

In addition to the wavelength shift and the high e-h wavefunction overlap, the δ-InN structure can exhibit very high carrier injection efficiencies if the active region is implemented for LEDs. The high bandgap material of the AlGaN IL can act as

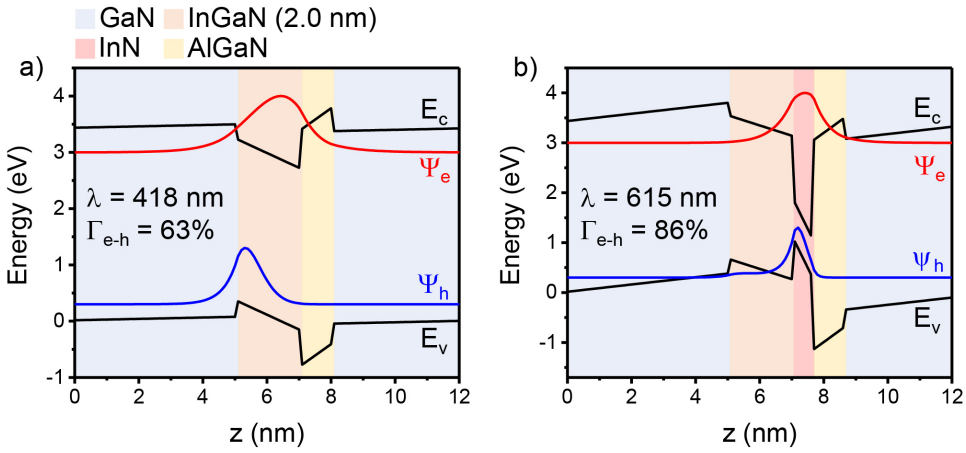

Figure 6.3: Numerical simulations of bandstructure and e/h wavefunction profile of a) reference structure consisted of 2.0 nm $In_{0.2}Ga_{0.8}N$ QW + 5 monolayers $Al_{0.4}Ga_{0.6}N$ interlayer between 5 nm GaN barriers, and b) δ-structure consisted of of 2.0 nm $In_{0.2}Ga_{0.8}N$ QW + 3 monolayers (0.6 nm) δ-InN + 5 monolayers $Al_{0.4}Ga_{0.6}N$ interlayer between 5 nm GaN barriers.

an effective barrier for the injected electrons and holes into the active region, by preventing them from the thermionic escape from the quantum well [27]. It is very common that in conventional InGaN QW based LEDs, as the injected current is increased over some range, there is an observed blue-shift of the emitted photon energy. This blue-shift in general is attributed 1) in the band-filling effect of localized energy states formed by potential profile fluctuations (due to In composition fluctuations) and 2) to the carrier screening of the strain-induced polarization fields (those fields are responsible for the quantum confined stark effect (QCSE)· the carrier screening of the QCSE flattens the potential across the MQWs increasing the quantum energy states into the QW).

For the case of the δ-structure, the QCSE is expected to be strong enough (due to the large lattice mismatch among the δ-InN and AlGaN IL) so that the presence of the carries will not be able to screen it. This will result in minimum blue-shift of the emitted wavelength of the spontaneous emission spectrum (assuming that there is not In-composition fluctuation into the active region of the δ-structure). This can be seen in figure 6.4 where the peak of the spontaneous emission spectrum of the

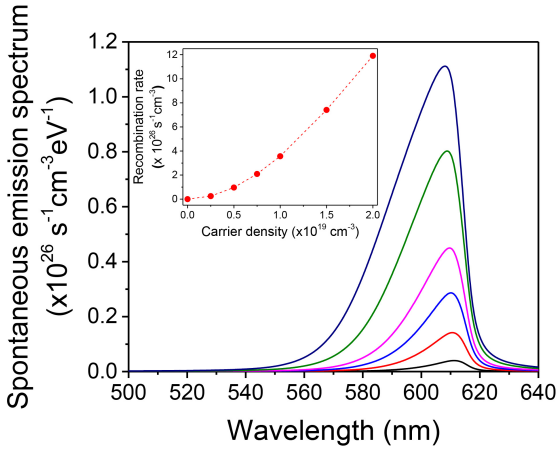

Figure 6.4: Spontaneous emission spectra and radiative recombination rate of a δ-structure consisted of of 2.0 nm $In_{0.2}Ga_{0.8}N$ QW + 3 monolayers (0.6 nm) δ-InN + 5 monolayers $Al_{0.4}Ga_{0.6}N$ interlayer between 5 nm GaN barriers.

δ-structure increases from 0.04×10^{26} to 1.12×10^{26} $s^{-1}cm^{-3}eV^{-1}$ while the carrier density n increases form 2.5×10^{18} to 2×10^{19} cm^{-3} respectively, with no observed blue-shift on the transition wavelength.

6.3 Proof-of-concept experiments

The numerical simulations so far have indicated the δ-structure with a relatively thin InGaN QW and an AlGaN IL can be used as a highly efficient light emitter in the visible spectral regime without the need of high In-content in the active region. Proof-of concept experiments are carried out in order to demonstrate the concept of the δ-structure presented in this thesis. The proof-of-concept experiments were done according to the flow of the simulations and are divided into two parts: in the first part the δ-structure was studied for a ≈ 3 nm $In_{0.15}Ga_{0.85}N$ QW with ≈ 1 nm $Al_{0.4}Ga_{0.6}N$ IL and for the second part the δ-structure was studied for a ≈ 2 nm $In_{0.17}Ga_{0.83}N$ with a QW ≈ 1 nm $Al_{0.35}Ga_{0.65}N$ IL. The composition of the InGaN layers among the two experimental parts varied slightly, but this does not significantly alter the concept of the wavelength shift and e-h wavefunction overlap changes of the

δ-structures with respect to their reference structures.

As described in introduction part, the new design of the δ-structure, enables the experimental verification via the OMVPE technique. However, an issue that needs to be taken under consideration is the growth of pure InN δ-layer, without the presence of metallic-In. It is well known that the OMVPE growth of InN imposes a very narrow-optimized growth conditions which are limited by the ammonia (NH3) dissociation and metallic-In formation. Nevertheless, this issue can be overcome by employing a pulsed-OMVPE growth mode for the InN layer, which results in high quality metallic-In free InN films.

The structures investigated in this study are depicted in figure 6.1. The epitaxy of the structures was done in a vertical-flow shower-head type Veeco-P75 reactor under a growth pressure of 200 $Torr$. Ammonia was used as the group-V precursor while triethylgallium (TEGa), trimethylindium (TMIn), and trimethylaluminium (TMAl) were used as group-III precursors for the III-nitride layers. Five periods consisted of InGaN/ δ-InN / AlGaN / GaN were grown on top of a 3 nm thick n-doped GaN (3×10^{16} cm^{-3}) templates on patterned c-plane sapphire substrate. The growth profile of the structure is depicted in figure 6.5. The InGaN layers were grown at $\approx$ 730 ^{o}C while the GaN barriers at $\approx$ 860 ^{o}C. To accommodate the growth of the InN at $\approx$ 560 ^{o}C, the pulsed-OMVPE growth was employed. During the growth of the InN δ-layer, the NH3 was constantly running into the reactor while the TMIn precursor was pulsed. Following the growth of the δ-InN layer, the AlGaN layer was grown via the normal-OMVPE growth mode at the same temperature of $\approx$ 560 ^{o}C.

To study the effect of the δ-InN, a second structure without the δ-InN layer was grown under the same growth temperature profile depicted in figure 6.5. Both MQW structures consisted of a $\approx$ 3 nm $In_{0.15}Ga_{0.85}N$ QW, $\approx$ 5 monolayers ($\approx$ 1 nm) of $Al_{0.4}Ga_{0.6}N$ IL and $\approx$ 10 nm GaN barriers. For the structure with the δ-InN layer, the growth conditions of the pulsed-OMVPE growth mode were optimized in

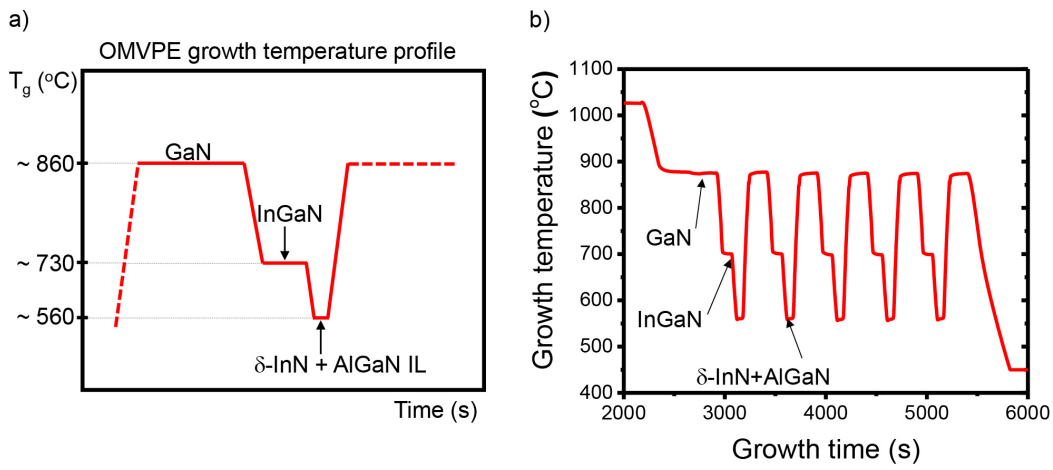

Figure 6.5: a) OMVPE growth temperature profile of 1 period of a δ-structure. b) Actual growth temperature profile of a 5 period δ-structure. The reference structures exhibit similar growth temperature profile.

order to achieve metallic-In free δ-InN layer with nominal thickness of $\approx 0.6\ nm$ [25-26]. This thickness of the δ-InN layer corresponds to ≈ 2 monolayers ($\approx 0.6\ nm$) which is the optimum thickness for fully strained InN layer. The two structures were characterized by using a coupled $\omega/2\theta$ scan in the (002) - growth direction - via a X-ray diffractometer. As it can be seen from figure 6.6 (a), both structures exhibit sharp diffraction peaks which is an indication that the crystallinity of the MQWs is maintained, despite the low growth temperature of AlGaN IL and the introduction of the δ-InN layer. We believe that the high growth temperature of the GaN barriers assists to the re-crystallization of the δ-InN + AlGaN IL which in turns improve the overall crystal quality of the structure. It is also important to notice that despite the introduction of the δ-InN layer, the picture of the coupled $\omega/2\theta$ scan for the δ-structure does not significantly change. One would expect smaller fringes between the satellite pics for the MQW δ-structure. However, the very thin layer of the δ-InN in combination with the low resolution of the XRD diffractometer cannot detect its presence. Any detected signal would be buried into the noise between the adjacent picks of the MQW δ-structure.

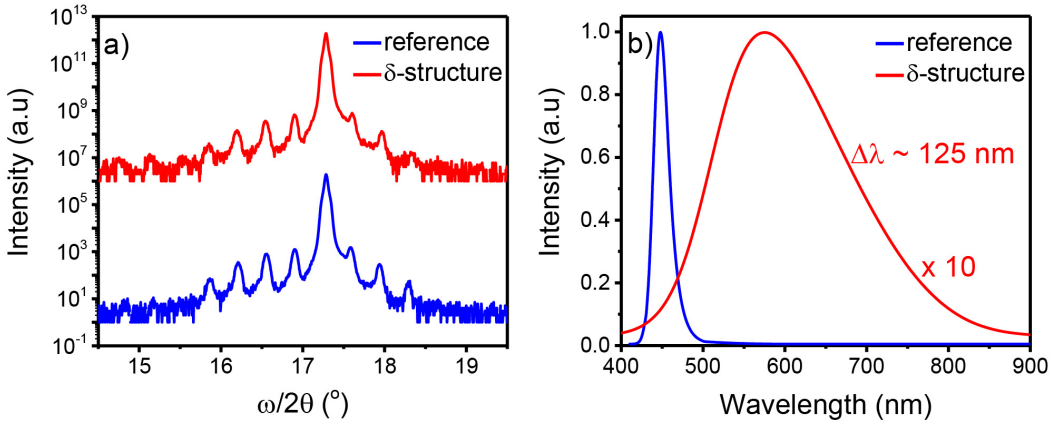

Figure 6.6: a) (002) plane $\omega/2\theta$ XRD scans, and b) Photoluminescence spectra of the reference and δ-structure with a 3 nm InGaN layer.

The PL spectra of both structures is depicted in figure 6.6 (b). A source of a 405 nm laser with a 95 mW power was used as the excitation source. The reference structure has a sharp luminescence with a peak wavelength of λ=448 nm. With the insertion of the δ-InN layer, the δ-structure exhibits a very low luminescence with a peak wavelength of λ=571 nm. Notice: In order to see the signal, the integration time of the digital spectrophotometer had to be increased by 10 times to that of the reference structure. Although the emitted wavelength has shifted towards the yellow region of the spectrum, the PL signal arising from this δ-structure is most probably associated with the yellow band luminescence of the GaN substrate. In addition, considering fact that the δ-structure maintains relatively good crystal quality, according to the XRD spectrum, the very low luminescence could not be due to bad crystal quality. The reason for the low luminescence is most probably associated with poor e-h wavefunction overlap as predicted from the numerical simulations.

Following the order of the numerical simulations, the second part of the proof-of-concept experiments consists of a reference and δ-structures of $\approx$ 2 nm $In_{0.17}Ga_{0.83}N$ QW, $\approx$ 1 nm $Al_{0.35}Ga_{0.65}N$ IL and $\approx$ 10 nm GaN barrier while the δ-InN in the δ-structure is $\approx$ nm. Figure 6.7 (a) depicts the $\omega/2\theta$ scan of both structures. Sharp

satellite peaks are observed which is an indication of the good crystal quality of the structures. Both structures were excited with a 405 nm laser at 95 mW power. The PL signal is depicted in figure 6.7 (b). It can be seen that after the thickness of the InGaN layer is reduced to $\approx$ 2 nm, the luminescence of the δ-structure has been increased approximately from 40000 to 49000 (1.22 times) - the plots have been normalized to the maximum peak of the δ-structure) and the peak wavelength has been slightly increased from 450 nm to 475 nm with respect to the reference structure. This result is consistent with the numerical calculations: for a 2 nm InGaN layer, the reference structure exhibits an e-h wavefunction overlap $\Gamma_{e-h} \approx 63\%$ while the δ-structure has $\Gamma_{e-h} \approx 83\%$ (1.36 times) with a simultaneous increase of the transition wavelength. Despite the fact that only the PL enhancement is observed here, which is $\approx$ 1.3 times of that of the reference structure, the shift of the emitted wavelength is very small $\approx$ 25 nm.

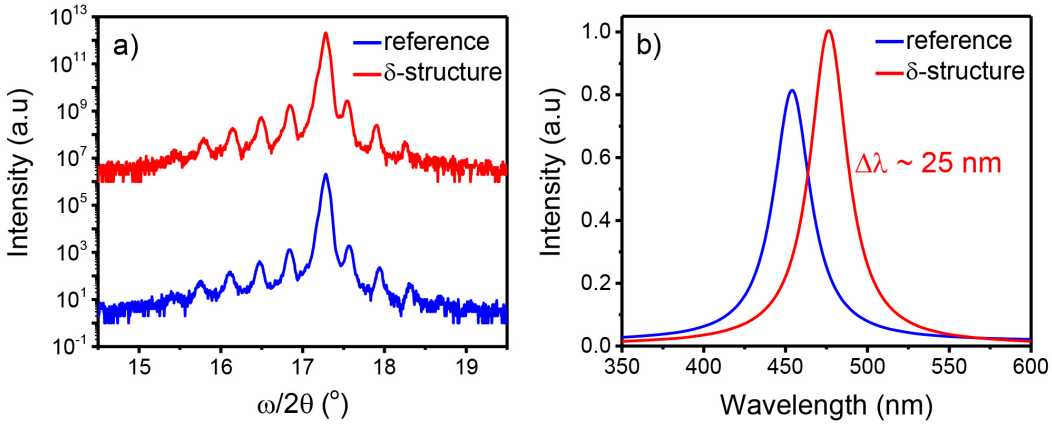

Figure 6.7: a) (002) plane $\omega/2\theta$ XRD scans, and b) Photoluminescence spectra of the reference and δ-structure with a 2 nm InGaN layer.

These results indicate that the reduction of the thickness of the InGaN layer and the insertion of the δ-InN layer, indeed help to improve the radiative efficiency of the emitter and also shift the emitted wavelength as opposed to the structure with thicker InGaN layer where the insertion of the the δ-InN layer completely killed the photolu-

minescence. However, it is important to mention that the experimental structures are not ideal i.e they do not exhibit abrupt hetero-interfaces, neither coherently strained and uniform layers as it is assumed for the numerical calculations. The above factors will certainly introduced unwanted crystal defects during the growth of the structures which will impact their properties. This is the reason of the observed discrepancy in the absolute values of the wavelength shift between the simulation and the experiment. Further improving the OMVPE process or even switching to molecular beam epitaxy (MBE), where the uniformity of the layers and strain control are better control, will dramatically improved the properties of the δ-structures. Nevertheless, the numerical calculations and the simulations in general should serve as a guidance of the experimental design. The experimental trends are consistent with the trends of the numerical calculations presented in this thesis.

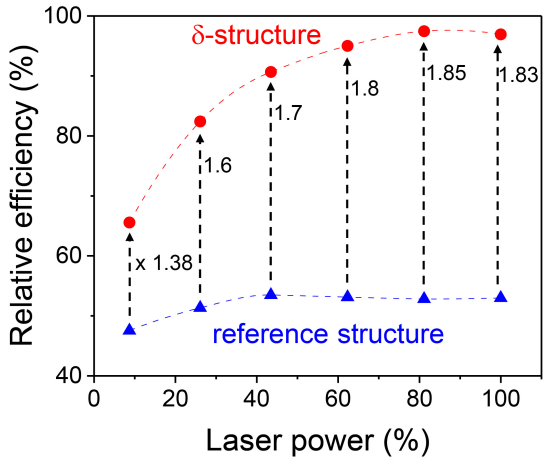

Figure 6.8: Relative efficiencies under different excitation powers with a 405 nm laser for the reference and δ-structure with 2 nm InGaN layer.

Figure 6.8 depicts a relative efficiency of the δ-structure with respect to the reference structure for the case of a 2 nm InGaN layer. The relative efficiency is defined as the integral of the PL spectra in the ranged of 350 nm - 550 nm over the relative output power of the laser (maximum output power of 350 mW). The δ-structure exhibits almost 1.85 times higher efficiency than the reference structure. This is an

indication that the insertion of the δ-InN layer enhanced at some degree the wavefunction overlap improving in that way the internal quantum efficiency of the emitter (assuming that the two structures have identical defect concentration).

6.4 Summary of Chapter 6

In summary, a novel active region design of GaN/InGaN/δ-InN/AlGaN/GaN has been proposed in order to achieve high efficiency visible light emitters without the need for high In content in the active region. This new design enables experimental demonstration via the OMVPE technique because it helps to overcome the issue of the δ-InN evaporation/decomposition during the growth of the structure. In particular, the growth of the thin AlGaN interlayer following the growth of the δ-InN layer at the same temperature, prevents the evaporation/decomposition/out-diffusion of the InN during the high temperature GaN barrier growth. In addition, the high temperature GaN barrier growth assists to the annealing of the layers and improves the overall quality of the structure. The experimental trends are consistent with the numerical calculations which they showed that a) a δ-structure with relatively thick InGaN layer reduces the e-h wavefunction overlap and kills the efficiency of the emitter as compared to the reference structure, and b) a δ-structure with a relatively thin InGaN layer provides a wavelength shift towards red spectral regime and high efficiencies as compared to the the reference structure.

References

1. Belyaev, K. G. et al. Phase separation in $In_xGa_{1-x}N$ (0.10 < x < 0.40). Phys. Status Solidi C 10, 527-531 (2013).

2. McCluskey, M. D. et al. Phase separation in InGaN multiple quantum wells. Appl. Phys. Lett. 72, 1730–1732 (1998).

3. Takeuchi, T. et al. Quantum-confined stark efect due to piezoelectric felds in GaInN strained quantum wells. Jap. J. Appl. Phys. 36(Part 2), Number 4A (1997).

4. Damilano, B. & Gil, B. Yellow–red emission from (Ga,In)N heterostructures. J. Phys. D: Appl. Phys. 48, 403001 (2015).

5. Xu, G. et al. Investigation of Large Stark Shifs in InGaN/GaN Multiple Quantum Wells. J. Appl. Phys. 113, 033104 (2013).

6. Tsao, J. Y. et al. Toward smart and ultra-efcient solid-state lighting. Adv. Optical Mater. 2, 809–836 (2014).

7. Zhao, H. P. et al. Approaches for high internal quantum efciency green InGaN light-emitting diodes with large overlap quantum wells. Optics Express 19, A991–A1007 (2011).

8. Zhao, H. P. Growths of staggered InGaN quantum wells light-emitting diodes emitting at 520-525 nm employing graded growthtemperature profle. Appl. Phys. Lett. 95, 061104 (2009).

9. Zhao, H. P., Arif, R. A., Ee, Y. K. & Tansu, N. Self-consistent analysis of strain-compensated InGaN-AlGaN quantum wells for lasers and light emitting diodes. IEEE J. Quantum Electron. 45, 66–78 (2009).

10. Zhang, J. & Tansu, N. Improvement in spontaneous emission rates for InGaN quantum wells on ternary InGaN substrate for lightemitting, diodes. J. Appl. Phys. 110, 113110 (2011).

11. Daubler, J. et al. Long wavelength emitting GaInN quantum wells on metamorphic GaInN bufer layers with enlarged in-plane lattice parameter. Appl. Phys. Lett. 105, 111111 (2014).

12. Ohkawa, K., Watanabe, T., Sakamoto, M., Hirako, A. & Deura, M. 740-nm emission from InGaN based LEDs on c-plane sapphire substrates by MOVPE. J. Crys. Growth 343, 13–16 (2012).

13. Hwang, J., Hashimoto, R., Saito, S. & Nunoue, S. Development of InGaN-based red LED grown on (0001) polar surface. Appl. Phys. Express 7, 071003 (2014).

14. Kawaguchi, Y. et al. Semipolar (2021) single-quantum-well red light-emitting diodes with a low forward voltage. Jap. J. Appl. Phys. 52, 08JC08 (2013).

15. Hashimoto, R. et al. High-efficiency yellow light-emitting diodes grown on sapphire (0001) substrates. Phys. Status Solidi C 11, No. 3–4, 628–631 (2014).

16. Hashimoto, R. et al. High-efficiency green-yellow light-emitting diodes grown on sapphire (0001) substrates P hys. Status Solidi C 10, No. 11, 1529–1532 (2013).

17. Saito, S. et al. InGaN Light-Emitting Diodes on c-Face Sapphire Substrates in Green Gap Spectral Range. Applied Physics Express 6 (2013) 111004

18. Shioda, T. et al.Enhanced light output power of green LEDs employing AlGaN interlayer in InGaN/GaN MQW structure on sapphire (0001) substrate. Phys. Status Solidi A 209, No. 3, 473–476 (2012).

19. Koleske, D.D. et al. On the increased efficiency in InGaN-based multiple quantum wells emitting at 530–590 nm with AlGaN interlayers. Journal of Crystal Growth. 415 57–64 (2015).

20. Li, P. et al. Highly efficient InGaN green mini-size flipchip light-emitting diodes with AlGaN insertion layer Nanotechnology. 30 095203 (2019).

21. Hussain, S. et al. Capping green emitting (Ga,In)N quantum wells with (Al,Ga)N : impact on structural and optical properties Semicond. Sci. Technol. 29 035016 (2014).

22. Muyeed, S.A.A. et al. Strain compensation in InGaN-based multiple quantum wells using AlGaN interlayers. AIP Advances, 7, 105312, (2017).

23. Sun, W. et al. Integrating AlInN Interlayers into InGaN/GaN Multiple Quantum Wells for Enhanced Green Emission. Appl. Phys. Let., 112, 201106, (2018).

24. Zhao, et al. N. Analysis of InGaN-delta-InN quantum wells for light-emitting diodes. Appl. Phys. Lett. 97, 131114 (2010).

25. Fragkos, I.E et al. Pulse MOVPE Growth studies of InN and its Integration into InGaN QW for Long Wavelength Emission. IEEE International Photonics Conference, Reston, VA, USA (2018)

26. Fragkos, I.E et al. Experimental Studies of Delta-InN Incorporation in InGaN Quantum Well for Long Wavelength Emission. ICMOVPE XIX, Osaka, Japan (2018).

27. Zhao, H. et al. Analysis of internal quantum efciency and current injection efficiency in nitride light-emitting diodes. J. Disp. Technol. 9, 212-225 (2013).

Chapter 7

Future outlook

7.1 Summary and future outlook of GaN:Eu based work

In this thesis the internal quantum efficiency of the GaN:Eu based emitters was studied. In particular a current injection efficiency model was developed both for optically-pumped and electrically-driven GaN:Eu based devices. Through this model the efficiency discrepancy observed between the optically-pumped and electrically-driven GaN:Eu based devices was clarified. The current injection into the Eu^{+3} ions was studied at the basis of different carriers mechanism that take place along the excitation path of the Eu^{+3} ion. It was shown that the absence of transport phenomena in the optically case resulted in a magnitude higher current injection efficiencies and consequently higher internal quantum efficiencies in the optically-pumped GaN:Eu emitter as compared to the electrically-injected GaN:Eu emitter. This is an indication that the efficiency of this type of emitter is greatly affected by the GaN crystal host as well as from the formation trasport and quantum mechanical phenomena arising form the formation of a $Al_xGa_{1-x}N/GaN : Eu/Al_xGa_{1-x}N$ hetero/homojunction.

It was identified that the droop in the external quantum efficiency of the GaN:Eu

based emitters arises from the saturation of the Eu ions with increasing the photon flux or the current density. The saturation rate of the Eu^{+3} ions depends on the different parameters along their excitation path. In particular, several carriers mechanisms were identified to limit the current injection efficiency at low photon fluxes and current densities. Those mechanisms are related to the GaN host crystal quality, transport/quantum mechanical phenomena arising from the formation of GaN:Eu/AlGaN hetero/homojunctions, as well as, to the traps which are close to the vicinity of the Eu^{+3} ions. At high photon fluxes and current densities the current injection efficiency is limited by the radiative lifetime of the Eu^{+3} ion. The reduction of this time is essential for achieving high efficiencies at the the higher photon flux and current density regime. The realization of high efficiency GaN:Eu emitter will enable their use in micro-LED applications and other solid state lighting applications.

The use of surface plasmon polariton is essential to achieve a reduction of the radiative lifetime of the Eu^{+3} ion. The theoretical calculations has shown that the use of TiN is a promising candidate to achieve thin. Preliminary studies have been carried out to demonstrate the effect of the TiN on the internal quantum efficiency of the GaN:Eu emitter. For these studies TiN was sputtered on top of GaN/GaN:Eu/sapphire substrate. The sapphire was double polished to allow the excitation and PL measurements of the sample from the back. The excitation source was a 325 nm laser.

Figure 7.1 depicts the photoluminescence from the back of sapphire of an 100 nm GaN:Eu with 4 nm and 1 nm GaN spacer with 30 nm sputtered TiN. An non-coated sample was used as a reference (both samples of Gan:Eu with different GaN spacer thickness exhibit similar values of photoluminescence). It can be seen that the peak of the PL at 621 nm was reduced by approximately 46% and 78% for the sample with 4 nm and 1 nm GaN spacer respectively.

This might be an indication that effective coupling between the surface plasmon

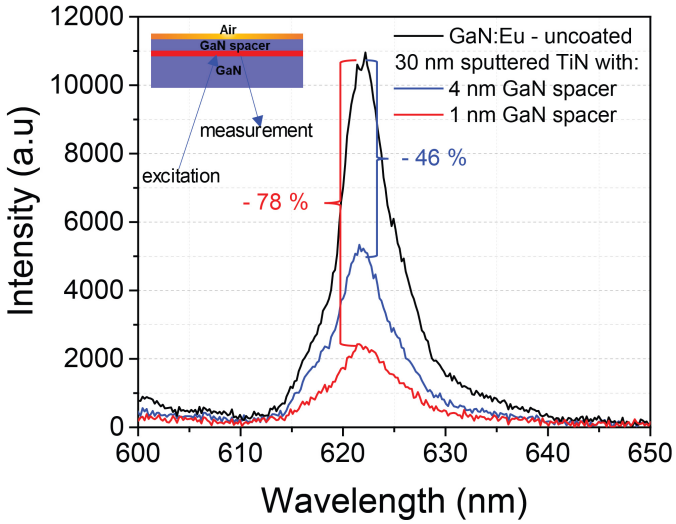

Figure 7.1: Photoluminescence measurements from a 100 nm GaN:Eu sample with a 10 nm GaN spacer and 33 nm sputtered TiN layer. A reference sample without TiN coating is used for comparison. A 325 nm laser was used as the excitation source and the samples were excited form the back.

and the electromagnetic wave emitted from the Eu^{+3} ions is established. However, the SPP cannot be decoupled, probably due to non sufficient scattering mechanisms at the interface of the TiN and the GaN spacer. According to the simulation, although TiN is suitable, the wavevectors of surface plamson polariton are relatively large, which means that the SPP needs to be scattered in order to be de-coupled and radiate. This decoupling could be achieved via the surface roughening of the GaN spacer or even by fabricating surface Bragg gratings that would match the wavevector of the surface plamson polariton.

It is also important to mention that part of the reflected laser beam from the Air/TiN/GaN interface will also contribute to the excitation of the GaN:Eu region (during the second pass from the GaN:Eu region). Numerical calculations have shown that the percentage of reflection of the 325 nm laser from such interfaces it is in the order 20% for the Air/GaN interface (uncoated sample) and 28% for the Air/TiN/GaN interface (30 nm TiN coated samples). This reduction should be similar for both GaN:Eu samples with different spacer thickness. Hence, the amount of available

photons that excite the GaN:Eu samples are lower from the case of the uncoated sample. Therefore, part of the PL reduction of the TiN coated samples might also be attributed to the less available photons for the excitation of the GaN:Eu active region.

7.2 Summary and future outlook of δ-InN/InGaN QW based work

An alternative active region design based on the integration of a δ-InN into an InGaN QW + AlGaN interlayer active region was studied. This structure enables light emission into the visible spectral regime with high quantum efficiencies. However, to fully take advantage of this structure, the InGaN layer has to be carefully designed in order to provide high e-h wavefunction overlap and hence high quantum efficiencies

For the experimental study of this structure, δ-InN layer was grown by pulsed-OMVPE technique to ensure metallic-free δ-InN layer. The growth of the AlGaN interlayer is essential for preventing the out-diffusion/evaporation of the δ-InN during the high temperature growth of the GaN barrier. The experiential results are consistent with the numerical studies. A δ-structure with thinner InGaN layer of approximately 2 nm is beneficial for much stronger luminescence as compared to a δ-structure with thicker InGaN layer. In addition, the δ-structure with thin InGaN layer exhibited 1.85 times higher efficiencies as compared to the reference structure without the δ-InN layer. However, the OMVPE growth of this structure is still challenging. Challenges associate with the δ-InN uniformity, as well as, the optimization of the AlGaN interlayer at low growth temperatures need to be resolved in order to further improved the device performance.

Nevertheless, the results are of this study are promising for the realization of the novel δ-structure as an effective and efficient visible light emitter. Further future

studies would be needed to improve and optimize the growth conditions of such structure that would enable its implementation as an effective and efficient visible light emitter.

Curriculum Vitae

Ioannis E. Fragkos, Ph.D

Phone: (+1) 484 - 758 - 7074 · Email: i.e.fragkos@gmail.com

EDUCATION

Doctor of Philosophy (Ph.D.) Jan. 2014 - May 2019
in Electrical Engineering *Lehigh University, Bethlehem, PA, USA*

- Ph.D Advisor: Prof. Nelson Tansu
- Thesis: Study of GaN:Eu & delta-InN based active regions for high efficiency long wavelength emitters

Master of Science (M.Sc.) Oct. 2010 - Oct. 2012
in Applied Physics - Micro/Opto Electronics *University of Crete, Heraklion, Greece*

- M.Sc Advisor: Prof. George Kiriakidis (Physics)
- Co-Advisor: Dr. Elias Aperathitis (FORTH-IESL)
- Thesis: Growth and characterization of Al-doped ZnO thin films for transparent electronics

Bachelor of Science (B.S.) Sept. 2005 - Oct. 2010
in Physics *University of Crete, Heraklion, Greece*

- Specialization Area: Applied Physics
- Minor: Social Psychology, Department of Psychology, University of Crete

PROFESSIONAL EXPERIENCE

Center for Photonics and Nanoelectronics Jan. 2014 - May 2019
Research Assistant *Lehigh University, Bethlehem, PA, USA*

- Process development and optimization of MOCVD epitaxy of III-Nitride materials and active regions;
- Characterization of III-Nitride based materials and active regions;
- Novel active region designs and for long wavelength light emitters;
- Model development for the study of the IQE of the GaN:Eu red LED;
- Theoretical and experimental studies on metal-nitride materials for plasmonic applications;
- Computational model development for various semiconductor devices;

Centro de Investigação em Materiais (CENIMAT) Oct. 2012 – Oct. 2013
Research Scientist *Universidade NOVA de Lisboa, Lisbon, Portugal*

- Growth and characterization of transparent and conductive oxides (TCO's) for transparent electronics;

· Physical vapor deposition techniques (RF, DC Magnetron Sputtering, Thermal Evaporation);
· Process development and optimization;
· Methods for structural, optical and electrical characterization;

Institute of Electronic Structure and Laser Oct. 2010 – Oct. 2012
Research Assistant *Foundation for Research & Technology-Hellas, Heraklion, Greece*

· Growth and characterization of Al doped ZnO thin films;
· Physical vapor deposition techniques (RF, DC Magnetron Sputtering, Thermal Evaporation);
· Methods for structural, optical and electrical characterization;

TEACHING EXPERIENCE

Department of Electrical Engineering Jan. 2015 – May 2015
Teaching Assistant *Lehigh University, Bethlehem, PA, USA*

· ECE 121 Electronic Circuits Laboratory;

Department of Physics Oct. 2010 – Oct. 2011
Teaching Assistant *University of Crete, Heraklion, Greece*

· Advanced Physics Lab (Advanced experiments in modern Physics);

RESEARCH INTERESTS & SKILLS

My research interests lie in the areas of photonic / optoelectronic and microelectronic technologies. As part of my PhD research, I focused on the theoretical and experimental studies of high efficiency III-nitride based light emitters in the visible spectral regime.

Technical Skills

· Hands on experience in semiconductor materials & device - fabrication & characterization;
· III-Nitride semiconductor nanostructures for solid state lighting technologies and opto / microelectronics;
· Metalorganic Chemical Vapor Deposition (MOCVD), physical vapor deposition techniques (PVD);
· Process development and optimization;
· Clean room protocols;
· Data analysis & programming languages: Matlab, Mathematica, Fortran, OriginLab, MS Office;
· Experienced with design & simulation tools: Crosslight Software APSYS, Silvaco, Cadence, PVSyst;

Functional Skills

- Strong research intuition;
- Meticulous and detailed oriented and innately driven to understand issues deeply;
- Highly organized and efficient;
- Ability to balance competing priorities and execute accordingly and in timely manner;
- Strong oral and written communication skills;
- Ability to work independently and be self-motivated;
- Ability to work effectively in a team environment;
- Ability to mentor team members and work in a fluid environment;
- Always excited to discover and study new things;

AWARDS & HONORS RECEIVED

- Dean's Doctoral Assistantship 2014, Lehigh University;
- Lehigh University Research Assistantship (Sept. 2015 – May 2019), Lehigh University;
- Gerondelis Foundation Scholarship 2016;

JOURNAL & CONFERENCE PUBLICATIONS

1. I. E. Fragkos, C. K. Tan, V. Dierolf, Y. Fujiwara and N. Tansu. "Pathway Towards High-Efficiency Eu-doped GaN Light-Emitting Diodes". Nature Scientific Reports 7, 16773 (2017).
2. I. E. Fragkos, V. Dierolf, Y. Fujiwara and N. Tansu. "Physics of Efficiency Droop in GaN:Eu Light-Emitting Diodes". Nature Scientific Reports 7, 14648 (2017).
3. I. E. Fragkos and N. Tansu. "Surface Plasmon Coupling in GaN:Eu Light Emitters with Metal-Nitrides". Nature Scientific Reports 8, 13365 (2018).
4. I. E. Fragkos, W. Sun, D. Borovac, R. Song, J.J Wierer, Jr and N. Tansu, "Delta-InN/AlGaN interlayer integrated in InGaN active region for long wavelength emission", Proc. of the SPIE Photonics West 2018, Gallium Nitride Materials and Devices XIV, San Francisco, CA, February 2019.
5. I. E. Fragkos, W. Sun, D. Borovac, R. Song, J.J Wierer, Jr and N. Tansu, "Delta-InN/AlGaN interlayer integrated in InGaN active region for long wavelength emission", Proc. of the IEEE Photonics Conference 2018, Reston VA, October 2018.
6. I. E. Fragkos and N. Tansu, "Titanium Nitride Surface Plasmon Coupling for Enhanced IQE in GaN:Eu Red Light Emitters", Proc. of the IEEE Photonics Conference 2018, Reston VA, October 2018.
7. I. E. Fragkos, D. Borovac, W. Sun, R. Song, J.J Wierer, Jr and N. Tansu, "Experimental Studies of Delta-InN Incorporation in InGaN Quantum Well for Long

Wavelength Emission", Proc. of the IEEE Photonics Conference 2018, Reston VA, October 2018.

8. I. E. Fragkos, W. Sun, R. Song, and N. Tansu, "Pulsed MOVPE Growth Studies of InN and its Integration into InGaN QW for Long Wavelength Emission", Proc. of the ICMOVPE XIX, Growth of InN and InGaN, Nara, Japan, June 2018.

9. N. Tansu, J. J. Wierer, Jr., I. E. Fragkos, D. Borovac, A. M. Slosberg, and C. K. Tan, "Next Generation III-Nitride Materials and Devices – from Photonics to New Applications", Proc. of the International Symposium on Advanced Plasma Science and its Application for Nitrides and Nanomaterials (ISPlasma 2018), Nagoya, Japan, March 2018. (Invited)

10. I. E. Fragkos, W. Sun, R. Song, and N. Tansu, "Pulse-MOCVD Growth of InN / AlGaN Delta-Layer Active Region for Long Wavelength Emitters", Proc. of the SPIE Photonics West 2018, Gallium Nitride Materials and Devices XIII, San Francisco, CA, January 2018.

11. I. E. Fragkos, W. Sun, and N. Tansu, "Analysis of Asymmetric InGaN-Delta-InN/AlGaN Quantum Wells with GaN Barrier for LEDs", Proc. of the SPIE Photonics West 2018, Light-Emitting Diodes: Materials, Devices, and Applications for Solid State Lighting XXII, San Francisco, CA, January 2018.

12. I. E. Fragkos, C. K. Tan, V. Dierolf, Y. Fujiwara, and N. Tansu, "Engineering the Internal Quantum Efficiency of GaN:Eu based Red Light Emitting Diodes", Proc. of the IEEE Photonics Conference 2017, Orlando, FL, October 2017.

13. I. E. Fragkos, W. Sun, D. Borovac, R. Song, J. J. Weirer Jr., and N. Tansu, "Pulsed OMVPE Growth Studies of InN for Integration in InGaN Active Region", Proc. of the ACGGE-21/OMVPE-18 Conference 2107, III/V Nitride and Other WBG Semiconductors, Santa Fe, NM, August 2017.

14. Y. Zhong, I. E. Fragkos, and N. Tansu, "Surface Plasmon Dispersion Engineering by Using TiN / Au Double Metallic Layers for Yellow up to Red Spectral Emitters", Proc. of the SPIE Photonics West 2017, Photonic and Phononic Properties of Engineered Nanostructures VII, San Francisco, CA, February 2017.

15. I. E. Fragkos, Y. Zhong, C. K. Tan, V. Dierolf, Y. Fujiwara, and N. Tansu, "Enhancement of Internal Quantum Efficiency of GaN:Eu based Red Light Emitters through Surface Plasmon Engineering", Proc. of the SPIE Photonics West 2017, Light-Emitting Diodes: Materials, Devices, and Applications for Solid State Lighting XXI, San Francisco, CA, February 2017.

16. I. E. Fragkos, C. K. Tan, Y. Zhong, V. Dierolf, Y. Fujiwara, and N. Tansu, "On the identification and understanding of limiting factors in IQE of GaN:Eu based PIN diodes for red light emission", Proc. of the SPIE Photonics West 2017, Physics and Simulation of Optoelectronic Devices XXV, San Francisco, CA, February 2017.

17. I. E. Fragkos, C. K. Tan, Y. Zhong, V. Dierolf, Y. Fujiwara, and N. Tansu, "The role of Injection Efficiency in Eu-doped GaN LED", Proc. of the MRS Fall Meeting, Rare Earths in Advanced Photonics and Spintronics, Boston, MA, November 2016.

18. I. E. Fragkos, C. K. Tan, Y. Zhong, V. Dierolf, Y. Fujiwara, and N. Tansu, "Understanding the Current Injection Efficiency in Rare-Earth Doped GaN:Eu Red-Emitting Light Emitting Diodes", Proc. of the IEEE Lester Eastman Conference on High Performance Devices 2016, Bethlehem, PA, August 2016.

19. I. E. Fragkos, C. K. Tan, V. Dierolf, Y. Fujiwara, and N. Tansu, "Rare-Earth Doped GaN Based Light Emitting Diode: A Model of Current Injection Efficiency", Proc. of the SPIE Photonics West 2016, Physics and Simulation of Optoelectronic Devices XXIV, San Francisco, CA, February 2016.

20. I. E. Fragkos, V. Kampylafka, M. Gagaoudakis, K. Moschovis, K. Tsagkaraki, E. Aperathitis and G. Kiriakidis, "Effect of different annealing atmospheres on the properties of Al-doped ZnO thin films", 4th International Symposium on Transparent Conductive Materials, TCM 2012, Hersonissos, Crete, Greece, October 2012.

REFERENCES

1. **Prof. Nelson Tansu** [Fellow of National Academy of Inventors]
   Lehigh University
   Department of Electrical and Computer Engineering
   Center for Photonics and Nanoelectronics
   Email: tansu@lehigh.edu
   Phone: +1 610 - 758 - 2678

2. **Prof. Jonathan J. Wierer, Jr.**
   Lehigh University
   Department of Electrical and Computer Engineering
   Center for Photonics and Nanoelectronics
   Email: jwierer@lehigh.edu
   Phone: +1 610 - 758 - 2602

3. **Dr Renbo Song**
   Scientific Manager
   Lehigh University
   Center for Photonics and Nanoelectronics (CPN)
   Email: resd@lehigh.edu
   Phone: +1 484 - 767 - 7299

4. **Dr. Thomas Charisoulis**
   Hardware Engineer, Apple Inc.
   Email: tcharisoulis@apple.com
   Phone: +1 650 - 864 - 2037